Microscopic nuclear mass model for r-process nucleosynthesis

Mikroskopisches Kernmassen-Modell für r-Prozess Nukleosynthese
Zur Erlangung des Grades eines Doktors der Naturwissenschaften (Dr. rer. nat.)
genehmigte Dissertation von M.Sc. Alexander Arzhanov, geb. in Moskau
Tag der Einreichung: 20.7.2017, Tag der Prüfung: 18.10.2017

1. Gutachten: Prof. Dr. Gabriel Martínez-Pinedo
2. Gutachten: Prof. Dr. Robert Roth

TECHNISCHE
UNIVERSITÄT
DARMSTADT

Institut für Kernphysik
Fachbereich Physik
Theoretische Astrophysik

Microscopic nuclear mass model for r-process nucleosynthesis
Mikroskopisches Kernmassen-Modell für r-Prozess Nukleosynthese

Genehmigte Dissertation von M.Sc. Alexander Arzhanov aus Moskau

1. Gutachten: Prof. Dr. Gabriel Martínez-Pinedo
2. Gutachten: Prof. Dr. Robert Roth

Tag der Einreichung: 20.7.2017
Tag der Prüfung: 18.10.2017

Darmstadt 2017 — D 17

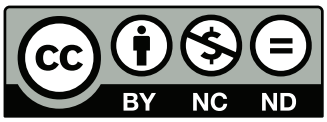

Abstract

Self-consistent mean-field (SCMF) theories based on Hartree-Fock-Bogolyubov (HFB) variational approach with energy density functionals (EDF) were actively developing in the recent decades and have proven successful in systematic studies of low-energy nuclear structure. In particular, current HFB-based mass models are found to be on the similar accuracy level in describing experimental masses as the more phenomenological mass formulas. In order to further increase the descriptive and predictive power of HFB models, we have addressed three particularly important topics that are generally inherent to all EDF approaches with either Skyrme, Gogny, or relativistic mean-field interactions.

Firstly, we analyzed the convergence properties of results obtained with the SCMF calculations based on the Gogny EDF. While in the case of binding energies one generally has to implement prohibitively large harmonic oscillator working bases to ensure convergence, the extracted separation energies are found to be virtually converged even in a relatively modest basis dimension. Nevertheless, by properly controlling the numerical convergence, we have removed the artificial noise that was found in some of the previously published databases for binding and neutron-separation energies. We have also employed and systematically benchmarked one of the recently proposed infrared energy-correction techniques to extrapolate our results to the limit of an infinite model space. We found that this extrapolation scheme can be reliably applied only in the region of well-bound nuclei.

Thereafter, using the same Gogny EDF, we extended the HFB formalism by implementing such beyond-mean-field (BMF) methods as particle-number and angular-momentum symmetry restorations, as well as axial quadrupole shape mixing without assuming the commonly used Gaussian-overlap approximation. We performed global BMF calculations both with D1S and D1M parametrizations of Gogny interaction, and compared binding, separation, and 2^+–excitation energies of the calculated doubly even nuclei to the available experimental data set. We found that the BMF effects amount to $5-6$ MeV of correlation energy, and tend to decrease the shell effects particularly in the region of light nuclei. Moreover, the BMF calculations tend to reduce the shell gaps at $Z = N = 20, 28$, but we could not reproduce the reported quenching for the remaining shell gaps. As for the 2^+–excitation energies, we did not find any significant differences between D1S and D1M parametrizations, while both versions of Gogny interaction tend to overestimate the experimental values.

Finally, we introduced all the necessary tools for performing self-consistent blocking calculations of the odd-A and doubly odd nuclei. We presented results of the global Gogny-HFB survey up to the neutron drip line from $Z = 8$ up to $Z = 134$ with explicit treatment of the time-odd fields. We also compared our results to the experimental data, as well as values obtained with the widely used PQPA method of approximative blocking. The overall pairing strength of the D1S functional is found to be adequate and provide a good qualitative level of description for the main features of pairing gaps. The calculations with explicit T-odd fields were generally found to capture more subtle traits of the observed odd-even staggering effects. Analysis of the global systematics showed, however, a noticeable deviation of the calculations from the reported mass-dependence of experimental pairing gaps.

Zusammenfassung

Selbstkonsistente mittlere Feldtheorien (SCMF), basierend auf dem Hartree-Fock-Bogolyubov (HFB) Variations-Ansatz mit Energie-Dichte-Funktionalen (EDF), wurden in den letzten Jahrzehnten vermehrt entwickelt und haben sich bei systematischen Studien niederenergetischer Kernstruktur bewährt. Insbesondere zeigen aktuelle Kernmassen-Modelle basierend auf HFB eine vergleichbare Genauigkeit bei der Beschreibung experimentell bestimmter Kernmassen wie die phänomenlogischeren Massenformeln. Um die Aussage- und Vorhersagekraft von HFB-Modellen weiter zu verbessern haben wir uns mit drei wesentlichen Aspekten beschäftigt die inherent sind zu allen EDF-Ansätzen mit Skyrme-, Gogny-, oder relativistischen mittleren Feld-Wechselwirkungen.

Zunächst haben wir die Konvergenz der Ergebnisse von SCMF-Berechnungen basierend auf dem Gogny-EDF analysiert. Während Konvergenz bei den Bindungsenergien im Allgemeinen die Implementierung von unrealisierbar großen harmonische Oszillator-Basen benötigt, zeigen sich die extrahierbaren Abspaltungsenergien schon bei relativ überschaubaren Basis-Dimensionen als quasi konvergent. Durch sorgfälltige Kontrolle der numerischen Konvergenz ist es uns darüber hinaus gelungen das künstliche Rauschen zu beseitigen welches sich in einigen publizierten Datensätzen für Bindungs- und Neutronen-Abspaltungs-Energien gefunden hat. Weiter haben wir eine kürzlich vorgeschlagene Technik für Infrarot-Energie-Korrekturen angewandt und systematisch getestet um unsere Ergebnisse hin zum Grenzfall unendlicher Modellräume zu extrapolieren. Es hat sich herausgestellt, dass dieser Extrapolationsansatz nur im Bereich stark gebundener Kerne verlässlich angewandt werden kann.

Im Anschluss daran haben wir, unter Verwendung der gleichen Gogny EDF, den HFB Formalismus insofern erweitert, als das wir Methoden jenseits der mittleren-Feld-Theorie (s.g. *beyond-mean-field*, auch BMF) implementiert haben. Im Detail handelt es sich um Wiederherstellung der Teilchenzahl- und Drehimpuls-Symmetrie, sowie Mischung der axialen Quadrupol-Verformung ohne Annahme der häufig genutzten Näherung der Gausschen Überlagerung. Wir haben globale BMF-Berechnungen für die beiden Parametrisierungen D1S und D1M der Gogny-Wechselwirkung durchgeführt. Für die so bestimmten doppelt-geraden Kerne haben wir die Bindungs- und die Abspaltungs-Energie sowie die 2^+-Anregungsenergien mit den verfügbaren experimentellen Daten verglichen. Dabei führen die BMF-Effekte zu $5-6\,\mathrm{MeV}$ Korrelationsenergie und neigen gleichzeitig dazu die Schaleneffekte insbesonder für leichte Kerne abzuschwächen. Darüber hinaus führen die BMF-Berechnungen zu reduzierten Schalenabständen für $Z = N = 20, 28$. Die beobachtete Schmälerung der übrigen Schalenabstände konnten wir allerdings nicht reproduzieren. Für die 2^+-Anregungsenergie haben wir keine nennenswerten Unterschiede zwischen den beiden Parametrisierungen D1S und D1M festgestellt, jedoch zeigen beide Gogny-Wechselwirkungen eine Überschätzungen des experimentellen Messwerts.

Schließlich haben wir alle notwendigen Werkzeuge für die selbstkonsistene Berechnung des Quantenauschluss (s.g. *blocking*) in einfach und doppelt ungeraden Kernen eingeführt. Wir präsentieren die Ergebnisse eine globalen Gogny-HFB Betrachtung bis zur Neutronen-Abbruchkante und einer Protonenzahl zwischen $Z = 8$ und $Z = 134$, bei expliziter Berücksichtigung der Zeit-ungeraden Felder. Zudem vergleichen wir unsere Ergebnisse sowohl mit experimentellen Daten als auch mit Werten die aus der weit verbreiteten PQPA-Methode für genähertes Blocking gewonnen werden. Die allgemeine Paarbildungs-Stärke des D1S Funktionals erweist sich als angemessen und liefert eine qualitativ gute Beschreibung der Haupteigenschaften der Paarungs-Abstände (s.g. *pairing gaps*). Die Berechnungen mit den expliziten Zeit-ungeraden Feldern sind in der Lage feineren Eigenheiten der beobachteten gerade-ungerade Staffelung einzufangen. Die Analyse der globalen Systematik zeigt jedoch eine merkliche Abweichung der Berechnungen von der beobachteten Masse-Abhängigkeit der experimentellen Paarungs-Abstände.

Contents

1 Introduction and motivation

In 1957 Burbidge *et al.* [1] and Cameron [2] laid down the foundation for the concepts that describe how chemical elements heavier than helium are produced in the Universe. The primary observational basis in the subsequently developed theories of nucleosynthesis was the noticed systematics in the elemental abundance distribution of the solar system matter. Sixty years later, the emerging field of nuclear astrophysics is now able to provide a solid explanation of synthesis of the heavy elements in astrophysical environments.

The *slow* neutron-capture process, or the *s*-process, is responsible for the origin of approximately half of the chemical elements heavier than iron. The synthesis of these elements occurs in a stellar environment where the density of free neutrons is sufficiently low to ensure that the radioactive isotope formed after a neutron capture have time to β-decay back to a stable nucleus before capturing another neutron. The *s*-process therefore operates along the valley of stability, crossing along its path the $N = 82$ and $N = 126$ neutron shell-closures in the region of stable nuclei. This fact mirrors itself in the observed *s*-process peaks of the solar abundances at $A \sim 138$ and $A \sim 208$ (Fig. 1.1). Spectroscopic observations of the so-called asymptotic giant branch (AGB) stars have supplied us with firm evidence of the ongoing *s*-process operation, thereby also unambiguously identifying its astrophysical site [3]. Because the nuclear properties of the isotopes along the *s*-process path are rather well established, reliable calculations of the *s*-process abundances are possible. However, the *s*-process terminates by α-decays around the heaviest stable isotope ^{209}Bi, and cannot account for the production of, for example, such long-lived radioactive actinides as thorium and uranium.

The *rapid* neutron-capture process, or the *r*-process, is second principal mechanism of nucleosynthesis that accounts for the production of roughly another half of all trans-iron elements in the Universe. The *r*-process takes place in such exotic astrophysical environments, where, due the extremely high neutron density conditions, the neutron captures occur on the timescales that are generally much shorter than the typical β-decay lifetimes. In this way, sequential neutron captures become possible, which drives the path of the *r*-process nucleosynthesis further away from the valley of β-stability to the region of very neutron-rich nuclei (Fig. 1.1). Once the neutron flux drops, the radioactive material accumulated at the so-called *waiting points*, predominantly around $N = 82$ and $N = 126$ neutron shell-closures, eventually falls onto the valley of stability mostly through a long chain of β-decays. This scenario naturally explains the observed *r*-process peaks in the solar abundances around the $A \sim 130$ and $A \sim 195$ mass numbers (Fig. 1.1), and, in particular, resolves the question about the production of all actinides [4]. However, the quest of determining the actual astrophysical site(s) for the *r*-process is still underway [5–7], and it has been identified as one of the most challenging open questions in physics of the XXI century [8, 9].

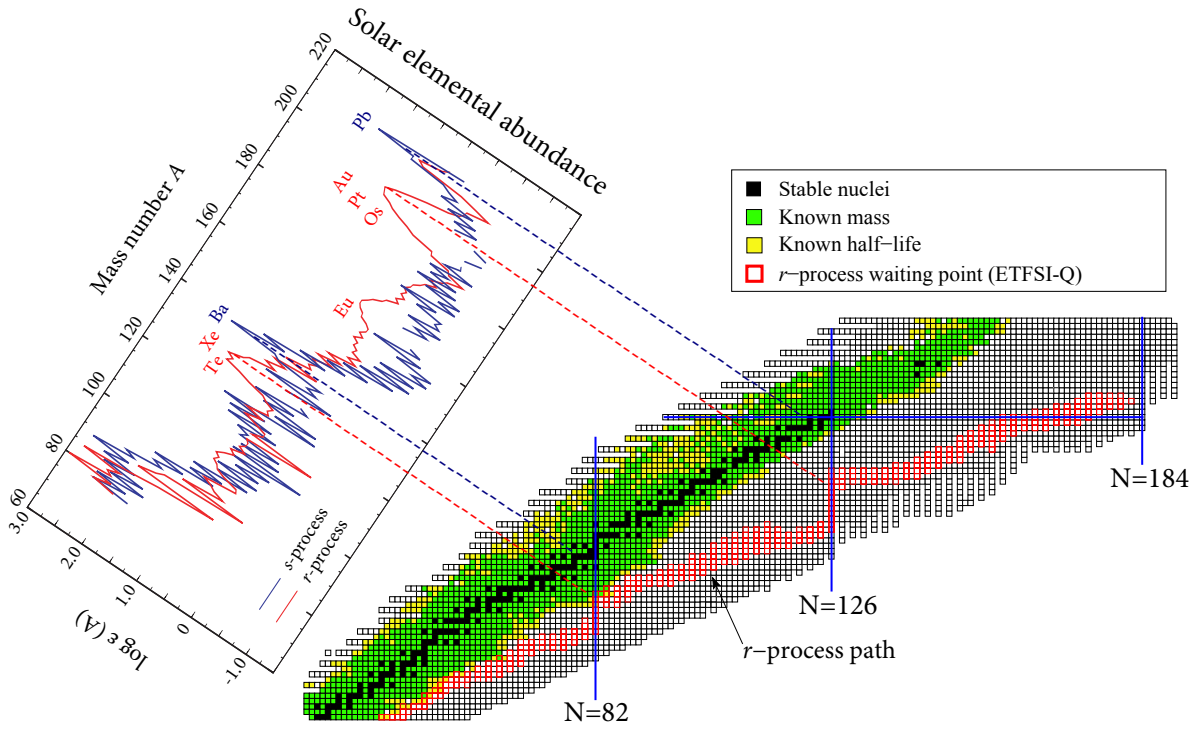

Fig. 1.1: The nuclear chart with indicated stable and experimentally known nuclei together with a calculated potential r-process path. The inset shows the logarithmic s- and r-process solar abundances normalized to hydrogen. Corresponding s- and r-peaks are also indicated. Adapted from Ref. [10] and Ref. [11].

Any attempt to construct a theoretical r-process model is met with significant uncertainties in calculations of elemental abundances. The uncertainties arise not only from the difficulties in modeling the astrophysical environments, but also from the overwhelming set of experimentally unknown nuclear properties that enters the calculations. The relevant range of nuclei for the model input spans all across the nuclear chart, including the domain of superheavy nuclei and potentially reaching up to the neutron-drip line. The fundamental nuclear physics input for any r-process calculation consists of such quantities as neutron capture, photo-dissociation, beta-decay, and fission rates. The nuclear masses are particularly important, as they enter into calculations of these reaction rates, and, through the extracted neutron-separation energies, largely determine the position of the r-process path on the nuclear chart, leaving thereby a direct imprint on the pattern of calculated final elemental abundances.

A great effort has been devoted in the past decades to accurately measure masses of the neutron-rich unstable nuclei [12]. The most recent global compilation of the experimental results contained in the 2012 Atomic Mass Evaluation (AME2012) [13, 14] count a total of 2368 nuclear masses larger than ^{16}O, almost 600 isotopes more than in AME1995 database [15]. Despite of the substantial progress of experimental nuclear physics in the recent years, out of thousands of neutron-rich nuclear species that enter the r-process calculation only about a hundred along the main r-process path are nowadays experimentally accessible. While the new radioactive beam facilities are expected to significantly enrich the experimental database of exotic isotopes, the major part of the nuclei involved in the r-process is still going to remain out of reach in any foreseeable future.

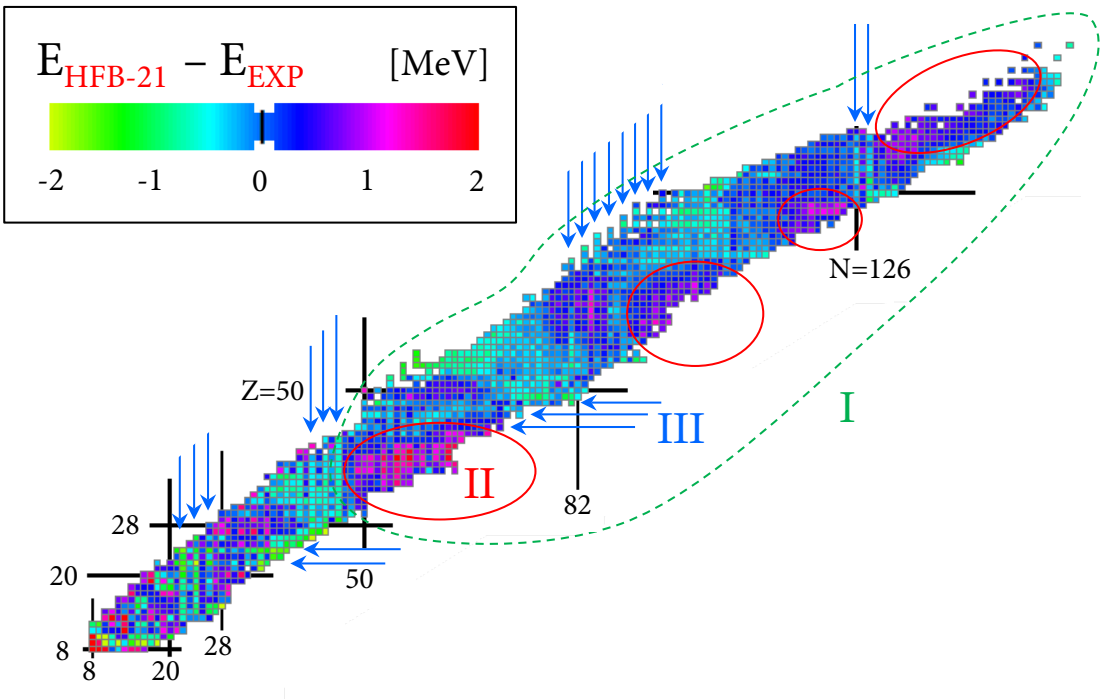

Fig. 1.2: Comparison of the experimentally established nuclear binding energies [22] and the results obtained with HFB-21 [23] mass model. The marked regions on the nuclear chart correspond to the three mentioned problematic issues of HFB models (see text).

This fact compels us to almost entire rely on theoretical predictions of the nuclear properties in r-process nucleosynthsis calculations. Despite the fact that most of the global mass models used in astrophysics have recently achieved a very good descriptive level of the known nuclei, with root-mean-square (rms) deviations from the experimental values of less than 0.8 MeV [16], the local discrepancies and significant difference in the predictions of unknown nuclei have a very noticeable impact on calculations of r-process elemental abundances [17–19].

Self-consistent mean-field (SCMF) theories based on the Hartree-Fock-Bogolyubov (HFB) variational approach with energy density functionals (EDF) were actively developing in the recent decades, and they are now based not only on the global fits to all known masses, but also include various constraints from the *ab initio* calculations of infinite nuclear matter [20, 21]. In particular, the SCMF approach has proven successful in the systematic study of low-energy nuclear structure, which brought the latest global HFB-based mass models (Chap. 2.4) to a similar high-precision level in describing the experimental masses as the more phenomenological mic-mac approaches (Chap. 2.3). However, due to the microscopic nature of the SCMF theories, they are generally expected to provide greater confidence in extrapolating into the neutron-rich extremes of the nuclear chart.

In order to further improve both descriptive and predictive performance of the HFB-based models, we have identified three particularly important topics that are relevant to all currently used HFB models with either Skyrme, Gogny, or relativistic EDFs:

I. Most of the current EDF calculations expand the many-body wave function either on a mesh of finite size and point spacing, or a finite number of harmonic oscillator single-particle states. The calculated observables should, in principle, be independent of a particular choice for the working basis. Nonetheless, this is rarely the case in practical applications due to limited computational resources. In the context of the nuclear masses, the model space truncations result in an incomplete convergence of the binding energies with respect to the exact HFB calculations on the level that can easily greatly exceed the estimated global rms deviation of the model. This is especially the case in calculations of the heavier neutron-rich isotopes, as is indicated on Fig. 1.2 (region I).

II. Furthermore, any HFB mass model typically exhibits particularly pronounced deviations from the experimental values in the nuclear chart regions between the magic numbers, which is, for example, clearly visible on Fig. 1.2 (regions II). This tendency is largely attributed to some of the important correlations that are missing on the purely mean-field level of HFB description. Extending the HFB formalism beyond the static mean-field by employing such symmetry-restoration techniques as particle-number and angular-momentum projections, as well as mixing multiple nuclear deformations is generally expected to significantly reduce the aforementioned discrepancies.

III. Finally, the nuclei with the odd number of neutrons and/or protons are usually not treated in the global HFB calculations on the same footing as their even-even neighbors. A proper self-consistent calculation of such odd-mass nuclei requires to break the time-reversal symmetry, which makes their treatment much more sophisticated and time-consuming in comparison to the doubly even nuclei. The adopted approximations that keep the benefits of time-reversal symmetry often result in the elevated local uncertainties in describing the odd-mass nuclei, as is evident, for example, by the observed ribbed structure of Fig. 1.2 (regions III).

We have addressed all of these three topics in this work, taking thereby another three steps along the path towards a better microscopic mass model for r-process nucleosynthesis.

This doctoral thesis is organized as follows:

Chapter 2 outlines the current status of the most successful modern nuclear structure models. Starting with a brief reference to the modern high-precision and chiral nuclear interactions, we outline the main ideas and the latest developments of the most successful *ab initio* nuclear structure methods to provide a broader perspective for the later discussion of the more phenomenological microscopic self-consistent mean-field models. Completing our overview, we also mention the present status of the so-called mic-mac mass formulas, as they have lately been tuned to a very impressive descriptive power.

Chapter 3 provides a short review of the historical development and the current state of affairs for the three major types of density-dependent effective interactions used in the SCMF models: the zero-range Skyrme and the finite-range Gogny non-relativistic interactions, as well as the family of relativistic mean-field interactions.

Chapter 4 presents the theoretical framework of the Hartree-Fock-Bogolyubov (HFB) formalism to solve the nuclear many-body problem. Starting from the Bogolyubov transformation for quasi-particles, we introduce the main concepts of the SCMF theory, derive the relevant HFB equations, and present the gradient method for their iterative solution. Thereupon, built on the established HFB formalism, we introduce the techniques for such beyond-mean-field (BMF) extensions, as particle-number and angular-momentum projections, as well as the symmetry-conserving configuration-mixing (SCCM) within the formalism of generator coordinate method (GCM).

Chapter 5 addresses the convergence properties of the nuclear binding energies and the extracted two-neutron separation energies obtained from Gogny-HFB calculations. We employ and benchmark one of the recently proposed infrared energy-correction techniques to extrapolate our results to the limit of an infinite model space. We also discuss its applicability to the global calculations of the nuclear masses.

Chapter 6 studies the BMF corrections and their impact on the HFB calculations. In particular, we perform particle-number restoration, angular-momentum projection, and configuration mixing using D1S and D1M parametrizations of the Gogny interaction. We systematically analyze the correlation energies from each of the BMF methods and compare our calculations to the experimentally known nuclear masses, two-particle separation energies, and 2^+ first-excited states.

Chapter 7 introduces all the necessary tools for performing self-consistent blocking calculations of the odd-A and doubly odd nuclei. We presented results of the global Gogny-HFB survey up to the neutron drip line from $Z = 8$ up to $Z = 134$ with explicit treatment of the time-odd fields. We also compared our results to the experimental data, as well as values obtained with the widely used PQPA method of approximative blocking. We also discuss the global systematics of the neutron pairing gaps extracted from both self-consistent blocking and PQPA calculations.

Chapter 8 concludes this doctoral thesis with a general discussion of the results and outlines the ramaining major challenges in the nuclear EDF theory.

2 Modern nuclear structure methods and their current status

Several dozens of nuclear structure models have been developed in the last 70 years, but only a handful can be used nowadays to satisfy the demanding requirements of an r-process nucleosynthesis calculation. A more fundamental model that relies on a microscopic description as much as possible is generally expected to provide a greater confidence in extrapolations to the unknown territory of the nuclear landscape, and will provide *not only* masses and basic ground-state properties, but a *complete* and *unified* model to describe the details of nuclear structure. Pursuing this ideal, in the most fundamental approaches one tries to derive masses and all other nuclear properties directly from the basic nucleonic interactions. Although that such *ab initio* models are still not quite capable of producing a complete mass table required for a r-process nucleosynthesis calculation, many novel developments within these fundamental approaches have recently vastly extended their accessible domain well into the regions of heavier nuclei on the nuclear chart. In an attempt to provide a broader perspective in discussing current trends and future development of the more phenomenological nuclear structure models, we briefly recap the status of the modern realistic nuclear interactions in Sec. 2.1, and concisely outline the main concepts and the current status of the most successful modern *ab initio* approaches in Sec. 2.2. Thereafter, in Sec. 2.3 we follow a diametrically opposite path compared to *ab initio* approach and review the main ideas of a purely macroscopic liquid-drop origin, which lie in the foundation of the so-called microscopic-macroscopic (mic-mac) methods. The mass models of this family deserve a closer attention, as they have lately been tuned to a very impressive descriptive power and are now extensively used in various r-process calculations [17]. Ultimately, in Sec. 2.4 we introduce a group of nuclear structure methods, which can be considered to lie somewhere in between the fundamental *ab initio* approach and the phenomenological mic-mac models. These are the microscopic approaches of the interacting Shell Model (ISM) and the self-consistent mean-field (SCMF) methods. Particular attention in the following chapters will be drawn to the SCMF approach based Hartree-Fock-Bogolyubov formalism, which underlies the rest of this doctoral thesis.

2.1 Nuclear interactions from the first principles

One of the primary quests of nuclear physics is to explain the structure and dynamics of the nuclei staring from the free-space interaction between individual nucleons. Pursuing this goal, the first part of the puzzle is to establish an appropriate interparticle Hamiltonian based on the underlying first principles of Quantum Chromodynamics (QCD) theory, which in itself is an ongoing and challenging task for low-energy nuclear physics.

The difficulties stem from the very nature of the nuclear force. The development of QCD has shown that neutrons and protons are not elementary particles. Nucleons consist of quarks and gluons that interact among each other predominantly through the strong interaction, and it is the residual of this interaction that manifests itself in the internucleonic force. Due to a distinctive feature of QCD termed as *asymptotic freedom* [24, 25] – weakening of the strong coupling constant as the energy approches high values – the strong interaction can be treated perturbatively only in a high-energy regime. As for the low-energy domain of QCD, which is relevant for derivation of the residual nucleon-nucleon (NN) interaction, the value of the strong coupling parameter renders any perturbative approach as impossible. There are, however, undergoing work to extract the nuclear potential in a non-perturbative manner directly from the low-energy QCD by means of the lattice calculations [26, 27], but these early attempts are still facing numerous computational challenges [28] and do not yet employ physical quark masses [29, 30]. As for another low-energy feature of QCD, the *color confinement* [31] principle emphasizes the fact that the color-charged quarks and gluons have never been observed isolated, but they always form color-neutral hadrons. The phenomenon of confinement thus warrants the idea to effectively eliminate quarks and gluons from the problem of NN-interaction, and reformulate it in terms of baryons and mesons – the observed degrees of freedom in low-energy domain of QCD.

2.1.1 High-precision NN–potentials

Even before the discovery of QCD in 1980s, the conventional way to tackle the problem of nuclear interaction was to adopt the meson-exchange picture in an attempt to parametrize the nuclear force. Only in retrospect can the confinenment principle of QCD provide a rigorous justification for the absence of free quarks in such models. Nevertheless, the original idea dates back to the seminal work of Yukawa, who in 1935 [32] performed the first attempt to describe the NN-interaction by means of the pion-exchange mechanism. Following the experimental discovery of pion and other heavier mesons shortly after, the outcome was an emergence of various phenomenological boson-exchange models, which still provide the foundation for many sophisticated modern NN-potentials. Such realistic potentials consist of several terms with varying meson-exchange and/or other operator structures that are motivated by various symmetry considerations, but their corresponding radial functions are fitted to an extensive set of experimental characteristics of the few-body systems, such as nucleon-nucleon scattering data and properties of deuteron [33]. Examples of bare nuclear potentials actively used in modern nuclear computations include Nijmegen [34], CD-Bonn [35], and Argonne V18 [36] high-precision potentials. Despite that many of such state-of-the-art phenomenological potentials provide an excellent description of elastic scattering phase shifts and other experimental data, when plugged into a many-body calculation they often show various unaccountable discrepancies with experimental data even in the region of the light nuclei [37]. Most of these problems can be related to the absence of naturally emerging three-body (or even higher-order) interactions in the resulting Hamiltonian [38]. Thus in order to provide accurate results, the high-precision NN-potentials have to be augmented separately with three-nucleon (3N) forces, like the ones from Urbana IX [39] or Tucson Melbourne models [40]. Moreover, such phenomenological constructions of the NN-potential do not allow for their systematic improvements in terms of the dominant dynamical contributions.

2.1.2 Nuclear forces from chiral Effective Field Theory

An alternative and a rather new approach became available with a concept of an effective field theory (EFT), the construction of which was outlined by Weinberg [41] in 1979. The idea was to set up the most general Lagrangian that includes higher-derivative terms and respects a certain number of QCD symmetries, including the assumption of the chiral symmetry. Then, instead of the quarks and gluons, the only relevant low-energy degrees of freedom are the nucleons and the pions – the Goldstone bosons corresponding to the chiral symmetry [42]. Furthermore, since such Lagrangian generally consists of an infinite number of terms, he suggested a kind of perturbative expansion such that only a finite number of terms, ordered by their decreasing importance, could contribute to the interaction. For this purpose Weinberg introduced the so-called *power-counting* scheme – a low-momentum expansion in terms of powers $(Q/\Lambda_\chi)^\nu$, where Q is a soft scale momentum typical for the interaction ($Q \sim m_\pi$), the Λ_χ is the hard scale, often called chiral symmetry breaking scale, that limits the validity of the effective theory ($\Lambda_\chi \sim m_\rho$), and $\nu \geq 0$ is the order of expansion [43]. Although that the basic idea of pion-exchange interaction was akin to the one already suggested by Yukawa, the insight that ensured success of the new EFT scheme was the aknowledgement of the chiral symmetry as an important contraint for the theory [42]. The resulting chiral effective field theory (χEFT) provides both a firmer link with the underlying QCD, as well as enables to systematically improve the theory by calculating additional Feynman diagrams of increasing importance according to the power-counting scheme. Finally, the two-body and higher multi-nucleon forces arise on an equal footing by including Feynman diagrams of higher order. For example, first contributions to 3N-forces appear naturally starting from $\nu = 2$ term of expansion, usually denoted as the next-to-next-to-leading order ($\mathrm{N^2LO}$) [43]. The diagrams that involve contact interactions are characterized by the so-called low-energy constants (LECs), which effectively absorb all the unresolved short-distance dynamics due to the missing heavier mesons in the χEFT theory. For example, at the well-established $\mathrm{N^3LO}$ level, there is a total of 24 LECs that have to be fixed by the experimental data [44], or eventually better constrained from the upcoming lattice QCD calculations.

However, because the free parameters of χEFT or any other traditional free space NN-potential are established directly from NN scattering data and some properties of few-nucleon systems, such interactions are in line with *ab initio* philosophy when employed in the nuclear structure methods.

2.2 The *ab initio* approach to nuclear many-body problem

Having established the most fundamental internucleonic potential, the *ab initio* nuclear structure approaches are met with the second part of the problem, namely to solve the non-relativistic many-body Schrödinger equation in a most exact manner that is possible.

2.2.1 Exact solution with Faddeev-Yakubovsky formulation

Essentially exact solutions with realistic vacuum forces are available only for $A \leq 4$ systems based on Faddeev [45, 46] approach and its Faddeev-Yakubovsky [47, 48] generalization, as well as their extensions introduced by Alt, Grassberger, and Sandhas (AGS) [49, 50]. All of them are based on Lipmann-Schwinger reformulation of the Schrödinger equation to derive a set of coupled integral equations that describe the many-body quantum mechanical system. For more than four nucleons, however, the number of equations becomes prohibitive for an exact solution [51].

2.2.2 Quantum Monte Carlo methods

Another path to *ab initio* nuclear structure calculations is taken by the class of quantum Monte Carlo (QMC) methods [52], which all involve a stochastic approach to solve the many-body problem. In the context of QMC methods, that are well-suited for local phenomenological and chiral NN+3N interactions [53], the greatest success can be attributed to the Green's Function Monte Carlo (GFMC) method [39, 54]. The GFMC approach is built upon the basic idea of Diffusion Monte Carlo (DMC) algorithm – to propagate the initial trial wavefunction $|\Psi_T\rangle$ in imaginary time τ until the ground-state wavefunction $|\Psi_0\rangle$ can be projected out with a required degree of numerical precision. Thus instead of solving the Schrödinger equation directly, the ground-state energy can be obtained as

$$E_0 = \lim_{\tau\to\infty} \frac{\langle\Psi_T|He^{-(H-E_0)\tau}|\Psi_T\rangle}{\langle\Psi_T|e^{-(H-E_0)\tau}|\Psi_T\rangle}. \tag{2.1}$$

The evolution of $|\Psi_T\rangle$ is carried out by discrete stochastic sampling in a number of n small $\Delta\tau$-steps, such that

$$e^{-(H-E_0)\tau} = \left[e^{-(H-E_0)\Delta\tau}\right]^n. \tag{2.2}$$

An introduction of the guiding Green's function in the GFMC approach optimizes the DMC algorithm to reduce the accumulated errors with each time step, which is also no longer kept constant. Although that GFMC can provide formally exact numerical solutions, the required computational cost scales exponentially with the size of the nuclear system under consideration. This fact currently restricts the nuclear domain of GFMC method to $A \leq 12$ systems and causes substantial computational difficulties in the limiting case of ^{12}C [52]. While the Auxiliary-Field Diffusion Monte Carlo (AFDMC) [55] extension of GFMC is capable of handling heavier nucleon systems due to separate sampling of spin-isospin component of the wavefunction, up to now it has only been applied to pure neutron systems [56]. It is also worth mentioning another relatively recent and perspective addition to the QMC family of *ab initio* methods, namely the Nuclear Lattice Effective Field Theory (NLEFT) that combines the χEFT theory with AFDMC algorithm. The pricipal idea of NLEFT is similar to the one of GFMC approach,

except that the dynamical degrees of freedom are the point-like nucleons and pions rather than "walker"-particles. As of now, the NLEFT calculations have been successful up to $A \sim 12$ nuclei [57], but the method have recently also been used to compute the ground-state energies for heavier α-particle multiplets up to ^{28}Si [58].

2.2.3 Formulation of variational principle

Many approaches in quantum mechanics, including some of the *ab initio* nuclear structure methods, rely on variational formulation of the exact Schrödinger equation [59], which can be stated in form of the stationary condition

$$\delta E\left[\Psi\right] = 0, \tag{2.3}$$

where the energy functional can be defined as

$$E\left[\Psi\right] = \frac{\langle\Psi|H|\Psi\rangle}{\langle\Psi|\Psi\rangle}. \tag{2.4}$$

The variational equation is particularly well-suited for ground-state energy calculations, since the variational principle ensures that the energy functional of any trial wavefunction $|\Psi_T\rangle$ is always greater or equal to the true ground-state energy of the many-body system E_0, that is

$$E\left[\Psi_T\right] \geq E_0. \tag{2.5}$$

By minimizing the energy functional for a set of trial wavefunctions, the one that yields lower energy value will provide a better approximation to the exact solution of the Schrödinger equation. In particular, if the trial wavefunction is expanded on a finite set of basis functions, a convergence to the exact solution of the Schrödinger equation is guaranteed in the limiting case of an infinite working basis. While there are numerous *ab initio* variational methods that primarily differ in the adopted form of the trial wavefunction, the Hyperspherical Harmonics and the no-core Shell Model methods that we mention below, are arguably among the most successful.

2.2.4 The Hyperspherical Harmonics method

The Hyperspherical Harmonics (HH) method can directly employ such modern realistic NN-potentials as Argonne V18 to variationally establish the many-body wavefunction that is decomposed in terms of hyperspherical harmonic functions, which are the A-body generalization of the usual spherical harmonics Y_{lm} [60]. Even though that HH method and its Correlated Hyperspherical Harmonics (CHH) [61] extention can be formulated for an arbitrary finite number of particles, they are met with substantial convergence and other symmetry-related difficulties that currently limit their application to $A \lesssim 6$ systems [62, 63].

2.2.5 No-core Shell Model and its extensions

The no-core Shell Model (NCSM) [64, 65] presents another successful *ab initio* approach based on direct matrix diagonalizations. In comparison to the standard interacting Shell Model (ISM), there is no inert core and all A nucleons of the nuclear system are considered to be active explicitly and interact by suitable NN- and 3N-forces. The NCSM many-body trial wavefunction $|\Psi_{\mathrm{NCSM}}\rangle$ may be built as a linear superposition of A-particle Slater determinants

$$|\Psi_{\mathrm{NCSM}}\rangle = \left(1 + \sum_{n=1}^{A} C_n\right) |\Psi\rangle, \tag{2.6}$$

where, given an appropriate reference state $|\Psi\rangle$, the C_n operator generates all possible n-particle-n-hole (np-nh) excitations. For any practical application, the model space has to be restricted to excitations up to a certain energy value that defines the model space dimension N_{max}. The calculations are usually performed in a harmonic oscillator (HO) basis due to computational convenience. Despite all the benefits from using the HO basis, the straightforward NCSM calculations with most standard high-precision and chiral potentials are met with difficulties related to the incorrect asymptotic behavior of the truncated HO basis, a topic which we discussed thoroughly later in Chap. 5. The problem is due to the strong short-range nature of the bare interactions, which cannot be correctly resolved in any finite HO basis. Even if one starts with a relatively soft realistic potential, like JISP [66] that is based on inverse scattering, or a variant of chiral N^{3}LO NN-potential [67], the convergence of the calculation from enlarging the basis is relatively slow. In order to capture the relevant short-range part of interaction and improve convergence, one usually proceeds by constructing an effective Hamiltonian where the realistic interactions are modified with unitary transformation schemes, like the ones of Okubo [68] or Lee-Suzuki [69]. The resulting softer effective interactions render the NCSM calculation feasible, but are tailored for that particular A-body system and model space at hand, meaning that the NCSM diagonalizations are no longer variational with respect to basis parameters [64]. Alternatively, with a recent rapid development of the Renormalization Group (RG) techniques that we discuss in the next section, one can directly start with a realistic NN-potential that has been softened by a similarity transformation *prior* to NCSM calculations. Thus the need to modify the initial Hamiltonian may be avoided, while ensuring variational and rapidly convergent NCSM calculations. Nevertheless, the dimensions of matrix eigenvalue problem in the NCSM approach grow exponentially with the considered number of nucleons and HO basis dimension, which defines the current limit of NCSM for precise convergent calculation of bulk nuclear properties to $A \leq 16$ nuclei. Only with the recent introduction of an extension to NCSM, namely the importance-truncated NCSM (IT-NCSM) [70, 71] that substantially reduces the required model space dimension by truncating unimportant basis states for ground-state calculations, the NCSM-based methods, aided by similarity-transformed chiral interactions, have systematically extended their domain to the lower *sd*-shell nuclei [72], reaching in some cases even to ^{40}Ca [73]. Other extentions that are currently under active development include symmetry-adapted NCSM (SA-NCSM) [74], and no-core Monte-Carlo Shell Model (MCSM) [75].

2.2.6 Similarity transformation techniques

As was already mentioned in the discussion of the NCSM above, the hard repulsive core of a bare NN-interaction poses serious complications for any practical many-body calculations in a truncated model space. In the past century this issue was significantly hindering the progress of *ab initio* nuclear structure methods, and one had to introduce sophisticated many-body techniques, like relativistic Brueckner-Hartree-Fock [76, 77], or correlated basis functions [78, 79], to deal with singular behavior of the vacuum NN-forces. Only with the recent vast leap forward in accessible computational power such virtually exact methods as GFMC and NCSM became capable of reaching out to the p-shell nuclei [60]. Despite that the rapidly developing chiral effective field theory have produced much softer potentials than the traditional meson-exchange interactions, their direct implementation is not truly optimal to ensure sufficient convergence when dealing with heavier nuclear systems and large model spaces. The strong short-range NN-correlations are still present at the chiral separation scale Λ_χ and are responsible for significant coupling of low- to high-momenta states, which, in turn, manifests itself in large off-diagonal matrix elements of interaction [80]. This issue has stipulated ideas to further exploit the concept of EFT and eventually resulted in a relatively new way to approach the realistic nuclear forces through the framework of Renormalization Group (RG) apparatus. The RG methods provide tools to evolve the nuclear interaction by means of similarity transformations, and thereby change its energy and momentum resolution to the scales relevant for the low-energy nuclear structure calculations at hand. The phase-shift equivalent RG techniques allow to integrate out the troublesome high-momentum modes in a manner that leaves the low-energy observables invariant [81].

The model-independent RG methods can be classified by two slightly different prescriptions to renormalize the high-momentum modes. The $V_{\mathrm{low}k}$ scheme [82] introduces a momentum cutoff parameter Λ, that smoothly drives the matrix elements above the cutoff boundary momentum to zero. Essentially it removes the high-momentum modes of the interaction, while leaving the phase shifts of the initial interaction up to the cutoff unchanged. The Similarity Renormalization Group (SRG) [83], arguably the most popular unitary transformation technique by now, utilizes the flow equation to continuously evolve the interaction to a band-diagonal form, thereby effectively decoupling the high- and low-momentum modes. The transformation is driven by the momentum regulator λ, which defines the degree of such decoupling, while unitarity ensures the phase-shift equivalence throughout whole momentum space. We can also mention the Unitary Correlation Operator Method (UCOM) [84] to soften the realistic NN-interaction, whose correlated operators that pre-diagonalize the initial Hamiltonian can be extracted from the more general SRG approach.

The main idea of the SRG method is to evolve the original Hamiltonian H, or any other observable of interest, by a continuous unitary transformation U_α, as

$$H_\alpha = U_\alpha^\dagger H U_\alpha. \tag{2.7}$$

Differentiating the above equation with respect to the flow parameter α, one recovers the so-called flow equation that governs the evolution of Hamiltonian H_α, namely

$$\frac{dH_\alpha}{d\alpha} = [\eta_\alpha, H_\alpha]\,, \tag{2.8}$$

where the transformation generator η_α has the form

$$\eta_\alpha = \frac{dU_\alpha}{d\alpha} U_\alpha^\dagger. \tag{2.9}$$

By solving the flow equation one can let the α to continuously flow along a particular path, dictated by a suitable choice of η_α generator, to a specific value α_λ. This will drive the Hamiltonian in a suitable representation (*e.g.* HO basis, or momentum space) to its band-diagonal form H_λ, where the width of the band is related to $\lambda \sim \alpha^{-1}$. Starting from a NN- or 3N-Hamiltonian, this generic scheme will result in a transformed Hamiltonian that generally acquire A-body terms during evolution, thus in the practical calculations one usually restricts the evolution to two- or three-body space. While this restriction formally violates the unitarity of transformation, as long as the relevant observables remain independent of the α parameter, one can cautiously disregard this important shortcoming [85].

Apart from utilizing the RG techniques to produce low-momentum NN- and 3N-interactions that are well-suited for the many-body calculation [86], the concept of similarity transformation has been also been successfully implemented in such *ab initio* approaches as Coupled Clusters (CC) method and the newly introduced In-Medium Similarity Renormalization Group (IM-SRG) method.

2.2.7 The Coupled Clusters approach

The Coupled Clusters (CC) method was first introduced to nuclear physics in 1950s [87], but because of the complications with the mentioned strong short-range correlations, there were only a few practical applications [88, 89]. Nonetheless, since then the CC method was successfully implemented in the field of quantum chemistry [90]. Only recently the CC approach was brought back to active development in the nuclear physics community [91].

The correlated CC–state $|\Psi_{\mathrm{CC}}\rangle$ can be formally built from a suitable reference single Slater-determinant state $|\Psi\rangle$ (*e.g.*, a Hartree-Fock ground-state) using a so-called cluster operator T as an exponential cluster expansion [92], namely

$$|\Psi_{\mathrm{CC}}\rangle = e^T |\Psi\rangle, \qquad \text{with} \quad T = \sum_{n=1}^{A} T_n. \tag{2.10}$$

where T_n is the cluster operator of rank n that is used to generate np-nh excitations in the reference state. In practical calculations the maximal rank of the employed cluster operator has to be restricted. Leaving only the first rank operator $T = T_1$ that produces 1p-1h excitations is referred to as CC with Singles (CCS) approximation. By the same token, CC with Singles and Doubles (CCSD) [93] approximation refers to additional inclusion of 2p-2h excitations by means of $T = T_1 + T_2$ operator. By including higher ranks of the cluster operator, one can hierarchically improve the method [91].

The energy expectation value E of a CC-state can formally be written in terms of the initial (normal-ordered) Hamiltonian H as

$$E = \langle \Psi_{\mathrm{CC}} | H | \Psi_{\mathrm{CC}} \rangle = \langle \Psi | e^{-T} H e^T | \Psi \rangle = \langle \Psi | H_{\mathrm{CC}} | \Psi \rangle \tag{2.11}$$

where, if one interprets the exponential form e^T as a transformation, one can define the coupled clusters similarity-transformed effective Hamiltonian as $H_{\mathrm{CC}} \equiv e^{-T} H e^T$ [94].

The coefficients (amplitudes) of all excited Slater-determinants that comprise the CC-state in Eq. (2.10) are then found by solving the set of coupled CC equations [91]. The computational cost of the standard CCSD approach scales with configuration space size M as $(M-A)^4A^2$ [95] and is much more gentle than other *ab initio* methods, like the ones of NCSM or GFMC. While the CCSD with Triples (CCSDT) is still computationally very demanding [94], the triply excited states have been treated perturbatively in CCSD(T) [96] approach. Recently, other more sophisticated techniques to include triples, like ΛCCSD(T) [97, 98] and CR-CC(2,3) [99, 100], were successfully employed to perform calculations of light and medium-mass nuclei. Only recently have the CC calculations been extended also to the domain of heavy nuclei, extending from ^{16}O all the way to ^{132}Sn [101]. Despite the rapid development of the CC techniques, up to now the method was successfully applied mostly in calculations of nuclei with closed sub-shells.

2.2.8 In-Medium Similarity Renormalization Group method

The SRG techniques to soften the nuclear interactions in free space have played a crucial role in the recent significant progress of *ab initio* methods [81]. However, the development of the method initially faced substantial technical difficulties to consistently evolve the 3N-interactions, which manifested itself, for example, in insufficient independence of calculated observables from the continuous flow parameter α [102]. An alternative approach to directly employ the RG flow equations inside the nuclear medium of the particular A-body system has been introduced. The first step in such In-Medium SRG (IM-SRG) approach [103] is the adoption of normal-ordered form for Hamiltonian (and other operators) with respect to an appropriate A-body reference state, like a one from Hartree-Fock calculation. Similar to the free-space SRG, evaluating the Eq. (2.8) with the normal-ordered Hamiltonian using a suitable SRG generator η_α of Eq. (2.9), one arrives to the coupled differential IM-SRG equations [103]. The Hamiltonian is then evolved with flow parameter α in order to decouple the particle-hole excitations from the given reference state. Generally, regardless of the initial Hamiltonian, the evolved Hamiltonian will include up to A-body interactions. However, by adopting the normal-order prescription, some contributions from the 3N-terms of the original Hamiltonian will be redistributed to the 0-, 1-, and 2-body nucleus-dependent terms of the normal-ordered Hamiltonian. Thus despite that the Hamiltonian and the dynamic generator η_α are currently truncated at the 2-body level due to otherwise unbearable computational cost, such approximation denoted as IM-SRG(2) [104] does still include higher-body interactions that are consistently evolved by the in-medium flow equations using the standard two-body techniques. By driving the evolution until the reference state is completely decoupled from its particle-hole excitations, the ground-state energy is obtained from the expectation value of the transformed Hamiltonian with the reference state [105]. The downside is that the IM-SRG evolution has to be performed anew for every particular nucleus or matter density, akin to Lee-Suzuki similarity transformation [69] procedure mentioned previously. However, since the computational cost of IM-SRG(2) scales polynomially with the size of the basis [103], the method is suitable for much heavier nuclear systems than the ones that are currently accessible with standard NCSM and GFMC approaches. Finally, by including higher-body terms in the IM-SRG equations one can systematically improve the method. The swiftly developing IM-SRG method has vastly extended the *ab initio* domain well into the region of medium-mass nuclei around $A \sim 60$ [106–108], and is currently starting to confront the challenging terrain of open-shell and unstable nuclei [109–111].

2.3 Macroscopic mass formulas with microscopic corrections

The paramount theoretical importance of the *ab initio* nuclear theory cannot be underestimated, as it is meant to provide *not* only the basic bulk nuclear observables, but is able to grant a *complete* and *unified* description of nuclear structure that is built upon the first principles of QCD. However, despite the recent remarkable breakthrough of such nuclear models particularly in low-energy segment of nuclear physics, the *ab initio* methods are yet not capable of reaching across the whole nuclear chart, and thus cannot be universally implemented for the subsequent input into r-process nucleosynthesis calculations. Nevertheless, for time being, such fundamental approaches should serve as a viable reference for the more phenomenological approaches to construct a universal mass table that is essential for any astrophysical model.

In this section we follow the development of nuclear models via a diametrically opposite path to what has been outlined previously. Starting with a purely *macroscopic* liquid drop parametrization of a nucleus and augmenting it with phenomenological shell- and pairing-corrections, one has been able to produce global mass formulas with very high descriptive power. To evaluate the precision of the most successful *global* nuclear models, we define the root mean square (rms) deviation between the theoretical ($M_i^{\rm th}$) and the experimental ($M_i^{\rm exp}$) nuclear masses as

$$\sigma(\text{Year}) = \sqrt{\frac{1}{n}\sum_{i=1}^{n}(M_i^{\rm th} - M_i^{\rm exp})^2}, \tag{2.12}$$

where n is the total number of compared nuclei from the atomic mass evaluation (AME) compilation of the specified *Year* with N and $Z \geq 8$. One should, however, remember that the descriptive accuracy of the models are *not* necessarily correlated with the predictive power for the experimentally unknown regions of the nuclear chart. See, for example, Refs. [16, 112] for a comprehensive study of the predictive quality offered by some modern nuclear mass models.

2.3.1 The Liquid Drop Model

One of the first attempts to theoretically establish a global nuclear mass formula was carried out by von Weizsäcker in 1935 [113]. The Weizsäcker's semi-empirical mass formula was inspired by the macroscopic liquid-drop model (LDM) [114] of the nucleus that was built upon ideas of Gamow [115] and subsequently developed by Bohr and Wheeler [116] to innovatively explain nuclear fission. The LDM considers nucleus as a uniformly charged liquid drop of incompressible nuclear fluid of constant density with a sharp fall-off at the surface. Based on these assumptions, a relatively simple formula for the nuclear binding energy could be devised and brought to wider circles by Bethe and Bacher in 1936 [117]. Since then it has become a fairly good intuitive explanation of the observed nuclear structure trends across the whole nuclear landscape. A slightly modified version of the original formula as a function of the mass number A and the number of protons Z, which can be written as

$$E(A,Z) = a_{\rm V}A + a_{\rm S}A^{2/3} + a_{\rm C}Z^2A^{-1/3} + a_{\rm VS}(A-2Z)^2A^{-1} + a_{\rm SS}(A-2Z)^2A^{-4/3} \tag{2.13}$$

parametrizes the binding energy of a nucleus with several empirical constants corresponding to volume ($a_{\rm V}$), surface tension ($a_{\rm S}$), Coulomb energy ($a_{\rm C}$), volume symmetry ($a_{\rm VS}$),

as well as surface symmetry (a_{SS}) terms. Surprisingly enough, with just this few adjustable parameters being fitted to the available experimental data at that time, this simple analytic formula can still provide a decent qualitative description of a variety of nuclear chart properties including position estimates of the neutron- and proton-drip lines, predictions of the regions with alpha instability, or even zones of beta-delayed nucleon emission [118]. As a matter of fact, a re-fit of this liquid drop mass formula to the experimental masses resulted in a total rms error of $\sigma(1995) = 2.97$ MeV [119] when compared globally to the total number of 1768 known binding energies tabulated in the AME1995 [15] compilation. A very impressive result for such a simplistic model with only 5 free parameters. Nevertheless, any quantitative practical applications of the LDM-like formula are unsuitable due to a lack of accounting for the shell-effects, which leads to large local deviations of the predicted and experimental binding energies in different regions of the nuclear chart.

2.3.2 Microscopic corrections and the FRDM mass model

A key improvement to this purely macroscopic concept of LDM was made through its augmentation with phenomenological microscopic corrections. The initial step in this direction was made by Myers and Swiatecki in 1966 [120], when a simple algebraic shell-correction was introduced to create a "bunching" effect of the originally equidistant distribution of single-particle levels to induce a series of band gaps at the observed magic numbers. Besides that, the pairing effects were included with a simple phenomelogical term $\sim A^{-1/2}$, which was either added to the total binding energy for doubly even nuclei, subtracted for the doubly odd ones, or put to zero otherwise. Besides these microscopic add-ons, the final Myers-Swiatecki mass formula departed from the spherical symmetry by incorporating a shape parametrization into the surface and Coulomb terms of Eq. (2.13). Already these relatively simple shape-dependent corrections predicted the island of stability in superheavy nuclei, as well as preceded the discovery of many fission isomers in the region of heavy nuclei [121]. Later, the Strutinsky theorem [122], which can be viewed as an approximation to the Hartree-Fock (HF) method [123], offered a much firmer theoretical foundation of these microscopic augmentations with the so-called Strutinsky's shell-correction method [124]. The total binding energy could now be split into a smoothly varying macroscopic term and a microscopic term representing local fluctuations due to shell and pairing corrections – both being a function of *not* only A and Z, but also of a set of deformation parameters β, characterizing the shape of the nucleus

$$E(A, Z, \beta) = E_{mac}(A, Z, \beta) + E_{s+p}(A, Z, \beta). \tag{2.14}$$

The significance of these upgrades was astonishing, as the rms discrepancy between theory and experiment has dropped straight down to about 1 MeV [119]. The idea of artificial reconciliation of the seemingly opposite approaches of LDM and shell-effects marked off the period of the so called microscopic-macroscopic (mic-mac) mass formulas – the time, during which the full HF method (naturally unifying both parts) remained computationally impracticable. The continuous refinements and extensions of this hybrid approach finally resulted in 1992 in a very successful universal mass formula, the finite-range droplet model (FRDM) [125]. The FRDM took both the mic- and the mac-parts of the generic formula in Eq. (2.14) to the most sophisticated level of complexity. The macroscopic part was basically a generalization of LDM, introducing (among others)

refined Coulomb, Wigner and charge-asymmetry terms, and allowing different radii for neutron and proton distributions (neutron skin), as well as introducing finite-range surface effects [126] and finite compressibility [127] into the mass model. The microscopic part included the Strutinsky's shell-correction and the BCS pairing-correction [128]. The FRDM model of 1992 comprised of 19 adjustable parameters (out of a total number of 31 independent parameters [119]) directly fitted to the experimental masses listed in the AME1995 mass compilation, resulting in a rms error of $\sigma(1995) = 0.669$ MeV [125]. With the subsequent increase of computational power, a much finer optimization and minimization procedures became possible, resulting in a re-determination of many model parameters to boost the accuracy of the new FRDM mass formula of 2011 even further to $\sigma(2003) = 0.570$ MeV [129] when compared to the AME2003 [22] data.

2.3.3 ETFSI and Weizsäcker-Skyrme mic-mac mass models

An attempt to achieve a stronger consolidation between the mic- and the mac-parts of FRDM formula resulted in the development of two quite successful mass models: the extended Thomas-Fermi plus Strutinsky integral (ETFSI) [130] formalism, and a more recent Weizsäcker-Skyrme (WS) [131] mass model. In ETFSI approach, the macroscopic liquid-drop part emerges conveniently as a fourth-order approximation of the extended Thomas-Fermi (ETF) expression [132] for the binding energies, while the shell-corrections are addressed by the integral form of the Strutinsky's theorem. With both parts being based on the same Skyrme-type functional, the basic formal connection between the two could finally be established. One of the final refinements to the ETFSI formalism, before it was effectively made redundant by HF calculations, resulted in the ETFSI-2 mass table [133] with an rms deviation of $\sigma(2012) = 0.690$ MeV [112] when compared to the latest AME2012 [13, 14] database. In the WS scheme, the ETF approximation enters the parametrization procedure for the nuclear deformation corrections, which are combined with a modified spherical LDM expression for the macroscopic part, whereas the microscopic part is based on the Strutinsky's procedure and some other subtle phenomenological microscopic corrections. The latest version of WS scheme, denoted WS3 [134], is based on 16 variational model parameters and managed to yield an impressive $\sigma(2012) = 0.335$ MeV [112]. Meanwhile, as in the case of EFTSI, with the same Skyrme-type force eventually underlying both the mic- and the mac-terms, a much greater unification of the the two could be achieved here as well, avoiding thereby a lot of ambiguities of the FRDM approach (see, for example, Chap. 2.3 of Ref. [132] for details). Nevertheless, the ETFSI and WS mass models still remain members of the mic-mac family, offering a more credible microscopic solution compared with FRDM, but in the same time allowing to perform much faster large-scale calculations than with the computationally heavier Hartree-Fock methods.

2.3.4 The Duflo-Zuker mass formula

Another approach that is *per se* more fundamental than the ones of the mic-mac models, but still not strictly microscopic, is the Duflo-Zucker (DZ) mass formula [135, 136]. Although that the nucleonic interaction does not appear explicitly, the DZ method assumes an existence of such a well-behaved two-body pseudopotential that inside a nucleus creates a smooth mean-field potential plus a residual two-body interaction. The assumed effective Hamiltonian can thus be separated into two terms – the monopole

plus the multipole part, *i.e.*

$$\mathcal{H}_{\text{eff}} = \mathcal{H}_m + \mathcal{H}_M. \tag{2.15}$$

The former term provides the single-particle description necessary for a Hartree-Fock calculation, and generally is capable to reproduce exact energies of the closed shells, as well as their 1p-1h states [136]. The latter term contains pairing, quadrupole, and other contributions to describe the collective behavior, and can, in principle, be extracted parameter-free from a realistic NN-interaction [136]. The monopole part should, however, be treated purely phenomenologically as to ensure proper saturation properties of the NN-forces, and can be viewed as a functional of the orbital occupancies that are being sequentially filled in accordance with the shell model description [137]. Thus rather than the effective interaction itself, it is these monopole and multipole parts of the Hamiltonian that are being parametrized using various symmetry and scaling arguments. Finally, the deformed nuclei are treated by directly parametrizing their observed energy patterns in junction with a number of simple arguments about their structure [135]. The most recent mass table, calculated with DZ31 mass model (having 31 independent parameters) resulted in an rms of $\sigma(2012) = 0.397$ MeV [112].

2.4 Microscopic mean-field models with effective interactions

Despite of the relatively strong descriptive power of the FRDM mass formula, the incoherent link between the liquid-drop part and the shell-corrections, as well as a number of some other deficiencies [6], question the reliability and predictive strength when extrapolating towards the neutron-rich extremes of the nuclear chart. A much greater reconciliation between the mic- and the mac-part has eventually been achieved in other semi-empirical models based on ETFSI and WS formalisms. However, all of the mic-mac models are largely based on some *ad hoc* modeling around known nuclei, whereas a more reliable mass model for the experimentally unknown nuclei should be as microscopic as possible.

Inspired by the success of the independent particle model (also known as non-interacting Shell Model [59]), the models mentioned in this section are based on the mean-field concept, and work at a microscopic level with nucleons as the relevant degrees of freedom. The interactions are employed in an effective phenomenological form. The system is then treated in either restricted space (the ISM approach), or in various forms of many-body wave functions (the SCMF methods).

2.4.1 The interacting Shell Model

The interacting Shell Model (ISM) [138] shares the same approach to the many-body problem as the NCSM method that was outlined in Chap. 2.2.5, but it introduces an inert core that is comprised of a number of inactive nucleons, which therefore reduces nucleonic degrees of freedom explicitly entering the calculation to make the problem computationally more tractable. To this end the conventional starting point is to introduce the concept of a mean-field, which allows to separate the initial many-body Hamiltonian H into two parts, as

$$H = H_0 + V_{\text{res}}, \tag{2.16}$$

where the one-body single-particle field $H_0 = \sum_i (T_i + U_i)$ describes the ensemble of A non-interacting nucleons with kinetic energies T_i moving independently in an assumed average mean-field potential U_i generated by themselves; the $V_{\text{res}} = \sum_{i<j} V_{ij} - \sum_i U_i$ represent the residual interaction among the nucleons, and can formally be written as a difference between the mutual two-body (and possibly higher-order) interaction and the generated mean-field. Near the nuclear shell-closures the mean-field potential can usually be chosen in such a way, that the residual interaction will be small and can be neglected altogether, resulting in the independent particle model (IPM) [59]. However, as the number of protons and neutrons start to deviate further from the magic numbers, one can no more neglect the residual interaction that breaks the orbital energy degeneracy [138]. The corrections to the mean-field solutions are then obtained by diagonalizing the initial Hamiltonian H in the basis of Slater determinants representing all possible particle-hole excitations of the nucleons in the valence space. The shell model wavefunction is then comprised of IPM-configurations mixed together by the V_{res} interaction, and can formally be written in form of Eq. (2.6) assuming that the C_n operator can now only generate np-nh excitations in the valence orbitals, leaving the core orbitals always full. In order to keep the model space finite, the valence orbitals are often restricted from above by the so-called external space, containing orbitals that are kept constantly empty. The realistic interaction between the nucleons has to be renormalized in order to account for the effects due to the presence of the core and the external space [139]. The derived effective interaction is then very much dependent on the model space itself, and is typically established in form of two-body matrix elements that are phenomenologically tuned to reproduce experimental data. For example, calculations of the *sd*-shell nuclei, that are built upon ^{16}O inert core and have mass range of $16 \leq A \leq 40$, commonly employ the so-called Universal-*sd* (USD) [140] interaction, which is comprised of 66 parameters fitted to 447 experimental ground- and excited-state energies. The USD was later enhanced by re-adjusting the parameters to a larger set of experimental data covering all experimentally known *sd*-shell nuclei using an improved fitting procedure to provide the updated USDA and USDB interactions [141]. In the case of *fp*-shell nuclei, spanning the region of $40 \leq A \leq 80$ with ^{40}Ca as an inert core, there are several sets of commonly employed effective interactions, like GXPF1 [142] and KB3G [143].

On the whole, despite the built-in capacity of ISM to provide an accurate description of *not* only masses and separation energies, but also of various spectroscopic nuclear properties, the ISM approach is lacking a universal interaction, and therefore its predictive power is generally restricted only to the local regions of the nuclear chart [144, 145]. Moreover, analogous to the NCSM method, the dimensions of ISM calculations grow extremely fast, appealing to various advanced diagonalization schemes [146] or Shell Model Monte Carlo (SMMC) [147, 148] techniques to treat the heavier nuclear systems. However, even despite these enhancements, the ISM-based methods are still bound to nuclei in vicinity to the shell-closures [138], therefore also hindering its potential usage in the construction of a comprehensive mass table for the purposes of nuclear astrophysics.

2.4.2 Self-Consistent Mean-Field models

The self-consistent mean-field (SCMF) methods have been developing for the last 50 years, but initially were rather limited in the range of their applications [59], leaving the dominant role in the nuclear astrophysics calculations to the mic-mac formulas. In

contrast to ISM, the SCMF approach took a different path within the microscopic formulation, and was meant to determine an unprejudiced and self-consistent single-particle potential, suitable for the qualitative explanation of various nuclear properties. The first attempts in this direction involved various interaction schemes extracted directly from the bare NN–interaction. The calculations were able to reproduce some of the basic nuclear properties, such as masses and radii, but suffered greatly in the accuracy [146]. A significant improvement was achieved by proceeding in a more phenomenological way by adopting an effective interaction instead. The form of the effective interaction was motivated by *ab initio* principles, but then it was specifically adapted for the use in the mean-field calculations by extensive fits to the available nuclear structure data.

Further upgrade was done with an establishment of the density-dependent interactions, which became the pillars of what it is currently known as nuclear energy-density functional (EDF) methods [146], where the nuclear ground-state energy is obtained according to variational principle (introduced in Sec. 2.2.3) by minimization of the total energy density functional $\delta E[\rho] = 0$, which is discussed in detail in Sec. 4.1.3. These procedures turned out successful in *not* only describing the bulk properties of known nuclei, but also provided excellent results for other phenomena, to which they were not tailored at all, as, *e.g.*, rotational bands in isotopes around Dy and Hg, or systematic calculation of super-heavy nuclei [146]. Moreover, several past decades brought a lot of new experimental results in regions far from stability, triggering further improvements in predictive power of the EDF methods.

The Skyrme-force, that we discuss in detail in Sec. 3.1, has seen many parametrizations during the past decades. Two of the latest Skyrme-HFB models, labeled HFB-24 and HFB-25 [21], were able to provide the rms deviations of $\sigma(2012) = 0.55$ MeV and $\sigma(2012) = 0.54$ MeV, respectively, which represent the best values ever achieved within the mean-field framework [149]. Another set of EDFs based on Skyrme interactions have recently been developed in the UNEDF collaboration [150]. This sizeable project extensively exploited high-performance computing and resulted in a row of Skyrme-type parametrizations, like UNEDF0 [151] and UNEDF1 [152], where a special emphasis was made on a thorough study of sensitivity of the EDF-parameters, advanced code optimizations, as well as assertions of uncertainties in model predictions. The project concluded with a construction of the most tightly constrained Skyrme-parametrization for all-around calculations, denoted as UNEDF2 [153], which also marked the end of the Skyrme EDF exploration not only within the UNEDF project, but generally outlining the limits of current EDF methods [153]. In order to introduce further improvements to the EDF approaches, we address some of the most important beyond-mean-field (BMF) extensions in Chap. 6 in the context of the Gogny EDF. Contrary to the Skyrme's zero-range, the Gogny functional introduces a number of finite-range components to better reproduce the realistic nucleonic interactions. While the Gogny force is thoroughly discussed in Sec. 3.2, it should be mentioned here that one its recent parametrizations, denoted as D1M [154], resulted in the most successful Gogny-Hartree-Fock-Bogolyubov mass table with an rms deviation of $\sigma(2003) = 0.798$ MeV. Besides the non-relativistic microscopic methods, a wide attention was recently received by the relativistic mean-field models, which we outline in Sec. 3.3. However, despite of an evident success in describing a various number of nuclear phenomena [146], the currently estimated deviations of the RMF models from the known masses are about 2 MeV [112].

Altogether, the present SCMF models are comprised of the three "standard" interactions – Skyrme, Gogny, and RMF – and we turn to a more detailed discussion of them in the next chapter.

3 Effective interactions for SCMF models

While the *bare* NN potentials have been designed and adjusted to provide high-precision description of the nucleon-nucleon scattering data and various properties of few-body systems, as was already mentioned previously (Sec. 2.2), their divergent off-diagonal matrix elements cause substantial numerical problems for various nuclear many-body methods. Even the softer chiral potentials exhibit significant coupling of low- to high-momenta states, which renders their implementation inconvernient due to the slow convergence rate of calculations. However, given that a nucleon inside a nuclear many-body system interact in the presence of many other nucleons, it does not necessarily experience the strong repulsion due to significant in-medium restrictions on the scattering phase space [59, 155]. This idea motivated an introduction of soft *effective* nuclear interactions, that are numerically well-behaved and specifically constructed for the self-consistent mean-field (SCMF) approach. The most widespread of such effective forces are the non-relativistic density-dependent Skyrme and Gogny interactions. Their generic form is motivated by the fundamental NN potential and about a dozen of free parameters that they possess are carefully adjusted to various experimental data across the nuclear chart. Meanwhile, an introduction of density-dependent term not only allows to omit some of the non-trivial important operators of the realistic interaction (such as tensor force necessary to properly reproduce NN scattering phase shifts and deuteron quadrupole moment [156]), but it also makes it possible to effectively absorb in itself many unaccounted three-body and higher-order in-medium correlations [59], while still ensuring high-precision level for calculations of ground-state properties at low numerical cost.

In the following Sec. 3.1 and Sec. 3.2 we briefly introduce the zero-range Skyrme, and the finite-range Gogny effective interactions. We also concisely mention the main ideas of effective interactions based on relativistic Lagrangians in Sec. 3.3. For a comprehensive review of the mentioned mean-field models, see, for example, Ref. [146].

3.1 Zero-range Skyrme interactions

The phenomenological effective interactions of the Skyrme type are among the most widespread in the nuclear structure calculations. The interaction was first put forward by Tony Skyrme and John Bell in 1956 [157–159] to capture the key features of an in-medium interaction with an inclusion of a three-body term

$$V = \sum_{i<j} V^{(2)}_{i,j} + \sum_{i<j<k} V^{(3)}_{i,j,k}. \tag{3.1}$$

Since the actual nuclear force is of short-range nature, Skyrme argued that the dominant contribution to the effective interaction comes from a contact potential, so that the general two- and three-body interactions can be reduced to

$$\begin{aligned} V_{i,j}^{(2)} &= V^{(2)}(k,k')\delta(\vec{r}_i-\vec{r}_j) \\ V_{i,j,k}^{(3)} &= t_3\delta(\vec{r}_i-\vec{r}_j)\delta(\vec{r}_j-\vec{r}_k), \end{aligned} \tag{3.2}$$

with t_3 being an unknown constant. Mathematically, the implementation of a δ-force leads to an enormous simplification in the subsequent numerical implementations. From the physical point of view, the actual finite-range character of the inter-nucleon force enters indirectly through the dependence on *relative* momenta of interacting nucleons [160]. That is also the only possible type of momentum dependence for a potential due to the Galilean invariance and, owing to the low-energy character of the effective interaction, the two-body term can be expanded [158, 161] in terms of powers of k and k' as

$$V^{(2)}(k,k') = c_0 + \frac{1}{2}c_1[\vec{k}'^2+\vec{k}^2] + c_2\vec{k}'\cdot\vec{k} + \cdots, \tag{3.3}$$

where in the classical Skyrme-type parametrizations the expansion terms are kept only up to the second order. Concerning the three-body term, it was subsequentially shown in 1972 by Vautherin and Brink [162] that, for the purposes of mean-field calculations in cases of spin-saturated doubly even nuclei, it is equivalent to a two-body density-dependent interaction

$$V_{i,j}^{(3)} = \frac{1}{6}t_3(1+x_3\hat{P}_\sigma)\delta(\vec{r}_i-\vec{r}_j)\rho\left(\frac{\vec{r}_i+\vec{r}_j}{2}\right), \tag{3.4}$$

which later has been modified [163, 164] to introduce a power dependence on the density, so that the widely accepted standard form of the Skyrme force could be written as

$$\begin{aligned} V_{i,j}^{(\mathrm{Sk})} &= t_0(1+x_0\hat{P}_\sigma)\delta(\vec{r}_i-\vec{r}_j) \\ &+ \frac{1}{2}t_1(1+x_1\hat{P}_\sigma)\left[\delta(\vec{r}_i-\vec{r}_j)k^2 + k'^2\delta(\vec{r}_i-\vec{r}_j)\right] \\ &+ t_2(1+x_2\hat{P}_\sigma)\vec{k}'\cdot\delta(\vec{r}_i-\vec{r}_j)\vec{k} \\ &+ iW_0(\vec{\sigma}_i+\vec{\sigma}_j)\cdot\left[\vec{k}'\times\delta(\vec{r}_i-\vec{r}_j)\vec{k}\right] \\ &+ \frac{1}{6}t_3(1+x_3\hat{P}_\sigma)\delta(\vec{r}_i-\vec{r}_j)\rho^\alpha\left(\frac{\vec{r}_i+\vec{r}_j}{2}\right), \end{aligned} \tag{3.5}$$

where $\hat{P}_\sigma = (1+\vec{\sigma}_i\cdot\vec{\sigma}_j)/2$ is the spin-exchange operator, the $\vec{\sigma}$ are the Pauli spin matrices, the $\vec{k} = (\vec{\nabla}_i - \vec{\nabla}_j)/2i$ denotes the relative wave vector operator acting on right, whereas $\vec{k}' = -(\vec{\nabla}_i - \vec{\nabla}_j)/2i$ corresponds to a similar operator acting on the left. The $t_{0,1,2,3}$, $x_{0,1,2,3}$, W_0, and α are the arbitrary parameters that are adjusted to reproduce various experimental observables. The first line is the so-called central term which contains a pure δ–force of the interaction; the two next lines represent the effective range by means of kinetic-dependent terms; the forth line is the spin-orbit part of the interaction; while the last line is the part of the Skyrme force that explicitely depends of the nuclear density ρ, and is usially written with a 1/6 pre-factor due to historical reasons. The interaction can be regarded as a form of phenomenological G–matrix approximation which accounts for in-medium many-body effects by the virtue of

the density dependence [162]. Actually, the introduction of this density term turned out to be crucial in order to achieve the correct saturation properties of nuclear matter and is the primary reason for the success of the Skyrme interaction, for which there exists nowadays about 250 variants of different parametrizations (*e.g.*, see Refs. [165, 166]). Another benefit comes from its zero-range structure, that, as was already mentioned, not only simplifies calculations for finite nuclear systems, but also grands possibility to derive many analytical expression for different properties of an infinite nuclear matter, which explains the widespread employment of numerous Skyrme force parametrizations in astrophysical calculations, such as neutron star equation of states (*e.g.*, see Ref. [167] for a review). However, apart from a few exceptions (*e.g.* SkP parametrization [168]), the Skyrme interaction is always used in the particle-hole channel, as it does not provide the correct pairing properties [168, 169], so the particle-particle channel during calculations is supplemented independently to reproduce, for example, experimental energy gaps [170]. Moreover, some of the standard Skyrme parametrizations have some unresolved trends in the isovector channel (*e.g.* systematic underbinding in very neutron-rich nuclei [146, 171]), and there is also a number of nuclear observables (such as separation-energies) that cannot be satisfactory reproduced especially in cases of unstable nuclei [165]. The choice of zero-range interaction also backfires when used in the beyond-mean-field calculations, as contributions to the total energy from, for example, second-order corrections, display an ultraviolet divergence [172, 173]. In fact, the divergencies can already occur at the HFB level when using Skyrme force in the pairing channel as well [174]. To resolve this issue, various regularization techniques were proposed [169, 174, 175]. Other steps were taken in order to enhance the standard Skyrme interaction by various modifications [146], which included introduction of higher-order derivative components [176] or augmentation with alternative density-dependent terms [177, 178]. An in all, much effort was recently dedicated to improve the performance of the standard and extended Skyrme-type functionals [179–183].

3.2 Finite-range Gogny interactions

Even though that the effective interactions of the Skyrme type have been successfully implemented in nuclear structure calculations, it appeared to be questionable if such zero-range interactions are able to adequately simulate the finite-range nature of the realistic effective nuclear force [59]. An incorporation of a long-range terms into an effective interaction is essential for circumventing numerical complications arising from UV divergences in the pairing channel, as well as at the beyond-mean-field level [172]. Moreover, it has been recently shown that k^2-dependence of the Skyrme mean-field is not consistent with the analysis of the mean-field extracted from the heavy-ion collision experiments [184], which is not the case for a mean-field resulting from a finite-range interaction [185, 186].

In 1967 Brink and Boeker [187] suggested a finite-range type of effective interactions consistent of two Gaussians with shorter and longer range. The initial calculations with this interaction were not able to correctly reproduce the nuclear binding energies on the Hartree-Fock level [146] until 1973, when Daniel Gogny proposed [188, 189] to augment the interaction with a spin-orbit and a density-dependent term. Subsequently, with an introduction in 1980 by Dechargé and Gogny [190] of the first comprehensive parametrization (labeled as *D1*) to finally provide satisfactory results for calculations of

some relevant nuclear binding energies and radii, the Gogny interaction took its standard form

$$\begin{aligned} V_{i,j}^{(\mathrm{G})} &= \sum_{n=1}^{2} e^{-(\vec{r}_i-\vec{r}_j)^2/\mu_n^2}(W_n + B_n\hat{P}_\sigma - H_n\hat{P}_\tau - M_n\hat{P}_\sigma\hat{P}_\tau) \\ &+ iW_{ls}(\vec{\sigma}_i+\vec{\sigma}_j)\cdot\left[\vec{k}'\times\delta(\vec{r}_i-\vec{r}_j)\vec{k}\right] \\ &+ t_3(1+x_0\hat{P}_\sigma)\delta(\vec{r}_i-\vec{r}_j)\rho^\alpha\left(\frac{\vec{r}_i+\vec{r}_j}{2}\right), \end{aligned} \tag{3.6}$$

where $\hat{P}_\sigma = (1+\vec{\sigma}_i\cdot\vec{\sigma}_j)/2$ is the spin-exchange operator, $\hat{P}_\tau = (1+\vec{\tau}_i\cdot\vec{\tau}_j)/2$ the isospin-exchange operator, while $\vec{\sigma}$ and $\vec{\tau}$ are the Pauli spin and isospin matrices, respectively. Similar to the Skyrme force, the $\vec{k}'$ and $\vec{k}$ are the relative momentum operators acting on the either sides of the expression. The quantities B_n, H_n, M_n, W_n, μ_n (with $n = 1, 2$), as well as t_3, x_0, α and W_{ls} are the free parameters adjusted to various properties of finite nuclei and nuclear matter.

The first line of Eq. (3.6) corresponds to the finite-range (central) term of the force built up from two Gaussians that simulate short and intermediate ranges of the nuclear interaction and contain all possible combinations of spin and isospin exchange operators. The effective range is defined by the standard deviations of the Gaussians, which are usually chosen in the intervals of $\mu_1 \approx 0.5 - 0.8$ fm and $\mu_2 \approx 1.0 - 1.2$ fm. The choice of the Gaussian-form was stipulated by their particular computational advantages when working with harmonic oscillator basis for practical calculations. The second line is the spin-orbit term of the interaction, and the last line correspoding to the density-dependent part – both being identical to the corresponding ones in the Skyrme interaction of Eq. (3.5). Thus, in principle, the Gogny potential can be regarded as a Skyrme-type one, where the spacial part of the zero-range central term was substituted with a combination of two Gaussians. In fact, the Skyrme central terms can be recovered by momentum expansion of the Gaussian central and spin-orbit terms up to the second order [162]. However, in order to get satisfactory compressibility properties of symmetric nuclear matter, the α parameter is usually fixed at $\alpha = 1/3$ [191]. Moreover, in order to avoid the aforementioned problem of divergent behavior with Skyrme interaction in the particle-particle channel, the x_0 parameter preceding the $\hat{P}_\sigma$ operator in the density-dependent part is typically fixed such that $x_0 = 1$ [146]. Despite the resulting zero contribution from this term to the $T = 1$ pairing channel, this allows (contrary to the Skyrme interaction) to implement Gogny force self-consistently in both mean-field and pairing channels in a straightforward way. In fact, because of this property, the Gogny interaction is sometimes used in the particle-particle channel to augment the Hartree-Fock calculations with otherwise divergent interactions in the pairing channel, like the Skyrme-type forces or some relativistic models [192].

With the x_0 and α having been fixed in the original Gogny D1 interaction, the remaining t_0 parameter of the density-dependent part was established by considering the energy splitting of $d_{3/2} - p_{1/2}$ levels in ^{16}O [193]. Also the W_{ls} parameter, defining the strength of the spin-orbit term was established independently of other parameters in order to reproduce the $p_{3/2} - p_{1/2}$ energy splitting of ^{16}O [190]. Finally, the parameters of the central part of the force, namely $W_{1,2}$, $B_{1,2}$, $H_{1,2}$ and $M_{1,2}$, were fitted to, for example, obtain correct binding energies and radii of ^{16}O and ^{90}Zr closed-shell nuclei, energy difference between the neutron $2s_{1/2}$ and proton $2s_{1/2}$ states of ^{48}Ca, some odd-

even pairing systematics of Sn-isotopes, as well as saturation properties of infinite nuclear matter [190, 191]. However, as it turned out later, the D1 parametrization could not accurately reproduce the barrier heights of actinides, and in particular was overestimating the one of ^{240}Pu [194]. This was later accounted for by J.F. Berger, M. Girod, and D. Gogny in the updated D1S version of Gogny parametrization [193]. Although that the D1S interaction was primarily devised for fission calculations, it eventually became very successful and widespead for various nuclear structure calculations as well. However, the D1S parametrization suffers from predicting a relatively low saturation symmetry energy [195], which leads to, among others, unstable neutron matter calculations [196], and a distinctive systematic underbinding of the neutron-rich isotopes relative to the experimental values [191, 197]. The latter fact is also clearly observed in our calculations presented in Sec. 5.3. This deficiency was corrected in the subsequent extensions to the original form of the Gogny functional, such as Gogny D1P [198], which included a second zero-range density-dependent term and aimed for a more realistic neutron matter equation of state at high densities. Eventually, the aforementioned isotonic drift of the calculated binding energies was accounted for with the subsequent Gogny D1N [191] force, which retained its original Gogny-form of Eq. (3.6). Finally, the most recent Gogny D1M parametrization, that was introduced in 2009 by S. Goriely *et. al.* [154], was specifically tailored for HFB calculations of nuclear binding energies and radii, and the fitting procedure for the parameter set of the interaction explicitely included corrections for the quadrupole correlation energies within the 5-dimensional collective Hamiltonian (5DCH) approach [199]. The Gogny D1M parametrization was not only able to produce the nuclear mass table in excellent agreement with the experimentally known binding energies [154], but has also shown a good consistensy in nuclear and neutron matter properties with respect to microscopic calculations that employed realistic two- and three-body forces [197]. All in total there are about a dozen of Gogny parametrization sets that can be found in the literature nowadays, while the most important ones for the nuclear structure calculations that we implement or discuss in our subsequent analysis are summarized in the Table 3.1.

	n	μ_n [fm]	W_n	B_n	H_n	M_n [MeV]	
D1	1	0.7	−402.4	−100.0	−496.2	−23.56	$W_{LS} = 115$ [MeV fm^5]
	2	1.2	−21.30	−11.77	37.27	−68.81	$t_3 = 1350$ [MeV fm^4]
D1S	1	0.7	−1720.3	1300.00	−1813.53	1397.60	$W_{LS} = 130$ [MeV fm^5]
	2	1.2	103.64	−163.48	162.81	−223.93	$t_3 = 1390$ [MeV fm^4]
D1N	1	0.8	−2047.61	1700.00	−2414.93	1519.35	$W_{LS} = 115$ [MeV fm^5]
	2	1.2	293.02	−300.78	414.59	−316.84	$t_3 = 1609$ [MeV fm^4]
D1M	1	0.5	−12797.57	14048.85	−15144.43	11963.89	$W_{LS} = 115$ [MeV fm^5]
	2	1.0	490.95	−752.27	675.12	−693.57	$t_3 = 1562$ [MeV fm^4]

Table 3.1: Parameter sets of Gogny D1 [190], D1S [193], D1N [191], and D1M [154] interactions; all Gogny parametrizations listed here have $x_0 = 1$ and $\alpha = 1/3$.

3.3 Relativistic mean-field interactions

The success of non-relativistic mean-field models in studying low-energy nuclear structure problems can be easily justified if we estimate the largest kinetic energy of the nucleons $T_{\max}$, which inside the nucleus follows from the Fermi momentum $k_{\mathrm{F}} \approx 1.4$ fm^{-1}, and can be estimated [161] to be of the order of

$$T_{\max} = \frac{\hbar^2 k_F^2}{2m} \approx 38 \text{ MeV}. \tag{3.7}$$

That is indeed much less than the nucleon rest mass of ~ 1 GeV, and corresponds to a velocity of merely $v \approx 0.29c$. This fact renders the relativistic kinematics to be of minor importance. However, an implementation of relativistic models in studying various nuclear phenomena can be stipulated by a number of important points:

- Even though that the effective depth of the non-relativistic nuclear potential is typically of the order of 50 MeV, it is the outcome of an intricate cancellation between the much larger long-range attractive scalar field of ~ 400 MeV and a short-range repulsive vector field of ~ 350 MeV [146, 200].
- The spin-orbit part of the interaction is a inherent attribute of Dirac-Lorenz structure of effective Lagrangian, and therefore emerges naturally from the relativistic description. Moreover, while the attractive and repulsive fields nearly cancel each other out in case of the nuclear potential, they effectively add up for the spin-orbit part of the force, thereby also explaining the origin of its relatively large magnitude [146, 200].
- The density-dependent interactions among nucleons originate naturally from the Lorentz covariance of the relativistic formalism. Moreover, the non-relativistic reduction reveals non-central and non-local aspects inherent to the Hartree formalism [201].
- The saturation properties of nuclear matter can easily be described within the simple relativistic models [202, 203], while the formalism may be naturally extrapolated to regimes of highly condensed hot matter [161].
- Finally, the important concept of pseudospin symmetry [204], which explains a number of subtle phenomena in nuclear structure, can be recognized as a relativistic symmetry [205, 206].

The initial ideas of a phenomenological relativistic theory date back to 1956, when H.-P. Dürr [207] formulated the relativistically invariant framework that reproduced saturation properties of nuclear matter and showed how a strong spin-orbit coupling naturally emerges as a relativistic phenomena. The chosen approach gained further grounds in 1974 when J.D. Walecka developed the $\sigma - \omega$ model and successfully applied it to highly condensed matter [208]. Since then the relativistic approach was further enhanced and actively used with great success for studying finite nuclear systems using relativistic mean-field (RMF) models [209, 210], as well as with recently developed relativistic Hartree-Fock (RHF) schemes [211, 212].

Regarding the ground-state properties of finite nuclei, the RMF models proved to perform on the same high-quality level as the approaches based on Skyrme or Gogny

functionals. The basic idea of any RMF model is similar to the non-relativistic mean-field picture, but the non-interacting (quasi-)particle states become the four-component Dirac spinors, whose dynamics is governed by the Dirac equation. Additional degrees of freedom are the mesons (usually σ, ω, and ρ), as well as the photon field – they mediate interaction between the nucleons and effectively generate the mean-field potential. Similar to the non-relativistic case, there are two distinctive families of relativistic models: one with an effective finite-range interaction, and the zero-range, or point-like, forces. The finite-range models are, however, much more widespread. Their starting point is a phenomenological Lagrangian density, which has to fulfill the QCD symmetries. The general form of the Lagrangian density consists of both the nucleon and meson fields, as well as their coupling term

$$\mathcal{L} = \mathcal{L}_{\mathrm{N}} + \mathcal{L}_{\mathrm{meson}} + \mathcal{L}_{\mathrm{coup}}. \tag{3.8}$$

The first term is the free Lagrangian for the nucleon, which in covariant notation is

$$\mathcal{L}_{\mathrm{N}} = \bar{\psi}(i\gamma^{\mu}\partial_{\mu} - m_{\mathrm{N}})\psi, \tag{3.9}$$

where γ^{μ} are the Dirac matrices, m_{N} is the bare nucleon mass, and ψ is the nucleon field.

As for the free Lagrangian for the meson and photon fields, it can be written as

$$\begin{aligned} \mathcal{L}_{\mathrm{meson}} &= \frac{1}{2}\partial_{\mu}\sigma\partial^{\mu}\sigma - \frac{1}{2}m_{\sigma}^{2}\sigma^{2} - \frac{1}{4}\Omega_{\mu\nu}\Omega^{\mu\nu} + \frac{1}{2}m_{\omega}^{2}\omega_{\mu}\omega^{\mu} \\ &- \frac{1}{4}\vec{R}_{\mu\nu}\vec{R}^{\mu\nu} + \frac{1}{2}m_{\rho}^{2}\vec{\rho}_{\mu}\vec{\rho}^{\mu} - \frac{1}{4}F_{\mu\nu}F^{\mu\nu}, \end{aligned} \tag{3.10}$$

with the field tensors corresponding to ω, ρ, and γ fields defined as

$$\begin{aligned} \Omega_{\mu\nu} &= \partial_{\mu}\omega_{\nu} - \partial_{\nu}\omega_{\mu}, \\ \vec{R}_{\mu\nu} &= \partial_{\mu}\vec{\rho}_{\nu} - \partial_{\nu}\vec{\rho}_{\mu}, \\ F_{\mu\nu} &= \partial_{\mu}A_{\nu} - \partial_{\nu}A_{\mu}. \end{aligned} \tag{3.11}$$

Finally, the Lagrangian for nucleon-meson interaction is of the form

$$\mathcal{L}_{\mathrm{coup}} = -g_{\sigma}\bar{\psi}\sigma\psi - g_{\omega}\bar{\psi}\gamma\cdot\omega\psi - g_{\rho}\bar{\psi}\gamma\cdot\vec{\rho}\vec{\tau}\psi - e\bar{\psi}\gamma\cdot A\tau_{p}\psi, \tag{3.12}$$

where $\tau_p \equiv (1+\tau_3)/2$ is the isospin projection operator to provide γ-coupling only to the proton field, whereas g_σ, g_ω, and g_ρ are the corresponding meson coupling constants.

If one plugs in the known bare masses for nucleons, ω and ρ mesons, there are *only* four parameters, namely m_σ, g_σ, g_ω and g_ρ, to be adjusted to nuclear matter and finite nuclei properties. Despite that this initially enabled to describe the basic nuclear properties on a qualitative level, just like in the case of non-relativistic mean-field models, the density-dependence had to be explicitly introduced in order to correctly reproduce such essential nuclear phenomena, as incompressibility or surface properties of nuclear matter [146]. This can be implemented straighforwardly by making the coupling constants depend on the density [210], such that

$$g_{\sigma} \longrightarrow g_{\sigma}(\rho), \qquad g_{\omega} \longrightarrow g_{\omega}(\rho), \qquad g_{\rho} \longrightarrow g_{\rho}(\rho). \tag{3.13}$$

The density ρ is taken to be either a scalar density $\rho_s = \bar{\psi}\psi$ [203, 213], or the baryon density of Lorentz invariant form $\rho_b = \sqrt{j^\mu j_\mu}$ with vector current $j_\mu = \bar{\psi}\gamma_\mu\psi$ [200].

The other way to introduce effective density-dependence is by considering non-linear self-interactions among the meson fields [200]. In this case the mass terms of free mesons are replaced with the corresponding non-linear potentials. For example, in the popular and well-established self-coupling scheme of scalar field, introduced by Boguta and Bodmer [214], this is achieved by augmenting the Lagrangian with cubic and quartic contributions for the σ-meson, as

$$\frac{1}{2}m_\sigma^2\sigma^2 \quad \longrightarrow \quad U(\sigma) = \frac{1}{2}m_\sigma^2\sigma^2 + \frac{g_2}{3}\sigma^3 + \frac{g_3}{4}\sigma^4. \tag{3.14}$$

More recently, there were also self-coupling schemes introduced for vector mesons, resulting in appearances of, for example, $U(\sigma, \omega)$ potentials [215, 216]. However, most of these non-linear approaches suffer from stability problems at high densities [217] and, moreover, the rise questions of their physical foundation [213].

Despite all the success of the RMF models, the pairing is still a major problem: it is not possible to use the same meson-exchange forces straightforwardly both in the Hartree and pairing channels [209], and, just like the case of the Skyrme interaction, one has to either introduce an "active space" around Fermi level to cut off the encountered UV divergences, or implement another type of interaction for the pp–channel [146]. Since finite-range Gogny-type interactions provides a natural momentum cut-off, it has become customary to augment the RMF models with pairing correlations coming from the Gogny force. Nonetheless, it may appear problematic to extend such RMF models beyond the usual mean-field approximation [200].

4 Theoretical framework of the HFB approach and BMF methods

This chapter is devoted to the theoretical formalism which we extensively exploit throughout the subsequent chapters. We briefly recapitulate the non-relativistic self-consistent mean-field (SCMF) approach for describing the finite nuclear many-body quantum systems. We introduce the principle ideas of the Hartree-Fock-Bogolyubov (HFB) method and discuss the main properties of the implemented quasi-particle vacuum states in Sec. 4.1.1. In Sec. 4.1.2 we define the necessary ingredients of the HFB theory, and in Sec. 4.1.3 we make use of the variational principle to formally derive the HFB equations. The energy functional and its basic building blocks in form of mean- and pairing-fields are discussed in Sec. 4.1.4. Such aspects of practical applications as performing constrained HFB calculations to study nuclear deformations, as well as incorporations of the gradient method to iteratively solve the HFB equations are presented in Sec. 4.1.5 and Sec. 4.1.6. Finally, built on the HFB approach, we introduce extensions that go beyond the mean-field picture of non-interacting quasi-particles and present the generator coordinate method (GCM) in Sec. 4.2.1 to lay down the foundation for the particle-number and angular momentum projection techniques in Sec. 4.2.2 and Sec. 4.2.3. Finally, we formulate the symmetry-conserving configuration mixing (SCCM) method in Sec. 4.2.4. For a more detailed overview of these beyond-mean-field (BMF) approaches, we refer to the corresponding chapters in Refs. [59, 146, 161, 170, 218, 219].

4.1 Hartree-Fock-Bogolyubov formalism

The apparent success of the phenomenological shell model [220, 221] to qualitatively describe many experimental properties of the atomic nuclei greatly motivates to adopt the independent-particle picture to solve the many-body nuclear problem. In such approach a nucleon is envisioned to move freely inside the nucleus and interact only via average mean-field potential generated effectively by the rest of the nucleons. All the necessary tools for this approximation is provided by the Hartree-Fock (HF) approach [59], that searches for the best possible approximation of the exact many-body wave function in form of a Slater determinant comprised of single-particle wave functions. The HF method relies on the Ritz variational principle [222, 223] to derive the mean-field potential from an appropriate effective nucleon interaction. This method naturally takes into account the long-range part of the nuclear force or, equivalently, the particle-hole correlations between the constituent nucleons, and can be applied to treat the closed-shell nuclei. However, in the unfilled shells additional pairing correlations caused by the short-range

part of the nuclear force become particularly important. The pairing effects can be formally accounted for withing the Bardeen-Cooper-Schrieffer (BCS) framework [128], which takes a predefined set of single particle states and, provided a pairing interaction, generates a many-body wave function of the special form built of Cooper-pairs with partial occupation probabilities [59, 161]. The HF and BCS methods are usually used together, where the HF calculations generate the single particle states that are used as an input for the BCS model [168]. While such HF+BCS model requires two different types of calculations and performs well only near the valley of stability [224], both HF and BCS approaches can be generalized and unified within the Hartree-Fock-Bogolyubov (HFB) formalism to self-consistently describe the nuclei across the whole nuclear chart. The HFB method assumes an approximation to the exact many-body wave function in form of the most general Slater determinant comprised of single *quasi*-particle states, which accounts for as many particle correlations as possible while still maintaining the simple static non-interacting (quasi)-particle picture.

4.1.1 Bogolyubov transformation and HFB state

The Bogolyubov quasi-particle [223, 225] creation and annihilation operators, $\beta_\mu^\dagger$ and β_μ, are defined in terms of the single-particle operators, $c_k^\dagger$ and c_k, by the most general linear $\{c_k^\dagger, c_k\} \longrightarrow \{\beta_\mu^\dagger, \beta_\mu\}$ transformation

$$\begin{aligned} \beta_\mu^\dagger &= \sum_i U_{i\mu} c_i^\dagger + V_{i\mu} c_i, \\ \beta_\mu &= \sum_i U_{i\mu}^* c_i + V_{i\mu}^* c_i^\dagger, \end{aligned} \tag{4.1}$$

where U and V are the matrix coefficients of the Bogolyubov transformation [59].

In practical calculations, the infinite single-particle Hilbert space has to be truncated, so that both indices μ and i run up to certain maximum value M. The Bogolyubov transformation can then be conveniently recast into a block-matrix form with dimensions twice that of the chosen configuration space:

$$\begin{pmatrix} \beta \\ \beta^\dagger \end{pmatrix} = \begin{pmatrix} U^+ & V^+ \\ V^T & U^T \end{pmatrix} \begin{pmatrix} c \\ c^\dagger \end{pmatrix} = W^+ \begin{pmatrix} c \\ c^\dagger \end{pmatrix}, \tag{4.2}$$

thereby defining the matrix W of Bogolyubov transformation as

$$W = \begin{pmatrix} U & V^* \\ V & U^* \end{pmatrix}. \tag{4.3}$$

The U and V matrices have the following form as to ensure the fermionic anti-commutation relations for the quasiparticle operators $\beta_\mu^\dagger$, β_μ, which can be summarized by the requirement on matrix W, as

$$W^+ \sigma W = \sigma, \qquad \text{where} \quad \sigma = \begin{pmatrix} 0 & I \\ I & 0 \end{pmatrix}, \tag{4.4}$$

where I is M-dimensional unit matrix. This requirement also makes possible to invert the Bogolyubov transformation

$$\begin{aligned} c_i^\dagger &= \sum_\mu U_{i\mu}^* \beta_\mu^\dagger + V_{i\mu} \beta_\mu, \\ c_i &= \sum_\mu U_{i\mu} \beta_\mu + V_{i\mu}^* \beta_\mu^\dagger, \end{aligned} \tag{4.5}$$

which also allows to express all operators in quasi-particle space.

The HFB trial wave function $|\Phi\rangle$ is defined as a vacuum with respect to the quasi-particle annihilation operators, such that $\beta_\nu|\Phi\rangle = 0$ for any ν. The HFB state that satisfies such a requirement can then trivially be constructed as

$$|\Phi\rangle = \prod_\mu \beta_\mu |0\rangle, \tag{4.6}$$

where the product runs up to maximum M-value, and the $|0\rangle$ represents the particle vacuum state. In a full analogy to the HF approach, such a HFB state $|\Phi\rangle$ is of a single Slater-determinant form, but comprised of the independent quasi-particles. It is the quasi-particle formalism that allows to take into account both short and long range correlations by virtue of breaking particle-number and other symmetries of the nuclear system that we discuss later.

4.1.2 Densities

As follows from the Bloch and Messiah theorem [226], the U and V transformation coefficients can only define the HFB wave function $|\Phi\rangle$ up to a unitary transformation of quasi-particles [59]. All the redundancy can be removed with the Wick's theorem [59, 227], that guarantees a unique definition of the HFB state in terms of the density matrix ρ and the pairing tensor κ [59, 228], whose matrix elements can be defined as

$$\rho_{kl} = \langle\Phi|c_l^\dagger c_k|\Phi\rangle = \left(V^* V^T\right)_{kl} = \rho_{lk}^*, \tag{4.7}$$

$$\kappa_{kl} = \langle\Phi|c_l c_k|\Phi\rangle = \left(V^* U^T\right)_{kl} = -\kappa_{lk}, \tag{4.8}$$

which together with the constraints on the W-matrix of Eq. (4.4) yields an additional relation between ρ and κ, so that

$$\rho^2 - \rho = -\kappa\kappa^+, \qquad \rho\kappa = \kappa\rho^*. \tag{4.9}$$

The notation can be further condensed by an introduction of a Hermitian and idempotent generalized $2M$-dimensional density matrix $\mathcal{R}$ that can be formally defined as

$$\mathcal{R} = \begin{pmatrix} \rho & \kappa \\ -\kappa^* & 1-\rho^* \end{pmatrix}, \tag{4.10}$$

whose eigenvectors correspond to the U and V coefficients of the Bogolyubov quasi-particle creation operator with eigenvalue 0, whereas the U^* and V^* correspond to annihilation operators with eigenvalue 1, which can be seen by defining the quasi-particle contraction matrix:

$$W^+ \mathcal{R} W = \begin{pmatrix} \langle\Phi|\beta_\mu^\dagger \beta_\nu|\Phi\rangle & \langle\Phi|\beta_\mu \beta_\nu|\Phi\rangle \\ \langle\Phi|\beta_\mu^\dagger \beta_\nu^\dagger|\Phi\rangle & \langle\Phi|\beta_\mu \beta_\nu^\dagger|\Phi\rangle \end{pmatrix} = \begin{pmatrix} 0 & 0 \\ 0 & I \end{pmatrix}, \tag{4.11}$$

The so-called *supermatrix* $\mathcal{R}$ contains all the degrees of freedom of HFB theory and significantly simplifies the formal derivations of the HFB equations form the variational principle, which we discuss below.

4.1.3 Variational principle and HFB equations

With all the HFB degrees of freedom encapsulated in the supermatrix $\mathcal{R}$, the energy of the system can formally be expressed with an energy functional $E[\mathcal{R}] = E[\rho, \kappa]$, which is minimized under a subsidiary condition that the HFB state $|\Phi\rangle$ remains a quasi-particle vacuum [228]. That is equivalent to the requirement that the supermatrix $\mathcal{R}$ remains idempotent, *i.e.* $\mathcal{R}^2 = \mathcal{R}$, then the actual quantity to be minimized is

$$\mathcal{E}[\mathcal{R}] = E[\mathcal{R}] - \mathrm{tr}\left[\Lambda(\mathcal{R}^2 - \mathcal{R})\right], \tag{4.12}$$

such that

$$\delta\mathcal{E} = 0, \tag{4.13}$$

and Λ is the matrix of Lagrange parameters to be determined. The variation of the energy itself can be recast in a more compact form, as

$$\delta E[\mathcal{R}] = \mathrm{tr}\left[\mathcal{H}\cdot\delta\mathcal{R}\right], \tag{4.14}$$

where the matrix of HFB Hamiltonian $\mathcal{H}$ is defined as

$$\mathcal{H} = \begin{pmatrix} h & \Delta \\ -\Delta^* & -h^* \end{pmatrix}, \tag{4.15}$$

and the supermatrix variation $\delta\mathcal{R}$ is

$$\delta\mathcal{R} = \begin{pmatrix} \delta\rho & \delta\kappa \\ -\delta\kappa^* & -\delta\rho^* \end{pmatrix}, \tag{4.16}$$

Meanwhile, the matrix elements of Hartree-Fock Hamiltonian h, and the pairing potential Δ can be expressed as

$$h_{kl} = \frac{\delta E}{\delta\rho_{lk}}, \qquad \Delta_{kl} = \frac{\delta E}{\delta\kappa^*_{kl}}$$
$$\Delta^*_{kl} = \frac{\delta E}{\delta\kappa_{kl}}, \qquad h^*_{kl} = \frac{\delta E}{\delta\rho^*_{lk}}.$$

From Eq. (4.12), together with Eq. (4.13) and aided with some simple algebra [228], the whole variation with subsidiary requirements now takes the following form

$$\mathrm{tr}\left[(\mathcal{H} - \Lambda\mathcal{R} - \mathcal{R}\Lambda - \Lambda)\delta\mathcal{R}\right] = 0, \tag{4.17}$$

and because the $\delta\mathcal{R}$ is an independent variation, it directly follows that

$$\mathcal{H} = \Lambda\mathcal{R} + \mathcal{R}\Lambda - \Lambda. \tag{4.18}$$

Whereupon multiplying with $\mathcal{R}$ from left and right, and eliminating Λ by the $\mathcal{R}^2 = \mathcal{R}$ requirement, we are left with the final compact form of the HFB equations:

$$[\mathcal{H}, \mathcal{R}] = 0. \tag{4.19}$$

4.1.4 Energy Density Functional and fields

When working with density-dependent interactions, such as Gogny or Skyrme, the energy functional $E[\mathcal{R}]$ cannot be rigorously represented as an expectation value of an effective Hamiltonian only [59], as there are also contributions to the energy functional from the density-dependence of the interaction, which result in appearance of additional rearrangement terms. However, for now we ignore these additional terms and introduce them later as a trivial correction to the derived expressions. The most general form of non-relativistic two-body Hamiltonian that does not explicitly depend on the density is

$$\hat{H} = \sum_{ij} t_{ij} \hat{c}_i^\dagger \hat{c}_j + \frac{1}{4} \sum_{ijkl} \bar{v}_{ijkl} \hat{c}_i^\dagger \hat{c}_j^\dagger \hat{c}_l \hat{c}_k, \tag{4.20}$$

where $t_{ij} = \langle i|\hat{t}|j\rangle$ are the matrix elements of kinetic energy operator, and $\bar{v}_{ijkl} = v_{ijkl} - v_{ijlk}$ are the anti-symmetrized matrix elements of two-body interaction with $v_{ijkl} = \langle i,j|\hat{V}_{\text{eff}}|k,l\rangle$. In such case, the HFB energy is an expectation value of Hamiltonian $\hat{H}$, and using Wick's theorem [59] can be expressed in terms of the density matrix ρ, and the pairing tensor Δ, as

$$E_{\text{HFB}} = \langle\Phi|\hat{H}|\Phi\rangle = \text{tr}\left[t\rho + \frac{1}{2}\Gamma\rho - \frac{1}{2}\Delta\kappa^*\right]. \tag{4.21}$$

where, in this case, the mean field Γ and the pairing field Δ are defined as

$$\Gamma_{ij} = \sum_{kl} \bar{v}_{ijkl}\rho_{lk}, \qquad \Delta_{ij} = \frac{1}{2}\sum_{kl} \bar{v}_{ijkl}\kappa_{kl}. \tag{4.22}$$

The density-dependent part of the Skyrme or Gogny effective interactions, which has the generic form of $V_{\text{DD}} \sim \delta(\vec{r}_1 - \vec{r}_2)\rho^\alpha\left(\frac{\vec{r}_1+\vec{r}_2}{2}\right)$, cannot be strictly expressed in the notation of second quantization, and the mean- and pairing-fields should be computed directly according to the Eq. (4.17). In this case, there will be additional contributions $\partial\Gamma$ to the mean-field potential in Eq. (4.22) coming from the $\partial V_{\text{DD}}/\partial\rho$ derivative [228]. Such rearrangement correction to the mean-field matrix elements is of the generic form

$$\partial\Gamma_{ij} = \sum_{klmn} \langle kl|\frac{\partial V_{DD}}{\partial\rho_{ij}}|mn\rangle\rho_{nl}\rho_{mk}. \tag{4.23}$$

Therefore, the density-dependence of the interaction can be formally accounted for by making the substitution

$$\Gamma \longrightarrow \Gamma + \partial\Gamma \tag{4.24}$$

in the derived expressions.

4.1.5 Constrained HFB states

The price one has to pay in order to maintain the simple picture of non-interacting (quasi)-particles is that the HFB state violates by its construction many of the Hamiltonian symmetries [59, 146]. On the other hand, it is precisely this symmetry breaking that effectively enlarges the variational space and, as was already mentioned previously, allows to account for many important correlations. For example, the quasi-particle vacuum $|\Phi\rangle$, constructed in Eq. (4.6), is not an eigenstate of the particle-number operator. Therefore,

solving the HFB equations, it is necessary to impose subsidiary conditions and constrain the HFB solution to yield the desired average number of protons and neutrons (projection techniques onto exact particle-number are introduced later in Sec. 4.2.2). Besides that, further constraints may be included on multipole moments in order to, for example, study the effects of various types of nuclear deformations. In principle, any operator $\hat{O}_\alpha$ may be constrained straightforwardly by augmenting the HFB matrix with the correction

$$\mathcal{H}_{ij} \longrightarrow \mathcal{H}_{ij} - \sum_\alpha \lambda_\alpha \mathcal{O}_{\alpha,ij}, \tag{4.25}$$

where λ_α are the Lagrange multipliers, and the $\mathcal{O}_{\alpha,ij}$ are the matrix elements of the corresponding operator. The minimized value is then $\langle \hat{H}' \rangle = \langle \hat{H} \rangle - \sum_\alpha \lambda_\alpha \langle \hat{O}_\alpha \rangle$. In the case of particle-number and nuclear deformation constraints, the energy functional of the constrained HFB state $|\Phi(\vec{q})\rangle$ can explicitly be written as

$$E'\left[\Phi(\vec{q})\right] = \frac{\langle \Phi(\vec{q})|\, \hat{H} - \lambda_N \hat{N} - \lambda_Z \hat{Z} - \vec{\lambda}_q \cdot \vec{\hat{Q}}\, |\Phi(\vec{q})\rangle}{\langle \Phi(\vec{q})|\Phi(\vec{q})\rangle}, \tag{4.26}$$

where the $\hat{Z}$ and $\hat{N}$ are the proton and neutron number operators, $\vec{\hat{Q}}$ are the multipole deformation operators of interest, and the corresponding Lagrange multipliers ensure that the expectation values of the constrained operators are fixed, such that

$$\langle \Phi(\vec{q})|\hat{Z}|\Phi(\vec{q})\rangle = Z, \quad \langle \Phi(\vec{q})|\hat{N}|\Phi(\vec{q})\rangle = N, \quad \text{and} \quad \langle \Phi(\vec{q})|\vec{\hat{Q}}|\Phi(\vec{q})\rangle = \vec{q}.$$

In what follows, we will, for example, extensively explore axial quadrupole nuclear deformations resulting from constrained HFB calculations, such that

$$\langle \Phi(q_{20})|\hat{Q}_{20}|\Phi(q_{20})\rangle = q_{20}, \tag{4.27}$$

where the corresponding axial quadrupole operator is $\hat{Q}_{20} = r^2 Y_{20}(\theta, \phi)$. We will also use the corresponding quadrupole deformation parameter β_2, defined as

$$\beta_2 = \sqrt{\frac{5}{4\pi}} \frac{4\pi}{3 r_0^2 A^{5/3}} \langle \hat{Q}_{20} \rangle \qquad \text{with} \quad r_0 = 1.2 \text{ fm}, \tag{4.28}$$

as the collective coordinate in the beyond-mean-field calculations, as described in Sec. 4.2.4.

4.1.6 Solution of HFB equations with the gradient method

As we have seen, the HFB theory leads to a system of non-linear equations that are typically solved by iterative diagonalizations [59]. This proceduce is often computationally very demanding, and convergence is not always guaranteed. Since the variational principle is the foundation of the HFB theory, solving the HFB equations is equivalent to searching for a local minimum on a multidimensional energy surface. To this end, the gradient method [146, 229] is found to be very efficient in searching for the HFB energy minimum with multiple subsidiary constraints. The gradient method starts with an arbitrary initial wave function $|\Phi_0\rangle$ and each step in the iterative process is ensured to be taken in the direction of the steepest descent of the energy, while additionally keeping the path orthogonal to the gradient of the constraining conditions until the

energy minimum is reached. The gradient method can be conveniently formulated using the Thouless theorem [230], which also provides an alternative derivation of the HFB equations [59, 228]. The theorem states, that any HFB wave function $|\Phi\rangle$ that is *not* orthogonal to $|\Phi_0\rangle$ can be represented in terms of the Thouless matrix Z as

$$|\Phi(Z)\rangle = \langle\Phi_0|\Phi(Z)\rangle \exp\left[\frac{1}{2}\sum_{\mu\nu} Z_{\mu\nu}\beta^\dagger_\mu\beta^\dagger_\nu|\Phi_0\rangle\right]. \tag{4.29}$$

This provides also a unique parametrization of the energy surface near the initial starting point $|\Phi_0\rangle \equiv |\Phi(Z_0)\rangle$ given by the Bogolyubov transformation W_0. Taking a step in the direction of the steepest energy descent while keeping the imposed requirements on constraints will yield a new set of Bogolyubov coefficients W_1, corresponding to another Thouless matrix Z_1, as

$$Z_1 = -\eta\left(H^{20} - \sum_\alpha \lambda_\alpha O^{20}_\alpha\right), \tag{4.30}$$

where η is a small step size of iteration such that δE is negative, the parameters λ_α define the small admixtures to the energy gradient as to ensure the required expectation values of the constrained operators, *e.g.* $\hat{O} = \{\hat{N}, \hat{Z}, \hat{Q}_i\}$, with the corresponding matrix elements having the general form

$$O^{20}_{\alpha,ij} = \langle\Phi_0|\left[\beta_j\beta_i, \hat{O}_\alpha\right]|\Phi_0\rangle, \tag{4.31}$$

while in particular H^{20} matrix can be expressed as

$$H^{20} = U^+hV^* - V^+h^TU^* + U^+\Delta U^* - V^+\Delta^*V^*, \tag{4.32}$$

and the H^{11} is of the form

$$H^{11} = U^+hU - V^+h^TV + U^+\Delta V - V^+\Delta^*U, \tag{4.33}$$

where the HF Hamiltonian h for a density-dependent interaction is of the form $h = t + \Gamma + \partial\Gamma$. The new set of quasi-particle operators, defining the HFB state $|\Phi_1\rangle$, has to be orthogonalized at the each step of iteration in order to satisfy the fermionic anti-commutations by diagonalizing the H^{11} matrix. The convergence is reached when

$$\delta E'[\Phi(\vec{q})]_{\Phi(\vec{q})=\Phi_{\mathrm{HFB}}} = 0, \tag{4.34}$$

which is equivalent to

$$\left(\frac{\partial E'[Z]}{\partial Z}\right)_{Z=0}\delta Z = 0. \tag{4.35}$$

That is also equivalent to the requirement

$$H'^{20} = H^{20} - \sum_\alpha \lambda_\alpha O^{20}_\alpha = 0. \tag{4.36}$$

The effect from solving the HFB equations can also be understood if we re-write the initial Hamiltonian from Eq. (4.20) using the inverse Bogolyubov transformation of Eq. (4.5) to obtain its representation in quasi-particle space

$$\hat{H}' = H'^0 + \sum_{\mu\nu} H'^{11}_{\mu\nu}\beta^\dagger_\mu\beta_\nu + \frac{1}{2}\sum_{\mu\nu}\left(H'^{20}_{\mu\nu}\beta^\dagger_\mu\beta^\dagger_\nu + \mathrm{h.c.}\right) + H'^{40} + H'^{31} + H'^{22}. \tag{4.37}$$

Now, with the condition of the HFB solution on ${H'}^{20}$ in Eq. (4.36) and diagonalization requirement for ${H'}^{11}$, the Hamiltonian takes the form

$$H' = E_{\mathrm{HFB}} + \sum_{\mu} E_{\mu}\beta^{\dagger}_{\mu}\beta_{\mu} + H_{\mathrm{res}}, \tag{4.38}$$

where terms ${H'}^{40}$, ${H'}^{31}$, and ${H'}^{22}$ – all containing four-quasi-particle products that enter the residual part H_{res}, are minimized by HFB solution and neglected in the quasi-particle non-interacting picture of HFB theory; the E_{μ} are the quasi-particle energies, which can be established from an alternative form of the HFB equations

$$\begin{pmatrix} h' & \Delta \\ -\Delta^{*} & -h'^{*} \end{pmatrix} \begin{pmatrix} U_{\mu} \\ V_{\mu} \end{pmatrix} = \begin{pmatrix} U_{\mu} \\ V_{\mu} \end{pmatrix} \cdot E_{\mu}. \tag{4.39}$$

Here, in the case of density-dependent effective interaction, the mean-field Hamiltonian with all the induced constraints is defined as

$$h' = t + \Gamma + \partial\Gamma - \sum_{\alpha} \lambda_{\alpha} \tag{4.40}$$

and the separate U_{μ} and V_{μ} columns of the Bogolyubov transformation matrices define the corresponding $\beta^{\dagger}_{\mu}$ operators. The fact that both $\mathcal{H}$ and $\mathcal{R}$ matrices are diagonal in β_{μ} operator basis is equivalent to the compact form of HFB equations in Eq. (4.19) derived previously. Solving these equations with various diagonalization techniques, or the gradient method described above, results in establishing the quasi-particle vacuum $|\Phi_{\mathrm{HFB}}\rangle$ state that minimizes the HFB energy $E[\mathcal{R}]$ under the imposed constraints. In what follows, for the sake of simplicity we are going to write the energy as an expectation value of the Hamiltonian (and not in its more general energy functional form), which in case of the found ground-state HFB energy is

$$E_{\mathrm{HFB}} = \frac{\langle \Phi_{\mathrm{HFB}} | \, \hat{H}' \, | \Phi_{\mathrm{HFB}} \rangle}{\langle \Phi_{\mathrm{HFB}} \mid \Phi_{\mathrm{HFB}} \rangle}. \tag{4.41}$$

4.2 Beyond-Mean-Field methods

The static mean-field approach of the HFB theory described above is proven to be very successful in describing the bulk nuclear properties (such as nuclear binding energies, radii, and deformations) throughout the whole nuclear chart. However, since the Bogolyubov transformation in Eq. (4.1) by its construction mixes the particle creation and annihilation operators, the resulting HFB state (Eq. (4.6)) is no longer an eigenstate of the proton and neutron number operators. Moreover, if there are no additional restrictions on the Bogolyubov matrices U and V, such symmetries of the system as parity and angular momentum will also be inevitably broken. Despite these substantial complications, it is precisely the construction of such *most general* product wave function that permits self-consistently to take into account some of the essential nuclear effects, such as pairing. Nevertheless, not all of the important correlations could be effectively subsumed by density-dependent effective interaction and the HFB picture of non-interacting quasi-particles. The clear presence of significant residual correlations is observed, for example, by the strongly imprinted *shell effects* in Fig. 5.3, which

cannot be accounted for with the smoothly varying energy functional [219]. In order to improve the theoretical predictions and include the missing correlations one has to go beyond the static mean-field approach. This can be achieved withing several different frameworks. For example, the Shell Model inspired multiparticle-multihole (MPMH) configuration interaction approaches [138, 231, 232] allows treatment of long-range correlations beyond the mean-field formalism, while keeping the symmetries of the Hamiltonian preserved. Other examples include different variations of the Random Phase Approximation (RPA) [233–236], that incorporates small amplitude collective vibrations of the nucleus as coherent superpositions of individual excitations. The beyond-mean-field (BMF) methods used in this work are all based on the Generator Coordinate Method (GCM) approach that provides all the necessary tools to build a linear superposition of several mean-field states to, for example, restore the symmetries of the Hamiltonian that were broken by the HFB method, or include correlations induced by large amplitude collective motion. In this chapter we first briefly present the general formalism of the GCM method, and then show how it can be utilized to conveniently restore such elementary symmetries of Hamiltonian as particle number and angular momentum, as well as to perform symmetry-conserving configuration mixing (SCCM) calculations. For more details, we refer to Refs. [59, 146, 219, 237].

4.2.1 Generator Coordinate Method

The general idea of the Generator Coordinate Method (GCM) is to expand an unknown many-body wave function in terms of a linear superposition of the known set of generating $|\Phi(\tau)\rangle$ wave functions [59, 237], which are labeled according to one or several collective variables $\tau = \{\tau_1, \tau_2, ...\}$, such that

$$|\Psi_k\rangle = \int d\tau f_k(\tau)|\Phi(\tau)\rangle. \tag{4.42}$$

where k is the eigenstate index of the Hamiltonian, $f_k(\tau)$ is the weight function, and the integral is taken over the space of the generator coordinates τ. The mixing coefficients $f_k(\tau)$ are generally established by variational principle, requiring that the energy expectation value

$$E\left[\Psi\right] = \frac{\langle\Psi|\hat{H}|\Psi\rangle}{\langle\Psi|\Psi\rangle}. \tag{4.43}$$

is stationary to any arbitrary variation δf_k. This requirement leeds to the generalized eigenvalue problem, known as the Hill-Wheeler-Griffin (HWG) equation [238, 239], which can be stated as

$$\int d\tau' \left[\mathcal{H}(\tau,\tau') - E_k\mathcal{N}(\tau,\tau')\right] f_k(\tau) = 0, \tag{4.44}$$

where the Hamiltonian and the norm overlaps, $\mathcal{H}$ and $\mathcal{N}$, are defined as

$$\begin{aligned} \mathcal{H}(\tau,\tau') &= \langle\Phi(\tau)|\,\hat{H}\,|\Phi(\tau')\rangle, \\ \mathcal{N}(\tau,\tau') &= \langle\Phi(\tau)\,|\,\Phi(\tau')\rangle. \end{aligned} \tag{4.45}$$

Since practical calculations call for numerical solution of HWG equation by discretization, the equation can be further condensed by recasting it into the matrix form

$$\mathcal{H}f = E\mathcal{N}f. \tag{4.46}$$

Then formally inverting the overlap norm $\mathcal{N}$, and then diagonilizing the $\mathcal{N}^{-1}\mathcal{H}$ would yield a non-Hermitian eigenvalue problem. However, since this is not always possible, one way to proceed is to orthogonilize the collective $|\Phi(\tau)\rangle$ basis set. One starts with the diagonalization of the norm operator $\mathcal{N}$ by

$$\int d\tau' \mathcal{N}(\tau,\tau') u_\xi(\tau') = n_\xi u_\xi(\tau), \tag{4.47}$$

where the $u_\xi(\tau)$ now comprise a complete set of orthonormalized functions in the Hilbert space of the weight functions. If $n_\xi \neq 0$, we can now define a set of *orthonormal* states $|\xi\rangle$ that span the original space of the generating functions $|\Phi(\tau)\rangle$

$$|\xi\rangle = \frac{1}{\sqrt{n_\xi}} \int d\tau u_\xi(\tau) |\Phi(\tau)\rangle. \tag{4.48}$$

Now the original GCM state (Eq. (4.42)) can be re-written in terms of these *natural states* $|\xi\rangle$, as

$$|\Psi_k\rangle = \sum_{\xi, n_\xi \neq 0} g_\xi^k |\xi\rangle \tag{4.49}$$

where the g_ξ coefficients, following from Eq. (4.48), are connected to the original weight functions, as

$$f_k(\tau) = \sum_{\xi, n_\xi \neq 0} \frac{g_\xi^k}{\sqrt{n_\xi}} u_\xi(\tau), \tag{4.50}$$

The HWG equation (Eq. (4.46)) can now formally be formulated as

$$\tilde{\mathcal{H}} g = E g, \tag{4.51}$$

or, more precisely, we get a diagonalization problem in the natural basis that defines both g_ξ^k and E_k as

$$\sum_\xi \langle \xi | \hat{H} | \xi' \rangle g_{\xi'}^k = E_k g_\xi^k. \tag{4.52}$$

The same procedures can be applied *not* only to the Hamiltonian, but to any operator of interest to obtain its expectation values in the GCM formalism. It should also be noted that, since the $f_k(\tau)$ are not orthogonal, they cannot be strictly regarded as probability, but we can introduce a so-called collective wave function $G_k(\tau)$ as

$$G_k(\tau) = \sum_\xi g_{\xi'}^k u_\xi(\tau), \tag{4.53}$$

that, if normalized to unity, *i.e.* $\int d\tau |G_k(\tau)|^2 = 1$, can be iterpreted as the corresponding probability amplitude [219].

The choice of the generating functions $|\Phi(\tau)\rangle$ and corresponding coordinates τ may be arbitrary and, theoretically, the GCM ansatz could provide an exact solution to the nuclear many-body problem. In practice, the choice of the generating functions is dictated by the particular physical problem, and the number of generating coordinates, as well as usual necessity of their discretization comes from the computational time restrictions. In our case, the generating functions $|\Phi(\tau)\rangle$ are the quasi-particle HFB–states, while the collective variables of our choice are either associated with the restoration of

a broken symmetry, or are used to generate a shape-mixed state. In the first case, the set of the $|\Phi(\tau)\rangle$ functions is generated by symmetry operators, such as rotations in the gauge space for particle-number restoration, or the rotations in the coordinate space for the angular momentum projections. The weight functions $f(\tau)$ for these cases can be established directly from the properties of the symmetry operators. For the case of the shape mixing, the collective space is generated from the constrained HFB calculations with one or several multipole moments being the corresponding collective variables. In our study we use the quadrupole moments as the only degree of freedom in our configuration-mixing calculations.

4.2.2 Particle-number projection

As was already mentioned before, one of the major problems in the HFB approach is violation of many Hamiltonian symmetries by the mean-field approximations. For example, the HFB quasi-particle vacuum by construction is not an eigenstate of the proton and neutron number operators $\hat{Z}$ and $\hat{N}$. Restoring these symmetries by projecting them onto good particle number states and then applying the variational method to the projected state will generally enlarge the variational space and will yield, as we show in Chap. 6, significant additional correlation energy. Since projecting techniques are the special cases of the GCM method described in the previous chapter, the main idea remains the same – to diagonalize the Hamiltonian in the collective subspace of generating functions $|\Phi(\phi)\rangle$. The collective coordinate ϕ in this case is an orientation angle in the quasi-spin gauge space associated with the particle (neutron) number operator $\hat{N}$ [59]. Then, following the general GCM ansatz of Eq. (4.42), we have

$$|\Psi\rangle = \int d\phi f(\phi)|\Phi(\phi)\rangle. \tag{4.54}$$

where $|\Psi\rangle$ is unknown GCM wave function with the corresponding weight functions $f(\phi)$. The form of the weight functions $f(\phi)$ is established by the particular symmetry in question, which in case of the neutron-number operator is of the form [219]:

$$f(\phi) = \sum_N \frac{1}{2\pi} e^{-iN\phi} \cdot g_N, \tag{4.55}$$

where N is an integer, and the general GCM function obtains a more specific form

$$|\Psi\rangle = \sum_N g_N \hat{P}^N |\Phi\rangle. \tag{4.56}$$

Here, the projection operator itself is of the form

$$\hat{P}^N = \frac{1}{2\pi} \int_0^{2\pi} d\phi e^{i\phi(\hat{N}-N)}, \tag{4.57}$$

which has the usual projector properties, as $(\hat{P}^N)^2 = \hat{P}^N$, and $(\hat{P}^N)^\dagger = \hat{P}^N$. Since out of the whole space of generic GCM functions of form given in Eq. (4.56) we are interested in only one state with a proper neutron number $|\Psi^{N_0}\rangle$, we require that $g_N = 0$ for all $N \neq N_0$, which leaves us only with the normalization constant g_{N_0}. At the end, taking the normalization constant $g_{N_0} = 1$, the initial GCM ansatz of Eq. (4.54) is reduced to

$$|\Psi^{N_0}\rangle \equiv \hat{P}^{N_0}|\Phi\rangle = \frac{1}{2\pi} \int_0^{2\pi} d\phi e^{i\phi(\hat{N}-N_0)}|\Phi\rangle. \tag{4.58}$$

By analogy, we define the wave function that is projected *both* onto good neutron *and* proton number as

$$|\Psi^{N_0 Z_0}\rangle \equiv \hat{P}^{N_0}\hat{P}^{Z_0}|\Phi\rangle, \tag{4.59}$$

where $\hat{P}^Z$ is the corresponding proton-number projection operator in full analogy to the case of neutrons.

The variation is then performed by minimizing the particle-number projected expectation energy within the set of generating HFB-states

$$\delta\frac{\langle\Phi|\hat{H}'\hat{P}^{N_0}\hat{P}^{Z_0}|\Phi\rangle}{\langle\Phi|\hat{P}^{N_0}\hat{P}^{Z_0}|\Phi\rangle} = \delta\frac{\langle\Psi^{N_0 Z_0}|\hat{H}'|\Psi^{N_0 Z_0}\rangle}{\langle\Psi^{N_0 Z_0}|\Psi^{N_0 Z_0}\rangle} = 0. \tag{4.60}$$

This technique is known as the particle-number variation after projection (PN-VAP) [146], which in its essence is nothing else than the GCM approach with double energy variation: against the weight function $f(\tau)$, as well as the generating states $|\Phi\rangle$. However, in this case the former is established by the particular symmetry in question, with only the latter to be varied. The effect of PN-VAP is that by projecting the HFB state onto an eigenstate of the particle-number operator, we actually expand the variational space, as is evident from Eq. (4.57), where we sum (integrate) over various HFB–states. This, in turn, has an effect of gaining additional binding energy owing to the underlying variational principle.

4.2.3 Angular momentum projection

Not only the particle-number symmetry is broken in the mean-field approach, the HFB wave functions generally do not respect the angular momentum symmetry. Consequentially, the deformed HFB ground states are not eigenstates of the total angular momentum operator $\hat{J}^2$ and its projection on the z–axis $\hat{J}_z$, which have the eigenvalues $\hbar^2 J(J+1)$ and $\hbar M$, respectively. And one has to reach beyond the mean-field formalism again in order to restore the rotational symmetries of the wave function. By full analogy with the particle-number restoration, the angular-momentum projection (AMP) technique starts with a set of generating functions $|\Phi(\Omega)\rangle$. These functions are then rotated in the coordinate space to build a suitable linear combination in the spirit of GCM method to recover a proper angular momentum state [59, 146].

We start directly with writing down the angular momentum projector operator [219, 240] as

$$\begin{aligned}\hat{P}^J_{MK} &= \frac{2J+1}{16\pi^2}\int_0^{4\pi} d\alpha \int_0^{\pi} d\beta \sin(\beta) \int_0^{2\pi} d\gamma \mathcal{D}^{J*}_{MK}(\Omega)\hat{R}(\Omega) \\ &= \frac{2J+1}{8\pi^2}\int d\Omega \mathcal{D}^{J*}_{MK}(\Omega)\hat{R}(\Omega),\end{aligned} \tag{4.61}$$

where $\Omega = (\alpha, \beta, \gamma)$ are the Euler angles, the $\mathcal{D}^{J*}_{MK}(\Omega)$ is the Wigner function [241], which can be further decomposed in terms of the *reduced* Wigner's function $d^J_{MK}(\beta)$ to

$$\mathcal{D}^J_{MK}(\Omega) = e^{-iM\alpha}\cdot d^J_{MK}(\beta)\cdot e^{-iK\gamma}. \tag{4.62}$$

The $\hat{R}(\Omega)$ is the rotation operator [242] and has the form

$$\hat{R}(\Omega) = e^{-i\alpha\hat{J}_x}e^{-i\beta\hat{J}_y}e^{-i\gamma\hat{J}_z}. \tag{4.63}$$

Then the weight functions of the GCM state can be expanded in the set of angular momenta operators represented in Euler angles, thus taking the form

$$f(\Omega) = \frac{2J+1}{8\pi^2} \sum_{JMK} g_{JMK} \mathcal{D}^{J*}_{MK}, \tag{4.64}$$

so that the general GCM state is

$$|\Psi\rangle = \sum_{JMK} g_{JMK} \hat{P}^J_{MK} |\Phi\rangle. \tag{4.65}$$

The effect of the operator $\hat{P}^J_{MK}$ is to select the components of $|\Phi\rangle$ that have the JMK quantum numbers, but it is not strictly a projector. Nevertheless, it possesses the following important properties [243]:

$$(\hat{P}^J_{MK})^\dagger = \hat{P}^J_{KM} \qquad \text{and} \qquad \hat{P}^J_{KM} \hat{P}^{J'}_{M'K'} = \delta_{JJ'} \delta_{MM'} \hat{P}^J_{KK'} \tag{4.66}$$

Projected state that bears the required J_0 and M_0 quantum numbers $|\Psi_{J_0 M_0}\rangle$ is constructed by summing over all $(2J_0+1)$ angular momentum projections along the intrinsic z–axis, *i.e.*

$$|\Psi^\sigma_{J_0 M_0}\rangle = \sum_{K=-J_0}^{+J_0} g^\sigma_{J_0 M_0 K} \hat{P}^{J_0}_{M_0 K} |\Phi\rangle. \tag{4.67}$$

Here, σ is the ordinal index for particular value of J_0, which arise from solving the HWG equations with $\sigma = 1$ corresponding to the ground state. In the general case, one proceeds then with minimization of the energy of the projected state to find both the generating states $|\Phi\rangle$ and the coefficients $g^\sigma_{J_0 M_0 K}$, which is equivalent to a diagonalization of the initial Hamiltonian $\hat{H}$ in the space spanned by the non-orthogonal projected states $\hat{P}^J_{MK}|\Phi\rangle$.

However, if we are restricted only to axially-symmetric deformations, the mean-field HFB solution is already represented by the $J_z = 0$ angular-momentum state, so that $\hat{J}_z|\Phi\rangle = 0$ and, naturally, are invariant to any rotations around the symmetry axis, *i.e.* $e^{-i\alpha \hat{J}_z}|\Phi\rangle = |\Phi\rangle$. Of course, a deformed solution $|\Phi(\beta_2)\rangle$ is still not an eigenstate of the total angular momentum operator $\hat{J}^2$, and, in principle, should be projected onto one of its eigenstates. In the case of the axial symmetry, the computationally demanding calculation of the 3-dimentional integral across all Euler angles in Eq. (4.61) is reduced to one-dimensional numerical integration

$$\hat{P}^J_{00} = \frac{2J+1}{2} \int_0^\pi d\beta d^{J*}_{00}(\beta) e^{-i\beta \hat{J}_y}, \tag{4.68}$$

which substantially simplifies the problem. Additinally, in the case of T-symmetric HFB states with simplex symmetry, the range of integration for β Euler angle may be even reduced [244] to $[0, \pi/2]$ interval. Moreover, in the sum of Eq. (4.67) only $M = K = 0$ term is left, which basically already defines the $g^\sigma_{J_0 00}$ coefficient by the normalization requirement [59].

In the practical application, the angular projection is usually carried out together with the particle-number restoration, which together with Eq. (4.60) leads to the energy variation requirement for the projected states

$$\delta \frac{\langle \Psi^{N_0 Z_0} | \hat{H}' \hat{P}^{J_0}_{00} | \Psi^{N_0 Z_0} \rangle}{\langle \Psi^{N_0 Z_0} | \hat{P}^{J_0}_{00} | \Psi^{N_0 Z_0} \rangle} = \delta \frac{\langle \Psi^{N_0 Z_0}_{J_0 \sigma} | \hat{H}' | \Psi^{N_0 Z_0}_{J_0 \sigma} \rangle}{\langle \Psi^{N_0 Z_0}_{J_0 \sigma} | \Psi^{N_0 Z_0}_{J_0 \sigma} \rangle} = 0. \tag{4.69}$$

This method includes both symmetry-restorations and is known as Particle-Number and Angular-Momentum Projection (PNAMP), which we later use together with the shape-mixing calculation, usually denoted as the symmetry-conserving configuration-mixing (SCCM) method.

4.2.4 Configuration Mixing

Having applied the particle-number and angular-momentum projecting techniques we have restored the corresponding symmetries. However, the obtained $|\Psi^{N_0Z_0}_{J_0}\rangle$–state still possesses some properties, such as quadrupole moment, very similar to the initial mean-field solution $|\Phi\rangle$. In order to properly describe the correlated ground and excited states, and study such nuclear phenomena as shape vibrations, coexistence, or transitions, one can revert to the configuration-mixing technique [245, 246]. The choice of the generating coordinate for the shape mixing is dictated by the corresponding operators to which the energy of such correlations is particularly sensitive to. Since we are dealing only with axially symmetric states, the subset of generating wave functions $|\Psi^{N_0Z_0}_{J_0}(\beta_2)\rangle$ that are going to be mixed is constructed by PNAMP calculations with constrained axial quadrupole moment operator $\hat{O}_{20}$. Hence, we can choose the β_2 deformation parameter, defined in Eq. (4.28), as the corresponding collective variable. Consequentially, the constructed GCM state $|\tilde{\Psi}^{NZ}_{J\sigma}\rangle$ within the symmetry-conserving configuration-mixing (SCCM) framework is a linear superposition of the constrained PNAMP wave functions (for simplicity we drop the 0 subscript, so that $J = J_0$, and so on) as

$$\begin{aligned} |\tilde{\Psi}^{NZ}_{J\sigma}\rangle &= \sum_{\beta_2} g^{J\sigma}_{\beta_2} |\Psi^{NZ}_{J\sigma}(\beta_2)\rangle \\ &= \sum_{\beta_2} g^{J\sigma}_{\beta_2} \hat{P}^J_{00} \hat{P}^Z \hat{P}^N |\Phi(\beta_2)\rangle. \end{aligned} \tag{4.70}$$

Then the mixing coefficients $g^{J\sigma}_{\beta_2}$ are found, by analogy with the previous cases, with the Ritz variational principle

$$\delta E^{J\sigma}_{\mathrm{SCCM}} \left[g^{J\sigma}_{\beta_2} \right] = 0, \tag{4.71}$$

leading once again to the HWG equations, that define the energy levels $E^{J\sigma}_{\mathrm{SCCM}}$ for different angular momentum values:

$$\sum_{\beta_2'} \left(\mathcal{H}^J_{\beta_2,\beta_2'} - E^{J\sigma}_{\mathrm{SCCM}} \mathcal{N}^J_{\beta_2,\beta_2'} \right) g^{J\sigma}_{\beta_2'} = 0, \tag{4.72}$$

where the Hamiltonian and the norm overlaps of Eq. (4.45) take the form

$$\begin{aligned} \mathcal{H}^J_{\beta_2,\beta_2'} &= \langle \Phi(\beta_2) | \hat{H}' \hat{P}^J_{00} \hat{P}^N \hat{P}^Z | \Phi(\beta_2') \rangle \\ \mathcal{N}^J_{\beta_2,\beta_2'} &= \langle \Phi(\beta_2) | \hat{P}^J_{00} \hat{P}^N \hat{P}^Z | \Phi(\beta_2') \rangle. \end{aligned} \tag{4.73}$$

The J index of the weight functions $g^{J\sigma}_{\beta_2}$ indicates that the HWG equations must be diagonilized anew for different values of angular momentum according to the GCM framework described previously in Sec. 4.2.1.

5 Convergence analysis in truncated oscillator spaces and extrapolations therefrom

In this chapter we study the convergence properties of nuclear binding energies and two-neutron separation energies obtained with self-consistent mean-field calculations based on the Hartree-Fock-Bogolyubov (HFB) method with Gogny-type effective interactions. Owing to lack of convergence in a truncated working basis, we employ and benchmark one of the recently proposed infrared energy-correction techniques to extrapolate our results to the limit of an infinite model space. We also discuss its applicability to global calculations of nuclear masses. The preliminary study of the convergence properties in SHO bases was performed in Ref. [247]. Thereupon some additional results were reported in Ref. [248]. This chapter is focusing on a newer extrapolation technique designed specifically for calculations of atomic nuclei with much improved analysis of convergence properties and particular focus on astrophysical applications. The results of this chapter were originally published in Ref. [249].

5.1 Introduction

Most of the current EDF calculations utilize for the many-body wave function expansion either a mesh with a given size of the box and a distance between neighbor points, or a finite number of harmonic oscillator single-particle states. Observables, like binding energies, radii, *etc.*, should in principle be independent of a particular choice for the working basis. Nonetheless, such an independence is only obtained in calculations in a mesh if a sufficiently large and dense box is used. On the other hand, a large number of single-particle states have to be included in the calculation with harmonic oscillator bases. This is rarely the case in practical applications due to limited computational resources. Hence, increasing the size of the working basis usually leads to an emergence of convergence patterns for the calculated observables. In the case of calculations in a mesh, such convergence studies have been systematically performed recently with Skyrme functionals (see Ref. [250] and references therein). For harmonic oscillator bases, extrapolations schemes to the limit of an infinite basis have been used [21, 154, 190, 251–255], as well as modifications of the basis in the so-called transformed harmonic oscillator method [256].

One of the goals of this chapter is to analyze the convergence of energies computed with an underlying harmonic oscillator single-particle basis using the variational HFB method. By doing this, we can directly test the global validity of the central ansatz for a widely implemented phenomenological extrapolation prescription in some of the previous large-scale HFB-based calculations [154, 251, 257]. To our best knowledge, none

of the earlier publications addressed the accuracy of this approach across entire isotopic chains. Having performed the convergence analysis, we turn our attention to a more recent extrapolation method, that was theoretically derived for calculations performed in harmonic oscillator basis [252–255]. However, previous studies have evaluated the performance of this extrapolation strategy on a couple of simple systems for which "exact" many-body calculations are possible. In what follows we introduce necessary tools and establish appropriate criteria for the systematic analysis of this extrapolation strategy applied to HFB calculations using Gogny EDF.

After a brief recapitulation of the general properties of the harmonic oscillator working basis in Sec. 5.2, we analyze the convergence patterns of HFB calculations with the variation of the numerical parameters of the basis in Sec. 5.4. Then, in Sec. 5.5.1-5.5.2, we describe the most important aspects of an extrapolation scheme introduced by Furnstahl, Hagen and Papenbrock in Ref. [252] and improved subsequently in Refs. [253–255]. In Sec. 5.5.3 this method is applied to the nucleus ^{16}O as a benchmark. This analysis is generalized to the nucleus ^{120}Cd in Sec. 5.5.4, and the cadmium isotopic chain in Sec. 5.5.5, where we identify the potential problems that could appear in the extrapolation. Finally, the main results are summarized in Sec. 5.6.

5.2 Numerical parameters of SHO basis

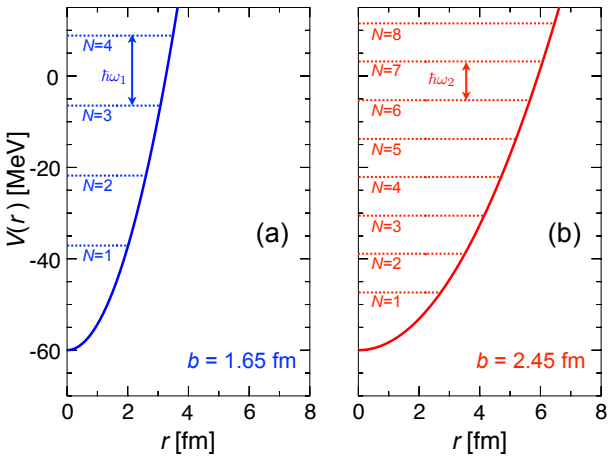

Fig. 5.1: SHO levels for two different values of the oscillator length (a) $b = 1.65$ fm and (b) $b = 2.45$ fm. From Ref. [249].

A common choice of the single-particle working basis for the quasi-particle expansion (Eq. 4.1) is a set of spherical harmonic oscillator (SHO) functions. In this case there are two numerical parameters that define the basis itself. The first one is the total number of major oscillator shells included in the basis N_{OS}, which defines its dimension d_{tot}. Hence, the total number of single-particle states in the basis is

$$\begin{aligned} d_{\text{tot}} &= \sum_{N=1}^{N_{OS}} D(N) \\ &= \frac{1}{3} N_{OS}(N_{OS}+1)(N_{OS}+2), \end{aligned} \tag{5.1}$$

where $D(N) = N(N+1)$ is the degeneracy of a single oscillator shell. Here, $N = 1, 2, \ldots$ is the major oscillator number $N = 2n + l + 1$, with $n = 0, 1, 2, \ldots$ and l being the radial and angular momentum quantum numbers, respectively.

The second parameter of the basis is the intrinsic oscillator length b of the SHO functions, which is connected to the oscillator energy $\hbar\omega$ as

$$b = \sqrt{\frac{\hbar}{m\omega}}. \tag{5.2}$$

In Fig. 5.1 we represent schematically the well-known spherical harmonic oscillator potential, $V(r) = -V_0 + (r/b)^2\hbar\omega/2$, for two different values of the oscillator length $b =$ 1.65 fm and 2.45 fm. The depth of the well is chosen to be the same for both schematic potentials, $V_0 = 60$ MeV. It is thus clear that for a fixed number of N_{OS}, the maximum energy reached by a single-particle state will be larger when the intrinsic oscillator length b (and therefore the effective radius of the basis) is smaller. Nevertheless, both bases are equivalent and should yield identical results for calculated observables when an infinite value of N_{OS} is considered. However, due to basis truncations in practical calculations and an improper asymptotic behavior of the harmonic oscillator wave functions at long distances, such an independence from the numerical basis parameters $\{N_{OS}, b\}$ is rarely reached.

5.3 Large-scale HFB calculation

A global drip-to-drip line calculation of nuclear masses with finite–range Gogny D1S interaction is computationally an intensive and challenging task. In spite of narrowing down the scope of this study to the set of even-even isotopes, the full list of $8 \leq Z \leq 134$ nuclei includes 2180 entries. Allowing only axial deformations, up to 100 independent calculations had to be carried out for every nucleus in order to ensure a bettermost convergence of the final ground-state energy. In this survey the binding energies were calculated in $N_{OS} = 19$ basis using an adaptive oscillator length parameter b, while also having the quadrupole deformation parameter β_2 as an additional degree of freedom. The results are presented in Fig. 5.2 (a), where the difference between the experimental binding energies of AME12 [13, 14] and our results are plotted as a function of the mass number A. For comparison, Fig. 5.2 (b) shows a similar plot, but for the computed masses listed in previously published AMEDEE database [199, 251, 258]. Some profound patterns are clearly noticeable for both serveys. For example, the peaks associated with the neutron magic numbers are well established at $A \approx 100, 150, 220$. It is precisely where the theoretical calculation are overbound in comparison to the empirical results, while the regions in-between the neutron shell closures are somewhat underbound. Another trend is that the neutron-rich isotopes of the heavier isotopic chains are systematically underbound by as much as $\sim 5 - 10$ MeV, which is evident by the tails of isotopic chains greatly bending down. The newer Gogny parametrizations, such as D1N [191] or D1M [154], do not posses such a drawback, because the neutron matter equation of state was properly taken into account during the fitting procedure. Comparing this survey to one of the already published databases, one sees that, due to a better convergence treatment, we have managed to achieve an overall better convergence by ~ 1.5 MeV, which is evident by a global shift of our calculation upwards, *cf.* Fig. 5.2 (a) and Fig. 5.2 (b). Besides that, a particular improvement of calculations in comparison to experimental results is seen in-between the neutron magic numbers, around $A \sim 130$ and $A \sim 180$. This can be well seen in Fig. 5.2 (c) by reduction of the so-called *Shell Effects* in cadmium isotopic chain. The Shell Effects (S.E.) is a scaling tool that subtracts the smooth part of the binding energy predicted by the liquid-drop model (LDM) from the total binding energy of particular method (HFB is our case):

$$S.E.(Z,N) = E_{\mathrm{LDM}}(Z,N) - E_{\mathrm{HFB}}(Z,N). \tag{5.3}$$

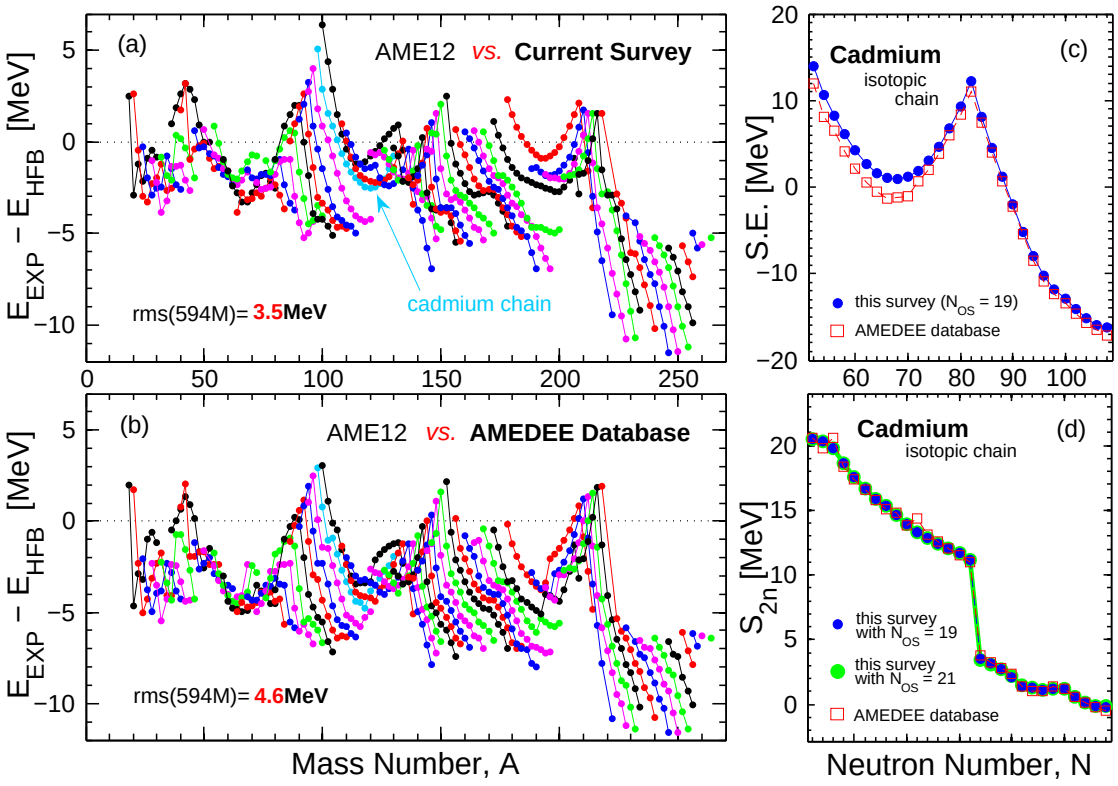

Fig. 5.2: Energy differences between AME12 compilation and theoretical masses according to calculations performed: (a) in this work, and (b) published results in Ref. [258]; (c) comparison of *Shell Effects* (Eq. (5.3)), and (d) two-neutron separation energies of cadmium isotopic chain. From Ref. [248].

A better convergence treatment generally results in much smoother mass curves in Fig. 5.2 (a), than the AMEDEE results reported in Ref. [258]. The direct consequence of this fact is that the extracted two-neutron separation energies are also smoother and lack much of the numerical noise found in AMEDEE database. The improvement is shown by the example of cadmium chain in Fig. 5.2 (d), where the extracted S_{2n} values from both surveys are compared. We can also notice that, despite the lack of full convergence in masses, the extracted two-neutron separations energies appear to be converged converged, which can be seen from the overlap of S_{2n} values calculated in $N_{OS} = 19$ and $N_{OS} = 21$ bases, Fig. 5.2 (d). Later we come back to this topic and systematically analyze the convergence patterns of binding and neutron-separation energies. Finally, the rms value between the 594 doubly even nuclei listed in the experimental AME12 compilation and the theoretical HFB-D1S calculations was also improved from ∼4.6 MeV for AMEDEE survey to ∼3.5 MeV in case of our results.

5.4 Convergence properties

Fig. 5.3 shows the calculated ground-state (g.s.) HFB energies of ^{16}O and ^{120}Cd for SHO basis dimensions $N_{OS} = 11, ..., 21$ plotted against various oscillator length values b. One sees that going from $N_{OS} = 11$ to $N_{OS} = 13$, or from $N_{OS} = 13$ to $N_{OS} = 15$ yields noticeably deeper minima. Yet given a sufficiently large basis, the g.s. energies

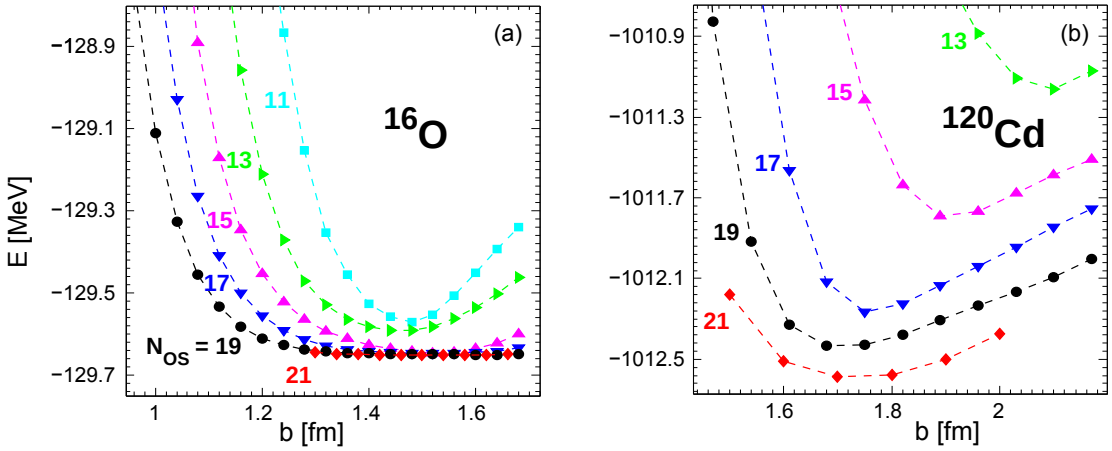

Fig. 5.3: HFB energies calculated in different bases $N_{OS} = 11,...,21$ (see labels at each curve) as a function of oscillator length b for (a) ^{16}O, and (b) ^{120}Cd. From Ref. [249].

of ^{16}O nucleus become largely insensitive to the numerical parameters N_{OS} and b, see Fig. 5.3 (a). We can thus state that in this case the results are virtually converged to the numerically exact value of HFB energy, thereafter to be referred to as E_∞. However, as was already mentioned, a complete convergence is rarely achieved in practice. For example, the calculated g.s. energies of the neutron-rich ^{120}Cd in Fig. 5.3 (b) are rather sensitive to the chosen intrinsic length of the basis b even in bases with larger N_{OS} values. Hence, further energy gain is anticipated from expanding the dimension of the working basis beyond our current maximum of $N_{OS} = 21$.

We generalize these results and study systematics of the g.s. energy convergence across oxygen and cadmium isotopic chains. In Fig. 5.4 we show the energy gained by increasing the number of SHO shells of the basis with respect to the energy obtained $N_{OS} = 11$ case. Additionally, these values are calculated with an adapted choice of the oscillator length b for each N_{OS},

$$E_{\min}(N_{OS}) = \min\{E(N_{OS}, b)\}, \tag{5.4}$$

i.e., they correspond to the minima of the curves shown in Fig. 5.3. First of all, a flat behavior in the HFB energies with respect to N_{OS} means a converged calculation. However, we see in Fig. 5.4 that a strict convergence is reached only for the nucleus ^{16}O. For the rest of the oxygen and cadmium nuclei we observe an noticeable increase in energy gain when we include more SHO states to the working basis. Such an increase is also observed to grow larger for heavier isotopes. For example, performing calculations in a basis with $N_{OS} = 21$ for ^{16}O yields only ~ 0.06 MeV of extra g.s. energy compared to a calculation with $N_{OS} = 11$, and such gains gradually grow reaching ~ 0.36 MeV for the ^{24}O nucleus. The situation with cadmium nuclei is similar, but the lack of convergence in the $N_{OS} = 11$ basis is much more profound for these heavier systems. Hence, the calculation with $N_{OS} = 11$ is underconverged by 1.70 MeV for ^{90}Cd compared to the calculation with $N_{OS} = 21$, and this value reaches 6.94 MeV for the nucleus ^{152}Cd. In Fig. 5.4 we also observe that the energy gain obtained by increasing the basis with two units of N_{OS} is not always monotonic. To get more insight on this matter, we define

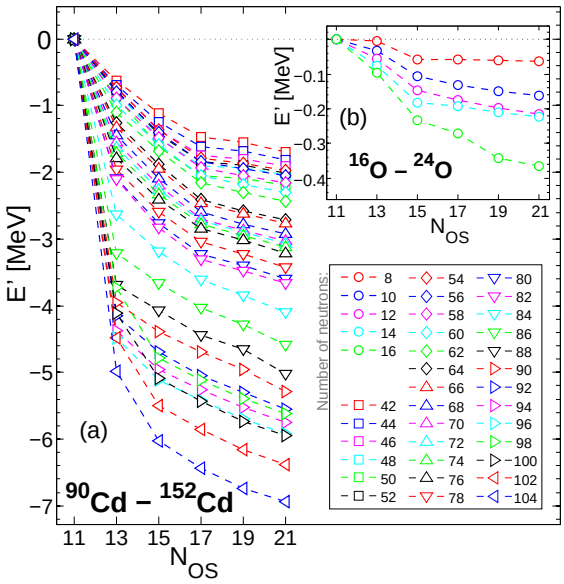

Fig. 5.4: Convergence patters of HFB energies for enlargement of the basis dimension, defined as $E'(N_{OS}) = E_{\min}(N_{OS}) - E_{\min}(11)$ for (a) cadmium, and (b) oxygen nuclei. From Ref. [249].

such the energy gain as

$$\Delta E(N_{OS}) = E_{\min}(N_{OS} - 2) - E_{\min}(N_{OS}), \tag{5.5}$$

Fig. 5.5 shows $\Delta E(N_{OS})$ for $N_{OS} = 17, 19, 21$ in oxygen and cadmium isotopic chains. First, we see once again a fully converged calculation for ^{16}O with $\Delta E(N_{OS})$ effectively being equal to zero. Second, we notice irregularities in the convergence pattern for the majority of nuclei. This is particularly well seen for the cadmium isotopes, where the convergence pattern $\Delta E(21) < \Delta E(19) < \Delta E(17)$ does not generally hold. In addition, we can also notice a clear disturbance of the slowly varying $\Delta E(N_{OS})$ patterns in the isotopic region around the magic ^{130}Cd nucleus. Therefore, any extrapolation method that assumes a continuous and smooth reduction of the energy gain obtained by adding two major shells (implemented in, *e.g.*, Refs. [154, 190, 251, 257]) is not supported by our analysis.

5.5 IR–extrapolation to an infinite basis and its application

The evident incomplete convergence in practical HFB calculations of ground-state energies prompts us to search for a systematic and reliable method to extrapolate the results obtained in a truncated harmonic oscillator basis to the limit of an infinite basis. One of the early attempts to quantify for the numerical error due to the basis truncation is based on the assumption that the g.s. energy follow a law $\Delta E(N_{OS}) \approx \Delta E(N_{OS} - 2)/2$, which by summing the arithmetic series would imply an estimate $E_\infty \approx E_{\min}(N_{OS}) - \Delta E(N_{OS})$ [154, 190, 251, 257]. According to our previous discussion in regard to Fig. 5.5, this ansatz is too crude and not general enough to give a reliable estimation of E_∞. A number of more elaborate phenomenological extrapolation schemes have also been used in nuclear

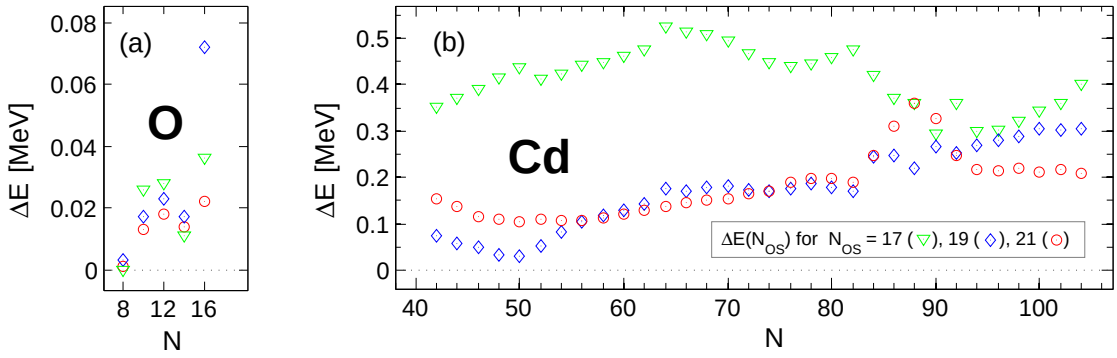

Fig. 5.5: HFB energy gains $\Delta E(N_{OS})$, as defined in Eq. (5.5), for (a) oxygen, and (b) cadmium isotopes. From Ref. [249].

structure calculations [96, 259–261], but most of them include some arbitrary aspects which prevent their use in global calculations.

In the rest of the chapter we analyze the performance of a more general and theoretically justified extrapolation scheme that was first introduced by Furnstahl, Hagen, and Papenbrock in Ref. [252], and subsequently developed in Refs. [253–255]. The underlying idea behind this approach is on a par with assertions of quantum field theories, where the energy of a particle, enclosed in a finite volume, is shifted by the imposed boundary conditions. For example, it was shown in Refs. [262, 263] that the mass of a trapped particle exhibits an exponential convergence to the infinite volume value at a certain theoretically predicted rate. In our case, the corresponding spatial confinement is present by virtue of the localized nature of the SHO basis. The effective dimensions of the enclosing volume are deduced from the spatial extensions of the oscillator functions. By truncating our working basis, we effectively impose a spherical hard-wall boundary condition in coordinate space and an analogous intrinsic sharp boundary in momentum space. These induced infrared (IR) and ultraviolet (UV) cutoffs of the basis, Λ_{IR} and Λ_{UV}, are modulated by the actual nucleus in consideration as well as the model space parameters N_{OS} and b, but are independent of the particular potential used. With the cutoffs explicitly considered, it is possible to derive the finite volume corrections to various nuclear structure observables, such as g.s. energies and radii, hence effectively extending the dimensions of the working basis to infinity.

As a proof of theoretical concept, a row of successful tests for the suggested extrapolation were performed on a number of model potentials, as well as an example of the deuteron with a realistic chiral EFT potential [252]. Although derived at first only for systems that could be reduced to single-particle degrees of freedom, the extrapolations showed a good reliability and robustness even in many-body calculations. Hence, the extrapolation method was used in ^{6}He and ^{16}O nuclei computed with NCSM and CC method, respectively [252]. Since then, the extrapolation for the binding energy has also been applied to several other nuclei [72, 105, 264–266], but without a particular analysis of its reliability.

Based on the previous insights, in Ref. [255], Furnstahl *et al.* have enhanced the theoretical basis of the derived IR–correction formula to extend its applicability to the many-body fermionic systems. The tests performed in three oxygen isotopes, ^{16,22,24}O,

generally confirmed the anticipated improvement of such IR extrapolations for atomic nuclei and brought us closer to the question of error quantification of the extrapolation.

Despite the demonstrated success of the method for these individual nuclei, the proposed scheme has not yet been put to a systematic test with widely used EDFs, exploring its precision, accuracy and reliability throughout the whole isotopic chains, particularly in the neutron-rich extremes of heavier nuclear systems where the lack of convergence is at largest. It is the purpose of this section to systematically test the performance of the suggested energy correction procedure within the HFB framework with the Gogny D1S interaction. We start by introducing the relevant tools for the energy extrapolation on an example of ^{16}O. Later, we check the performance of the method in the nucleus ^{120}Cd. Finally, we perform a systematic study of the IR extrapolation scheme in the cadmium isotopic chain from proton- to neutron-drip lines.

5.5.1 Characteristic cutoffs of the SHO basis

Following the arguments addressed in Refs. [252, 267], there are two momentum cutoffs imposed by the truncation of the model space for a given finite single-particle basis of harmonic oscillator functions. One of the cutoffs is associated with the highest excitation energy of the chosen basis, $E_{max} = \hbar\omega(N_{OS} + 3/2)$ (see Fig. 5.1). In a semiclassical approximation, the maximum momentum a particle in such a basis can reach is $\Lambda_0 \equiv \sqrt{2mE_{max}}$ or in terms of basis parameters

$$\Lambda_0 = \sqrt{2(N_{OS} + 3/2)} \cdot \hbar/b. \tag{5.6}$$

We take this as a leading-order estimate of the corresponding UV momentum cutoff of the basis, *i.e.* $\Lambda_{UV} \approx \Lambda_0$.

The second cutoff is induced in the opposite energy limit of the finite SHO basis, which at low energies is shown to be effectively equivalent to a spherical cavity with a sharp boundary radius L_{IR} [254]. Choosing the classical turning point of the harmonic oscillator $L_0 \equiv \sqrt{2E_{max}/m\omega^2}$, or

$$L_0 = \sqrt{2(N_{OS} + 3/2)} \cdot b, \tag{5.7}$$

as a first-order approximation for this radius suggests $L_{\mathrm{IR}} \approx L_0$. The associated IR cutoff is then defined as $\Lambda_{\mathrm{IR}} \equiv \pi/L_{\mathrm{IR}}$.

The complete convergence in a finite SHO basis can now be attained by the fulfillment of both UV and IR conditions, which, in turn, impose constrains on the choice of the basis. The first requirement is to select the basis in such a way that the highest momentum scale λ of the employed interaction is smaller than the maximum momentum in the working basis, *i.e.* $\lambda < \Lambda_{UV}$. This will ensure that all the ultraviolet physics set by the interaction has been captured in the working basis, which would provide a UV-converged results of the calculation. The second condition requires that the effective spatial radial extent L_{IR} of the chosen basis is large enough to encompass the many-body wave function, *i.e.* $r < L_{IR}$. It is this second condition that can usually never be fully achieved in practice for neutron-rich nuclei due to the different asymptotic behavior of the nuclear wave function (exponential falloff) and the SHO basis (Gaussian falloff) in coordinate space. Thus, in order to obtain the greatest degree of convergence in a truncated model space, one usually performs calculations in the largest accessible basis

dimension N_{OS}, and seeks for an optimal compromise between the IR and UV conditions by finding the binding energy minimum through variation of the intrinsic oscillator length b (see Fig. 5.3). However, selecting calculations performed only with sufficiently small oscillator lengths, one can strive to ensure the UV condition and thereby effectively isolate the systematic error coming from the lack of IR convergence.

While this is easily achievable in the many-body calculations with interactions where the cutoff is set using an UV-regulator, the situation is different in the current EDF approaches. Since the Gogny interaction has contact terms in the spin-orbit and density-dependent part of the functional, it does not have an intrinsic momentum cutoff. A. Rios and R. Sellahewa [268] have recently shown that the D1S parametrization, once decomposed in partial waves, contains significant matrix elements connecting high and low momenta in some channels of the interaction. Nonetheless, it still remains to be investigated, whether these two-body matrix elements have noticeable impact on the whole HFB calculation for a particular nucleus under consideration. However, in many cases we are able *a posteriori* to determine the parameters of the working basis in order to effectively ensure the UV criterium $\lambda < \Lambda_{UV}$, whereupon the IR extrapolation scheme could be applied to account for the IR corrections.

5.5.2 The L_{eff}–parameter and IR–extrapolation scheme

One of the actual challenges in accounting for the boundary effects enacted by the IR-cutoff was the determination of the effective impenetrable extend for the chosen set of SHO basis functions in a most accurate and universal way. The choice of the maximum displacement L_0, can qualitatively explain the concept of extrapolation, but it is only a leading-order estimate for the extent of the oscillator wave function. As it was recently shown, the correct box size of the SHO basis for a many-body system is deduced by matching the smallest eigenvalue of total squared momentum operator for a particular nucleus in a given SHO basis to the analogous smallest value in the spherical cavity [255]. The resulting effective radius L_{eff} is then

$$L_{\text{eff}} = \left(\frac{\sum_{nl} \nu_{nl} a_{ln}^2}{\sum_{nl} \nu_{nl} \kappa_{ln}^2} \right)^{1/2}, \tag{5.8}$$

where the κ_{ln}^2 are the eigenvalues of the momentum squared operator diagonalized in the SHO basis, ν_{nl} are the occupation numbers of nucleons giving the lowest kinetic energy in SHO basis; and a_{ln} are the $(n+1)^{\text{th}}$ zero of the spherical Bessel function j_l.

With the effective hard-wall boundary of the SHO basis properly identified, one can now recast the initial problem of having the given many-body system enclosed by a harmonic oscillator soft-cavity into the one with a sharp infinite potential with an effective radius L_{eff}. Such problems of confined quantum systems have been already studied (*e.g.*, see Ref. [269] and citations therein) with various techniques available for the energy corrections. One can proceed by making a linear energy approximation of the many-body wave function and impose a vanishing Dirichlet boundary conditions at L_{eff}. Whereas the details of the derivation can be found in Ref. [255], the resulting analytical expression of the first-order IR-correction is then of the form

$$E_L(L_{\text{IR}}) = A_\infty \exp\left(-2k_\infty L_{\text{IR}}\right) + E_\infty, \tag{5.9}$$

where, for an atomic nucleus, the proper radius is $L_{\rm IR} = L_{\rm eff}$ that depends both on the basis and the particular isotope, while A_∞, k_∞, and E_∞ are taken as fit parameters. This derived exponential pattern of the IR correction was shown to be independent of the particular potential and validated in the examples mentioned above [253–255].

5.5.3 Proof of concept with ^{16}O

We now illustrate the suggested extrapolation concept and introduce the relevant benchmarking tools for this method using the nucleus ^{16}O as an example. The commencing test with this nucleus is prompted by the well-converged HFB results starting already with a basis of $N_{OS} = 15$, as is evident from Fig. 5.3 (a) and Fig. 5.4. In Fig. 5.6 (a) and Fig. 5.6 (c) we show the HFB energy as a function of the effective radial extent $L_{\rm eff}$. In order to apply the IR corrections, we start by selecting only those calculations for which the UV cutoff of the basis is sufficiently large, so that the results are considered as UV converged. This is done by taking into account only those g.s. energies that are computed in the basis with the UV cutoff above a certain threshold value, that is $\Lambda_{UV} > \Lambda_{thr}$. For this illustration we take $\Lambda_{thr} = 750$ MeV/c, and justify this choice later. The selected HFB energies are represented by the filled symbols in Fig. 5.6 (a). We find that all of them almost perfectly fall on an exponential curve, consistent with the theoretical predictions for the UV-converged results. The observed rise of the g.s. energies at larger values of $L_{\rm eff}$ (Fig. 5.6 (a), open symbols) is due to an insufficient UV convergence. Those calculations are excluded from the fit to the form of Eq. 5.9. The solid lines in Fig. 5.6 (a) represent the separate fits to the HFB energies calculated in different combinations of

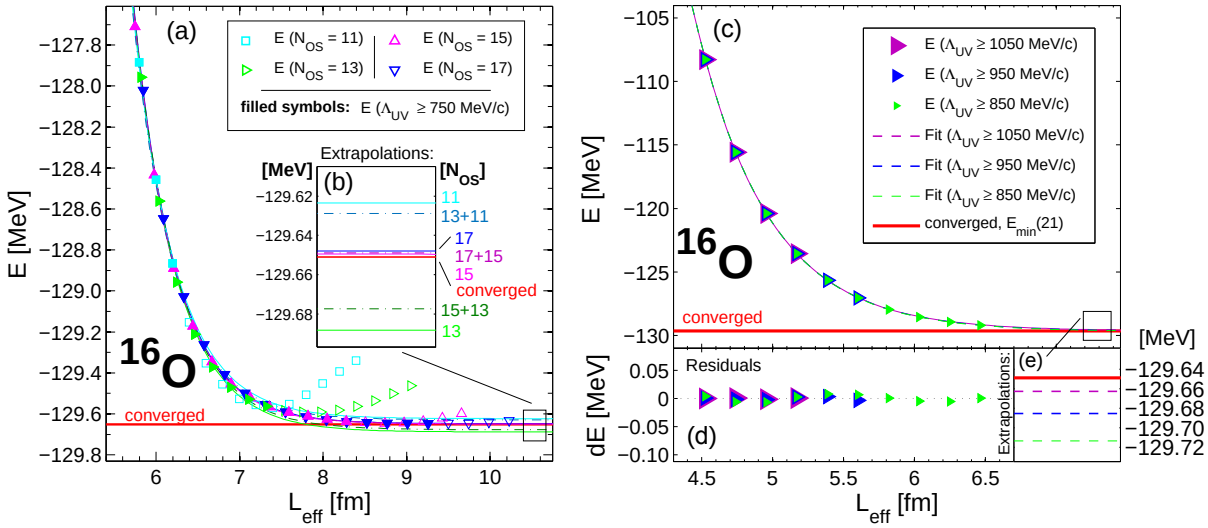

Fig. 5.6: (a) calculated HFB energies for the nucleus ^{16}O using SHO bases with $N_{OS} = 11,...,17$ as a function of $L_{\rm eff}$. Filled symbols indicate g.s. energies having $\Lambda_{UV} > 750$ MeV/c, red line shows the converged result, and other solid and dot-dashed lines are the corresponding fits to Eq. 5.9; (b) inset shows E_∞ values for different extrapolations; (c) HFB energies calculated in a basis having $N_{OS} = 13$ and filtered out by conditions $\Lambda_{\rm thr} = 850, 950$, and 1050 MeV/c. The corresponding fits are shown with dashed lines; (d) residuals defined as $dE = E(L_{\rm eff}) - E_L(L_{\rm eff})$; and (e) the corresponding extrapolations. See figure labels. From Ref. [249].

the basis dimensions N_{OS}. The inset, Fig. 5.6 (b), shows the corresponding extrapolated values E_∞ together with the reference value of a virtually converged calculation $E_{\min}(21)$. We see in this figure that differences of the order of 60 keV are obtained. Although we do not directly attribute such a spread in the extrapolated values to the uncertainty of the method, it is nevertheless representative of the precision and accuracy level of the extrapolation scheme.

However, we have to mention that some of the points used in the extrapolation given in Figs. 5.6 (a,b) are already close to the converged value. In order to imitate a typical situation (common to heavy and neutron-rich nuclear systems) of having access only to an insufficiently large working basis for complete convergence, we limit ourselves now to a SHO basis with $N_{OS} = 13$. In this case the calculations for ^{16}O are not fully converged. Furthermore, an accurate, precise and reliable extrapolation should also be largely insensitive to the choice of the threshold momentum Λ_{thr}, as long as the UV-convergence is ensured. We verify this criterion for ^{16}O by fitting to different sets of HFB calculations, defined by the choice of a threshold value $\Lambda_{thr} = 850, 950, 1050$ MeV/c. The illustration of this benchmark can be seen in Fig. 5.6 (c), where fits for different threshold values are provided by the colored lines. All HFB points are found to be on an exponential curve and the quality of the exponential convergence pattern is particularly well seen in Fig. 5.6 (d). The corresponding E_∞–estimates of the fits, shown in Fig. 5.6 (e), yield a narrow spread of their values, falling very close to the converged energy value $E_{\min}(21)$ even in cases where the closest points used in the fit are a few MeV above this value. This indicates a good stability, accuracy and precision of the method in this specific example.

We now perform a systematic analysis to estimate the dependence of the extrapolated values on the choice of Λ_{thr}. It is expected that below a certain value of Λ_{thr}, the computed HFB energies values could be affected by a lack of UV convergence (or 'UV-contamination'). The knowledge of a lower limit for Λ_{thr} will allow us to include as many computed HFB data points into our extrapolation as possible. To this end, we perform a series of extrapolations obtained in bases with various sets of N_{OS} and b parameters, and vary the threshold momentum across a wide range of $450 \leq \Lambda_{thr} \leq 1250$ MeV/c. In Fig. 5.7 we plot the difference between $E_{\min}(21)$ and the extrapolated values. Hence, positive (negative) values give extrapolated g.s. energies below (above) $E_{\min}(21)$ that is considered as the converged g.s. energy. We observe first that by lowering Λ_{thr} below a certain limit, namely, 620 MeV/c, we start to incorporate into our extrapolation an increasing amount of points which are not sufficiently UV-converged. Therefore, the inclusion of these points deteriorates the quality of the fit and should be eliminated from the IR extrapolating data set. Resting upon the results of these calculations, we estimate that the threshold for a significant UV-contamination lies around $\Lambda_{thr} \approx 750$ MeV/c in ^{16}O. We also observe a slight dependence of the extrapolated g.s. energies on Λ_{thr} of about 0.1 MeV if HFB results with $N_{OS} \leq 15$ are considered, even in the regions well above the estimated onset of the UV-contamination. Consequently, the extrapolated results are not completely free of Λ_{thr} dependencies unless a sufficiently large value of N_{OS} is chosen.

To conclude this section, we summarize the necessary criteria for the IR extrapolation to be robust and reliable. Assuming that the set of parameters (N_{OS}, b) defining the basis of HFB calculations ensures the UV-convergence of the g.s. energies, the following properties must hold for the E_∞ estimates:

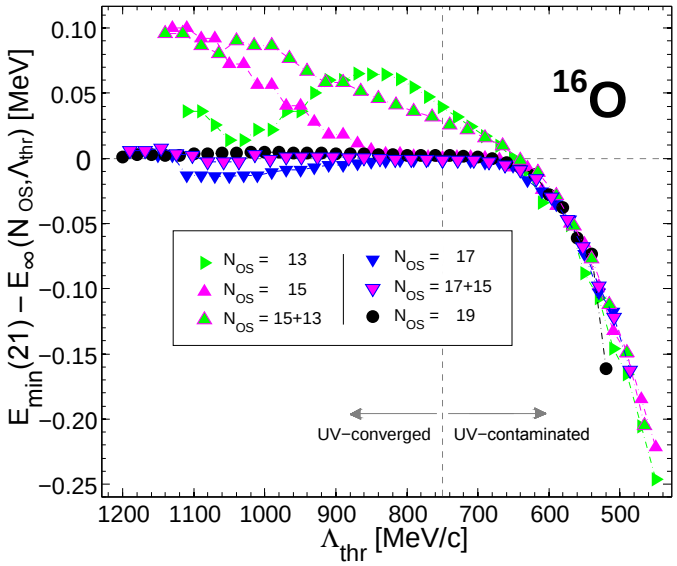

Fig. 5.7: Difference of the calculated $E_{\min}(21)$ and the energy obtained with IR extrapolations from different combinations of basis dimensions N_{OS} and chosen Λ_{thr} values. From Ref. [249].

i. independence of the chosen threshold value Λ_{thr} that define the set of HFB energies used in the fits for extrapolation according to criteria $\Lambda_{UV} > \Lambda_{thr}$;

ii. insensitivity to the basis dimensionality used to compute the HFB energies (as long as the data points are UV-converged). That is, the E_∞ values should be independent of whether we pick a calculation performed with $N_{OS} = 17$, with $N_{OS} = 19$, or even if we combine the two sets;

iii. finally, given that the fully converged value of the HFB g.s. energy is generally unknown, extrapolations should be able to at least reproduce the best converged HFB calculation available, *i.e.* $E_{\min}(21)$ for this work, or yield E_∞ estimates that are below that value.

5.5.4 Further convergence tests with ^{120}Cd

In the previous section we have studied the nucleus ^{16}O to benchmark the IR extrapolation scheme and established the main properties that the extrapolated energy should fulfill. We now apply the same method to extract the E_∞–estimates first for the nucleus ^{120}Cd, and then for the whole cadmium isotopic chain. As we have showed in Figs. 5.3 (b) and 5.4 (a), none of these nuclei is fully converged. The HFB energy as a function of the effective spatial radial extent L_{eff}, and the corresponding fits to Eq. 5.9 for the nucleus ^{120}Cd, are plotted in Fig. 5.8 (a). Following the prescription found in the previous section, we impose a cutoff of $\Lambda_{UV} > 750$ MeV/c to select SHO bases with sufficiently high momentum cutoff. We observe in Fig. 5.8 (a) a qualitative exponential decay with respect to L_{eff}. However, the extrapolated values show a larger spread in absolute energy than in the case of ^{16}O, as can be seen in the inset of Fig. 5.8 (a). For example, E_∞ estimate is about 1.7 MeV lower with the extrapolation from the $N_{OS} = 15$ basis than

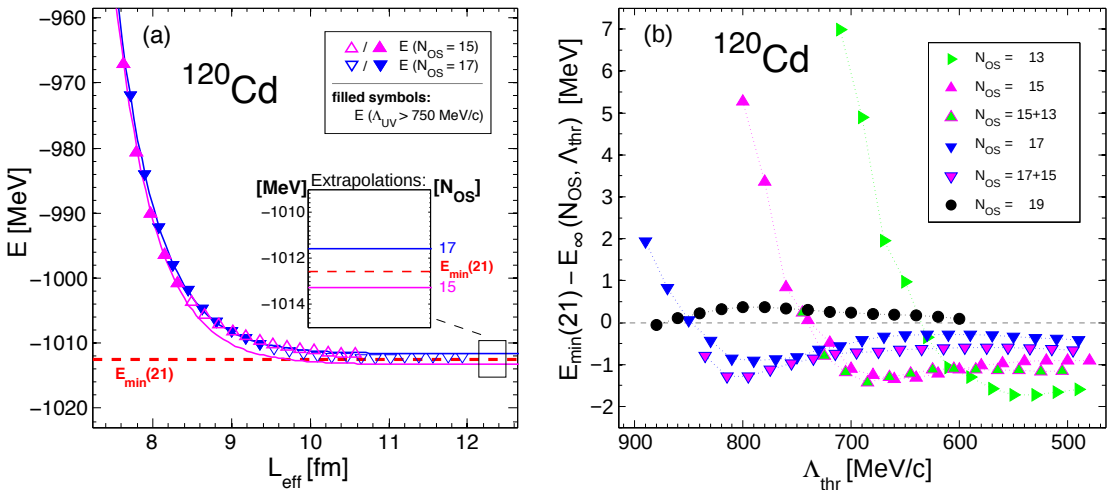

Fig. 5.8: (a) Similar to Fig. 5.6 (a,b), but for ^{120}Cd nucleus for $N_{OS} = 15$ and 17 bases with the $E_{\min}$ values is indicated by the dashed red line; (b) similar to Fig. 5.7 but for ^{120}Cd. From Ref. [249].

from the one with $N_{OS} = 17$. In addition, the minimal g.s. HFB energy attained in $N_{OS} = 21$ basis, *i.e.* $E_{\min}(21)$ value, lies in between the two extrapolated energies mentioned above. Similarly to Fig. 5.7 (b), we plot the dependence of the extrapolated energies on the Λ_{thr} value in Fig. 5.8 for the ^{120}Cd nucleus. In this case the situation is far from fulfilling the requirements for a robust and reliable extrapolation (given in the previous section). We found rather unstable results for extrapolations from $N_{OS} = 13$, 15, and 17 bases for large values of Λ_{thr} that are precisely the ones that should be better UV-converged. In those cases, the spread in the extrapolated energies produced by the particular choice of Λ_{thr} can be as large as 7 MeV. In addition, when the fits are performed for the $N_{OS} = 13$, 15, and 17 results separately, as well as combinations thereof, the extrapolated energies are systematically less bound than the best value reached with $N_{OS} = 21$ basis in the range of Λ_{thr}, where a flatter behavior is found. Since the extrapolation method is intended to estimate the remaining energy missed by the truncation of the working basis, these results are not acceptable. However, the only exception are the extrapolations from HFB energies obtained with $N_{OS} = 19$ basis, which seem to be most reliable.

5.5.5 Analysis of IR–extrapolations in cadmium isotopic chain

Previously we have discussed the performance of the IR extrapolation method for individual nuclei. Now we analyze the reliability and stability of the method in the whole cadmium isotopic chain. According to the points raised in the previous section to define the quality of the extrapolated energies, let us define the following quantities for each nucleus in the chain:

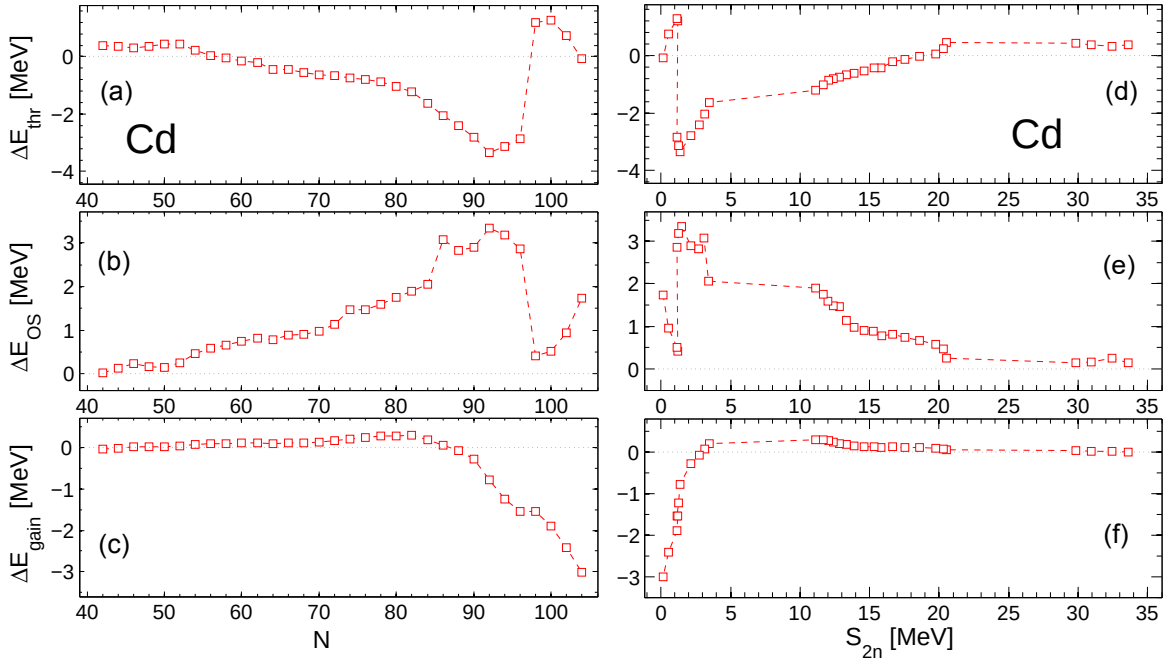

Fig. 5.9: (a) ΔE_{thr}, (b) ΔE_{OS}, and (c) ΔE_{gain} for $^{90-152}$Cd isotopes as a function of the neutron number; (d,e,f) same as in the left panel, but as a function of the S_{2n}, which were obtained directly from HFB calculations in $N_{OS} = 21$ basis *without* extrapolations. From Ref. [249].

i. $\Delta E_{thr} \equiv E_\infty(\Lambda_{thr} = 750\,\mathrm{MeV/c}) - E_\infty(\Lambda_{thr} = 900\,\mathrm{MeV/c})$ with $N_{OS} = 19$ fixed to check the dependence on the chosen threshold value Λ_{thr}. Hence, $\Delta E_{thr} \approx 0$ would mean a good performance;

ii. $\Delta E_{OS} \equiv E_\infty(N_{OS} = 17) - E_\infty(N_{OS} = 19)$ with $\Lambda_{thr} = 750\,\mathrm{MeV/c}$ fixed to check the dependence on N_{OS}. As in the previous point, $\Delta E_{OS} \approx 0$ would mean a good performance;

iii. $\Delta E_{\mathrm{gain}} \equiv E_{\mathrm{min}}(21) - E_\infty(N_{OS} = 19, \Lambda_{thr} = 750\,\mathrm{MeV/c})$ to check the quality of the extrapolation with respect to the lowest HFB energy computed in this work. Thus, ΔE_{gain} should be equal to zero for converged cases and slightly positive for those HFB calculations which are not converged.

In Fig. 5.9 (a,b,c) we show these three quantities as a function of the number of neutrons in the nuclei $^{90-152}$Cd. We observe first that the three conditions given above are not completely fulfilled simultaneously throughout the whole cadmium isotopic chain. Nevertheless, for many nuclei, the dependencies on Λ_{thr} and N_{OS} are rather mild with $|\Delta E_{OS}| \approx |\Delta E_{thr}| \leq 2$ MeV in the range of $N = 42 - 84$. In this region, the differences of the extrapolated energies with respect to the best values obtained with $N_{OS} = 21$ basis are close to zero or slightly above, providing a physically sound extrapolation. However, the situation is different in the neutron rich region above $N \geq 86$, where the extrapolations are remarkably dependent on the choice of both Λ_{thr} and N_{OS}, as well as lie above the best HFB energies directly computed, *i.e.* $\Delta E_{\mathrm{gain}} < 0$. Therefore,

whereas in the first region some systematic error estimates could be extracted from the extrapolation, that is not the case in the neutron-rich region.

Fig. 5.9 (d,e,f) shows the same quantities as left panel, but as a function of the two-neutron separation energy

$$S_{2n}(N) \equiv E(Z, N-2) - E(Z, N), \tag{5.10}$$

where the shell gaps, corresponding to $N = 50$ and 82 magic numbers, are well seen. From the astrophysical point of view, the most interesting aspect is that the ill-behavior of the extrapolation method with the present EDF is significantly larger for isotopes beyond $N = 82$ when the two-neutron separation energy is less than 5 MeV approximately, which is precisely the relevant range in r-process calculations.

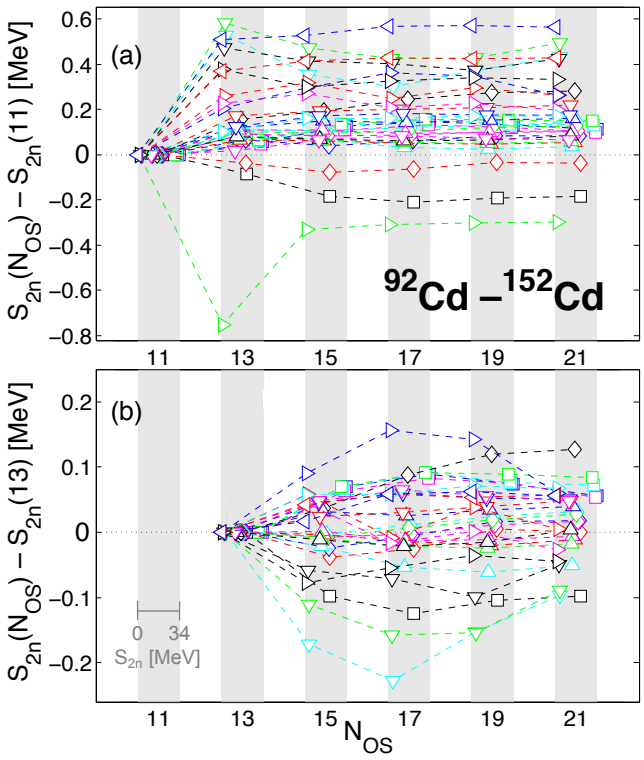

Fig. 5.10: S_{2n} energies of cadmium isotopes calculated in different basis dimensions (shaded bins). Same legend as in Fig. 5.4. From Ref. [249].

A similar result is obtained in the magnesium isotopic chain (not shown) where such an erratic behavior of the extrapolated energy is also found in the neutron rich part of the chain ($S_{2n} \leq 5$ MeV). Therefore, the present extrapolation scheme with Gogny EDF is not able to provide reliable estimations of E_∞ values in those loosely-bound regions, where the lack of convergence is also the largest. One possible explanation is that the momentum threshold chosen to select the set of points used for the extrapolations, though in some case as large as $\Lambda_{thr} = 1200$ MeV/c, is not large enough to ensure the UV-convergence. This could be justified by the absence of an explicit regulator in momentum space in the Gogny EDF.

Another complementary explanation could be the fact that a simple exponential extrapolation cannot fully capture the IR physics of the present EDF. By the same arguments, the considered extrapolation scheme cannot be used to extract the two-neutron separation energies from the E_∞ values. Despite this, being energy differences of the neighboring nuclei, the particle separation energies are expected to be better converged. Indeed, this is the case as can be seen in Fig. 5.10, where calculated S_{2n} values are shown without any extrapolations. The obtained energies are distributed among the shaded column bins according to the basis dimensions of the calculations. Moreover, in order to see the convergence patterns more clear, the separation energies for each isotope are shifted down by a constant that equals to the S_{2n} value obtained in N_{OS}=11 (Fig. 5.10 (a)), or in N_{OS}=13 (Fig. 5.10 (b))

basis. Furthermore, for better readability, the two-neutron separation energies are also displaced within each column bin so that the lower absolute S_{2n} values are shifted closer to the left edge of each shaded region, while the higher ones are closer to the right edge (by analogy to Fig. 5.9 (b)). We see that for isotopes having $S_{2n} > 5$ MeV, the enlargement of the basis beyond $N_{OS} = 11$ affects their values up to 0.3 MeV at most, Fig. 5.10 (a). For nuclei which have $S_{2n} < 5$ MeV the spread around zero reference value is about double as high, reaching as much as 0.6 MeV for the dripline isotope ^{152}Cd predicted by Gogny D1S EDF. By the same token, Fig. 5.10 (b) shows the convergence patterns zeroed out for a somewhat larger $N_{OS} = 13$ basis. Here we see that almost all of the S_{2n} values in $N_{OS} = 21$ basis fall within 0.1 MeV spread. However, we observe somewhat larger spread for nuclei having $S_{2n} < 5$ MeV in $N_{OS} = 15, 17$, and 19 bases. All in all, despite the fact that two-neutron separation energies do not exhibit any noticeable convergence pattern when the basis size is increased, these quantities reach a much better degree on convergence already in relatively small bases.

5.6 Summary of results and discussion

We have studied the convergence pattern of the HFB energies as a function of the maximum number N_{OS} of SHO shells included in the working basis, as well as a function of the oscillator length b. The calculations were performed with the Gogny D1S parametrization. Generally, one has to include a prohibitively large number of major oscillator shells in the working basis to ensure convergence in practical calculations. In order to circumvent this shortcoming, one can opt to use various extrapolation techniques to obtain an estimate of the converged observables. While the ansatz $\Delta E(N_{OS}) \approx \Delta E(N_{OS} - 2)/2$, that in central in a purely phenomenological energy correction scheme [154, 251], proved generally *not* to hold, we have systematically studied one of the most promising IR–extrapolation schemes that was recently proposed [255].

We have seen that the application of the considered IR extrapolation to a playground case of ^{16}O seems to work nearly perfect, providing reliable results that are both threshold-independent and consistent with the fully converged reference value. A more serious benchmark, first by application to the nucleus ^{120}Cd, and then to the whole set of nuclei in the cadmium isotopic chain, revealed, however, some limitations of the proposed scheme for the HFB energy obtained with Gogny D1S EDF.

Fig. 5.11 summarizes the conducted analysis of IR–extrapolations scheme for cadmium isotopes, as well as extends the scope of the study to tin and tellurium nuclei. As it is the case with all considered isotopic chains, the most robust extrapolations are obtained for isotopes in the direct vicinity to the stability region. Nevertheless, in this region the extrapolations are least relevant due to the larger degree of convergence of the HFB calculations in comparison to the neutron-rich isotopes. However, as one moves away towards the neutron-drip line, the IR extrapolations fails to yield reliable results. In particular, the discrepancy of the extrapolations from $N_{OS} = 17$ and $N_{OS} = 19$ values (with $\Lambda_{thr} = 750$ MeV/c) reach easily up to 5–8 MeV. Besides that, varying Λ_{thr} for neutron–rich nuclei has a much greater impact on the estimated E_∞ values (spanning energies of $10 - 15$ MeV for $A \sim 115$). Finally, we also notice that the IR corrections can no longer even reproduce the most converged HFB calculations at hand (*i.e.* the $E_{\min}(21)$ values) in the neutron–rich tail of the isotopic chain, which is evident by the negative unphysical estimates for $N \gtrsim 96$ on Fig. 5.11. These results have been supported

by similar findings for a more simplistic version of IR-extrapolations in cases of other isotopic chains as well [247].

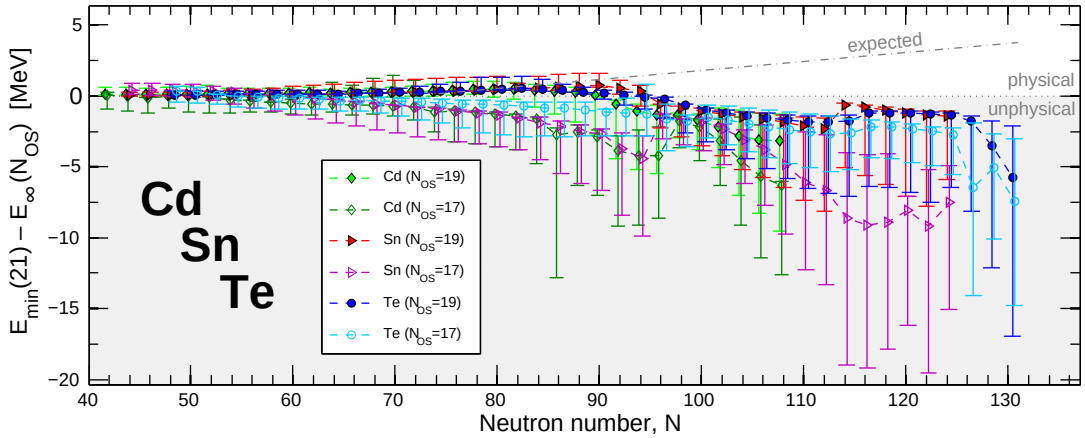

Fig. 5.11: Results of IR extrapolation for nuclei in cadmium, tin, and tellurium isotopic chains as the function of neutron number in form of the differences $E_{\min}(21) - E_{\infty}(N_{OS})$ with momentum threshold $\Lambda_{thr} = 750$ MeV/c. Two dimensions of model space is considered, $N_{OS} = 17$ (open symbols) and $N_{OS} = 19$ (solid symbols), separately. The associated errorbars represent the spread in corresponding E_{∞} values from the variation of the threshold parameter in the interval 700 MeV/c $< \Lambda_{thr} <$ 900 MeV/c. From Ref. [249].

To summarize, our HFB calculations with Gogny EDF show that the investigated extrapolation schemes are so far applicable only in the regions of well-bound nuclei. The origin of these behavior could be the lack of UV-convergence even in harmonic oscillator basis with a momentum cutoff of ~ 1 GeV/c due to the presence of contact terms in the Gogny interaction (and in most of the EDF used nowadays). In such a case, the IR extrapolation should not be applied unless an ultraviolet regulator is explicitly included in the EDF approach. Additionally, it is also possible that even though the calculations are UV-converged, the simple exponential extrapolation is not enough to produce physically sound extrapolated HFB energies with the present functional. Disentangling these two aspects requires to either explicitly include a momentum regulator in the EDF approach or to consider a functional form that is entirely of finite-range structure.

6 Beyond-mean-field calculations of masses and low-energy spectra

Having performed convergence analysis of the binding and separation energies in harmonic oscillator basis in the previous chapter, we were able to significantly improve the numerical aspects related to convergence of HFB calculations. In this chapter we study the impact from the enhancement of the physical desciption of the nuclear many-body problem by going beyond the static mean-field picture. In particular, we perform particle-number and angular-momentum projections, as well as configuration-mixing calculations for all doubly even experimentally known nuclei using D1S and D1M parametrizations of Gogny interaction. We systematically analyze the correlation energies from each of the implemented BMF methods, and augment the HFB calculations with the obtained BMF corrections. We compare our results to the experimentally known nuclear masses, two-particle separation energies, and 2^+ first-excited states. This chapter is mainly based on the results published in Ref. [270].

6.1 Introduction

As mentioned previously in Chap. 3, many of the short-range nuclear correlations are effectively subsumed in the effective interactions for the mean-field (MF) approach. However, not all of them can be included through the renormalization of the short-range part of a particular EDF. Many of such beyond-mean-field (BMF) rotational and vibrarional corrections were previously included phenomenologically [271]. With the recent increase in computational capabilities, a more rigourous treatment of the BMF corrections by means of symmetry restoration and configuration mixing became available [146]. As for global calculations of doubly even nuclei, some of the BMF effects were included using a collective Hamiltonian method with relativistic Lagrangian [272] and Gogny interaction [154, 199, 236], as well as projection techniques within the generator coordinate method (GCM) for the Skyrme-type functionals [245, 273]. All of the published global BMF calculations were performed with the so-called Gaussian-overlap approximation (GOA) in order to lower the extensive computational cost [274]. Despite that the nuclear systems with odd number of particles are still computationally very demanding to be systematically treated within the advanced BMF framework, the projecting techniques have already been tested on a row of selected odd-A nuclei [275, 276].

This global survey is performed both with an established D1S [193, 194], as well as the newer D1M [154] Gogny parametrizations (Sec. 3.2). The GCM and symmetry-restoration methods are implemented without the previously adopted GOA approximation. We explicitly explore the quadrupole degree of freedom withing the GCM frame-

work, while assuming axially symmetric and parity-conserving nuclear states. Inclusion of other multipole deformations would render such large-scale calculations unfeasible due to a highly demanding computation cost. Nonetheless, it should be noted that many transitional nuclei possess a soft triaxial potential and, according to recent global survey [277], are found to have an overall triaxial binding energy minimum. Besides this, some nuclei have been reported to favor triaxial quadrupole configurations over axial quadrupole ones only after performing angular-momentum projection [278], which stresses once again the importantance to include triaxiality in the future BMF methods. However, apart from a few isotopic chains with identified triaxial and octupole deformation [199, 277, 279], the mass-correction from inclusion of such degrees of freedom to the calculation procedure was reported to be very small [280], and is expected to vary mostly smoothly with mass number, yielding predominantly a constant shift of the binding energies. This, in turn, will have only a limited effect on the derivative values, such as the neutron- and proton-separation energies, or the pairing gaps (see Ref. [270] for discussion).

The theoretical background for this study is available in Chap. 4, and the computational details of the BMF corrections along with the brief convergence analysis are presented in Sec. 6.2. The detailed analysis of calculated total binding energies and the impact from successive application of BMF methods are found in Sec. 6.3.1. The comparison of the obtained results to the experimental values of the nuclear masses is performed in Sec. 6.3.2, and two-nucleon separation energies are discussed in Sec. 6.3.3. A quick survey of the 2^+ first-excited states is presented in Sec. 6.3.4. Finally, the results of this survey are summarized in Sec. 6.4.

6.2 Computational details of BMF corrections

In order to achieve the best possible degree of convergence of our results on the one hand, as well as to reduce the highly demanding computational effort required for the BMF calculations on the other hand, the total binding energy of the nuclear system is split into two parts as

$$E = E_{\mathrm{HFB}} + \Delta E_{\mathrm{BMF}}. \tag{6.1}$$

The first term, E_{HFB}, is the mean-field HFB ground-state (g.s.) binding energy (Sec. 4.1) calculated in $N_{OS} = 19$ SHO basis. The E_{HFB} was computed using the HFBAXIAL code [281]. The calculation was carried out with an optimization of oscillator length b to ensure the lowest binding energy of the solution, while also exploring the quadrupole deformation parameter β_2 to ensure the convergence of the HFB results to the *global* energy potential minima. The Gogny interaction (Sec. 3.2) has been incorporated in a most exact manner, *i.e.* including pairing, direct, and exchange terms of both nuclear *and* Coulomb potential.

The second term of Eq. (6.1), ΔE_{BMF}, corresponds to correction beyond the mean-field approximation calculated in a basis of $N_{OS} = 11$ dimension to reduce the computational cost. The BMF corrections consist of particle-number restoration (Sec. 4.2.2), angular-momentum projection (Sec. 4.2.3), as well as quadrupole shape-mixing of the symmetry-restored axially symmetric states withing the GCM framework (Sec. 4.2.1). The BMF corrections ΔE_{BMF} are defined as

$$\Delta E_{\mathrm{BMF}} = E_{\mathrm{BMF}} - E_{\mathrm{HFB}} \tag{6.2}$$

and, being an absolute energy difference, are expected to show reduced dependence on the size of the basis. The total BMF binding energy corresponds to the SCCM energy (derived in Sec. 4.2.4), *i.e.*

$$E_{\mathrm{BMF}} = E^{I=0\sigma=1}_{\mathrm{SCCM}}. \tag{6.3}$$

The particle-number (PN-VAP) and angular-momentum (PNAMP) projections, as well as symmetry-conserving configuration-mixing (SCCM) calculations were performed with the codes developed at Universidad Autónoma de Madrid [282, 283]. Additional highly optimized scripts for large-scale calculations were run on super-computer clusters in GSI [284] and Frankfurt University [285]. Similarly to HFB case, the BMF calculations incorporate Gogny and Coulomb interactions in an exact manner with pairing, direct, and exchange terms.

Depending on the particular nucleus, a number between 15 and 20 intrinsic PN-VAP states with a broad range of quadrupole deformations were used in the SCCM-calculation. The PN-VAP calculation included 9 gauge angles for particle-number restoration, and implementation of PNAMP was based on 16 Euler angles for angular-momentum projection, while the convergence of the projected calculations was determined by analyzing the expectation values of $\hat{N}$, $\hat{Z}$, $\Delta\hat{N}^2$, $\Delta\hat{Z}^2$, and $\hat{J}^2$. As for the configuration mixing, the degree of convergence of the Hill-Wheeler-Griffin (HWG) equations were checked by studying the energy plateaus as a function of the natural states which transform the HWG equations into regular eigenvalue problems [270] (see also Refs. [283, 286] for details).

Additionally, the 2^+_1–excitation energies are readily obtained withing the SCCM framework as

$$E(2^+_1) = E^{I=2\sigma=1}_{\mathrm{SCCM}} - E^{I=0\sigma=1}_{\mathrm{SCCM}}, \tag{6.4}$$

and are also examined later in Sec. 6.3.4.

The Fig. 6.1 illustrates the BMF calculation procedure on an example of ^{120}Cd nucleus. The potential energy curve (PEC) of the axial quadrupole deformation obtained with HFB calculation in $N_{OS} = 19$ basis, is shown as the green curve. The global energy minimum (marked with square symbol) appears at $\beta_2 = 0.15$, and corresponds to a slightly prolate deformation with $E_{\mathrm{HFB}} = -1011.79$ MeV. By restoring the particle number with the variation after projection (PN-VAP) method, a deeper PEC is achieved, which is shown by the red curve. The new global energy minimum is marked with a red triangle. The resulting energy gains are $\Delta E_{\text{PN-VAP}} \approx 1.96$ MeV. Further correlations are included by performing a simultaneous particle-number and $J = 0$ angular-momentum projections (PNAMP). The PNAMP calculation leads to a formation of two energy minima at $\beta_2 \approx -0.10$ and $\beta_2 \approx 0.18$ with the anticipated zero energy gain for a spherical nuclear that is already in the $J=0$ state. The PEC for PNAMP is shown with the black solid curve. This step gains additional $\Delta E_{\mathrm{PNAMP}} \approx 2.8$ MeV of binding energy in comparison to the PN-VAP state. The last BMF correlations are taking into account by mixing the PNAMP–states with different quadrupole deformations according to the GCM method. The squared values for the collective wave function $|G(\beta_2)|^2$, which we have defined in Eq. (4.53) of Sec. 4.2.1, represents the probability composition in the linear combination of the β_2–states comprising the GCM solution. These values are shown with the solid blue curve and correspond to the right y-axis of Fig. 6.1. The ^{120}Cd nucleus exhibit a noticeable configuration mixing of an oblate state (with a maximum at $\beta_2 \approx -0.1$), and a prolate state (with a maximum at $\beta_2 \approx +0.2$), resulting in the mean

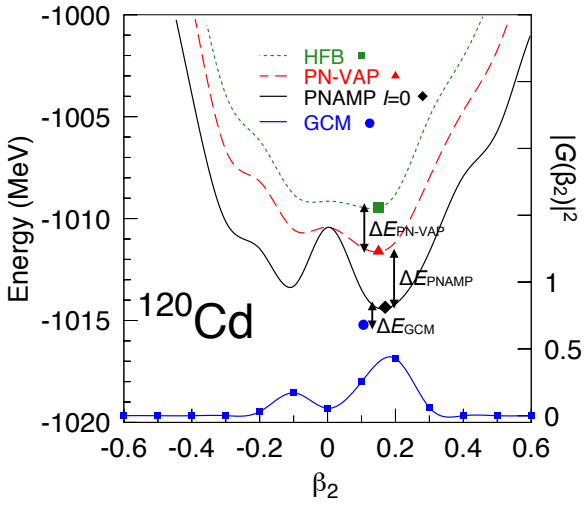

Fig. 6.1: PECs calculated with HFB, PN-VAP, PNAMP, and GCM methods for ^{120}Cd using Gogny D1S. The global enegy minima, as well as the corresponding binding energy gains from successive inclusion of the mentioned BMF correlations are shown. The square of the collective wave function $G(\beta_2)$, associated with probability amplitute according to Eq. (4.53), is shown with blue squares, which are connected by a solid line to guide the eye (right y-axis). Adapted from Ref. [270].

deformation of $\bar{\beta}_2 = 0.10$ (marked with a single blue circle in Fig. 6.1). The shape-mixing yields another $\Delta E_{\mathrm{GCM}} \approx 1.02$ MeV of additional binding energy, amounting to a total of $\Delta E_{\mathrm{BMF}} \approx 5.77$ MeV of cumulative BMF correlation energy, and thereby lowering the total binding energy of ^{120}Cd to $E_{\mathrm{BMF}} = -1017.56$ MeV.

The Fig. 6.2 shows convergence patterns of g.s. binding energies for ^{120}Cd and ^{194}Po, calculated in different basis dimensions with HFB approximation, as well as the mentioned BMF techniques. First of all, the degree of convergence of the absolute binding energy for the medium mass ^{120}Cd nucleus is noticeably greater than for the heavier ^{194}Po isotope. That is evident by lesser energy gains for ^{120}Cd from the SHO basis enlargements than for ^{194}Po. Moreover, due to variational nature of all presented methods, including additional BMF correlations projects the given intrinsic state to a linear combinations of Slater determinant configurations (Sec. 4.2), and by that effectively enlarges variational space, which, in turn, always produces deeper binding energies. This is, for example, confirmed by Fig. 6.2, where the separate lines maintain their order, and do not cross. The average computation times are shown for a selection of SHO bases to point out an approximate computational expense for different methods. For example, a single HFB calculation in a relatively large $N_{OS} = 19$ basis takes about ~ 2.5 hours on a single core, whereas a similar amount of time is already needed for a single PN-VAP calculation in a significantly smaller $N_{OS} = 11$ basis. Enlarging the basis dimension to $N_{OS} = 13$ almost triples the PN-VAP computational time to $\sim$120 hours, and reaches a tremendous 21–days estimate for $N_{OS} = 17$ basis. The provided times are averages of a single calculation, and are dependent on a particular nucleus in consideration. Despite that, as can be seen in Fig. 6.2, the GCM calculations are somewhat less time-demanding, but aiming to perform a large-scale calculation with BMF corrections up to the neutron drip line would include more than ~ 2200 doubly even nuclei. Restricting our study

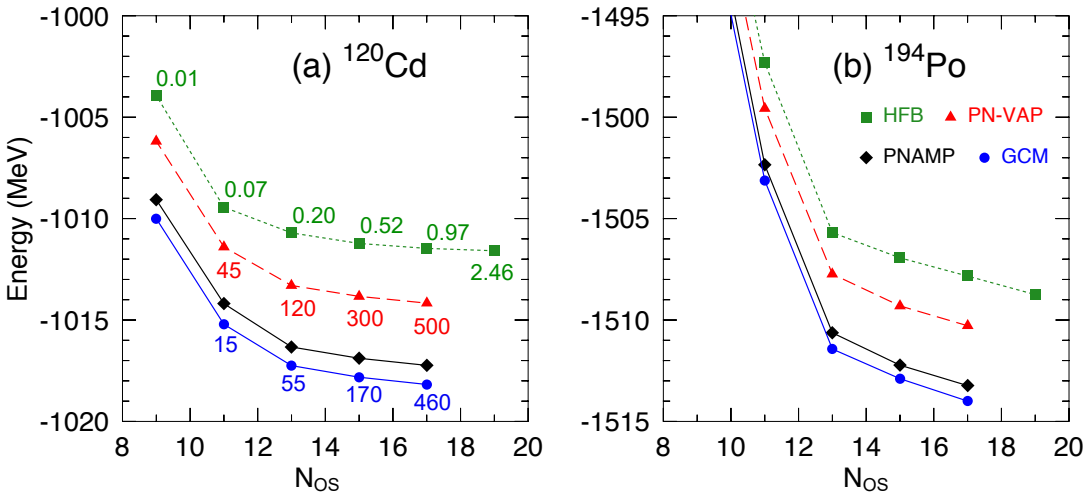

Fig. 6.2: Convergence of the g.s. binding energies from enlargement of the SHO basis calculated with the various many-body methods for (a) ^{120}Cd and (b) ^{194}Po. Approximate computational times in *hours* of a single nucleus on a single core at the GSI cluster [284] are also shown next to the corresponding calculation points. Adapted from Ref. [270].

to only experimentally known nuclei listed in AME12, will reduce this number to 598 isotopes, but performing it both for D1S and D1M Gogny parametrizations would again double the number, rendering such a survey beyond $N_{OS} = 11$ SHO basis as unbearably heavy. Nonetheless, the connected lines of different methods in Fig. 6.2 can be seen as being almost parallel to each other, indicating a much less pronounced dependence of the $\Delta E_{\text{PN-VAP}}$, ΔE_{PNAMP}, and ΔE_{GCM} gains on the particular basis dimension.

In order to check the quality of the computationally optimized results obtained with Eq. (6.2) against the time-demanding SCCM calculations performed entirely in $N_{OS} = 17$ basis, we plot in Fig. 6.3 the *Shell Effects* for $_{80}$Hg, $_{82}$Pb, and $_{84}$Po–chains, extracted from HFB and GCM calculations in both $N_{OS} = 11$ and $N_{OS} = 17$ bases. The lack of convergence of the total binding energies calculated in the $N_{OS} = 11$ basis relative to the $N_{OS} = 17$ basis appears to be as large as ~ 10 MeV both for HFB and BMF energies. However, adding the BMF corrections from $N_{OS} = 11$ basis on top of HFB calculation in $N_{OS} = 17$ basis (magenta open circles, according to Eq. (6.2)) closely reproduces the GCM energies obtained entirely in $N_{OS} = 17$ oscillator basis (shown in blue in lower panels of Figs. 6.3). The mentioned computational demands in junctions with the presented analysis of Shell Effects reasonably justifies the choice to split the BMF calculation according to the Eq. (6.2). However, the drawback of such a split is a minor artificial numerical noise that can appear in ΔE_{BMF} energies, if $N_{OS} = 11$ oscillator basis is not large enough to adequately incorporate UV and IR physics of the wave function (see Sec. 5.5.1). Having benchmarked the employed approach of the BMF calculations, we proceed further to the results.

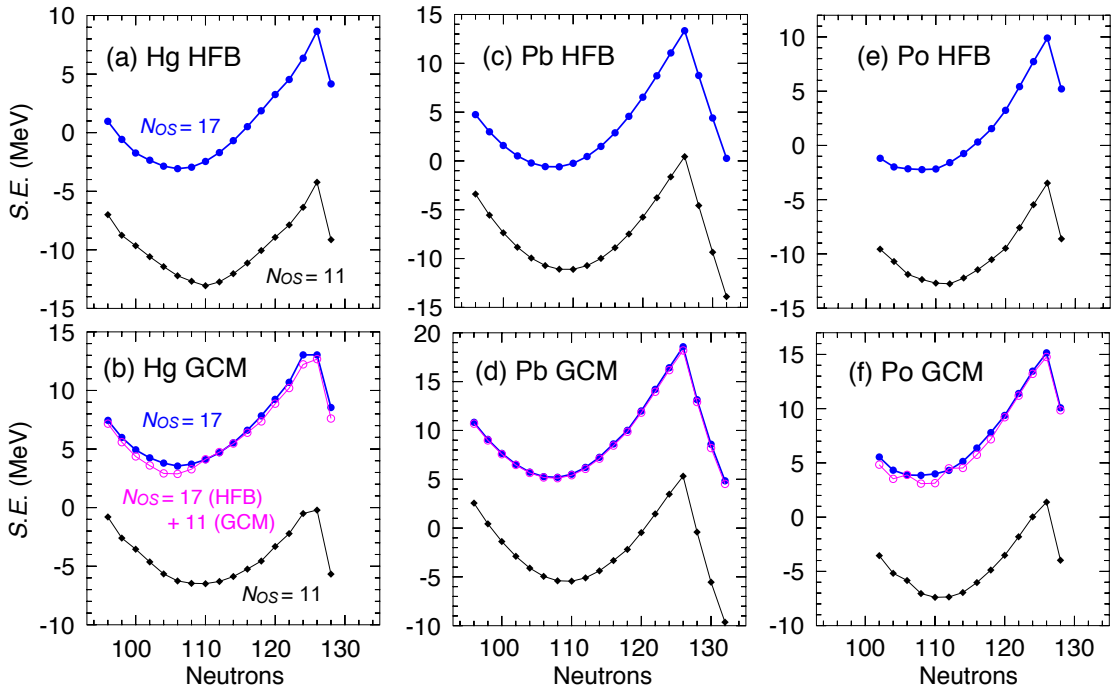

Fig. 6.3: Shell Effects, defined in Eq. (5.3), of HFB calculations in $N_{OS} = 11$ (black solid diamonds) and $N_{OS} = 17$ (blue solid cicles) SHO bases for (a) $_{80}$Hg, (b) $_{82}$Pb, and (c) $_{84}$Po. The (b,d,f) plots show the Shell Effects calculated in the same SHO bases but for GCM method, as well as a mixed calculation (open magenta circles) in accordance to Eq. (6.1). Adapted from Ref. [270].

6.3 Global BMF calculation

In what follows we discuss the results of the performed global BMF calculation of doubly even nuclei whose masses are known experimentally. We start off with a detailed analysis of calculated total binding energies and the impact from successive application of symmetry restoration and the configuration mixing methods in Sec. 6.3.1. Later we also compare the obtained results to the experimental values of the masses in Sec. 6.3.2, and two-nucleon separation energies in Sec. 6.3.3. Finally, a quick survey of the 2^+ first-excited states calculated within the GCM framework, as well as a comparison to the empirical values, is presented in Sec. 6.3.4.

6.3.1 Correlation energies of BMF methods

The graphs in Fig. 6.4 show the results of successive applications of BMF corrections globally for experimentally known doubly-even nuclei. The calculations were performed both with D1S and D1M Gogny interaction, which turn out to produce very similar results. When plotted as a function of neutron number on Fig. 6.4 (a,b), or proton numbers on Fig. 6.4 (i,j), most of the PN-VAP correlations lie in the $1.5 - 3.5$ MeV range, while having a mean value of $\sim$2.3 MeV. As for the PNAMP correlations the, the energy gains compared to PN-VAP calculations are of the $\sim$2.7 MeV order on average both as a function of neutrons (Fig. 6.4 (c,d)), as well as of protons (Fig. 6.4 (k,l)). Both PN-VAP and PNAMP show well established oscillating patterns of energy gains,

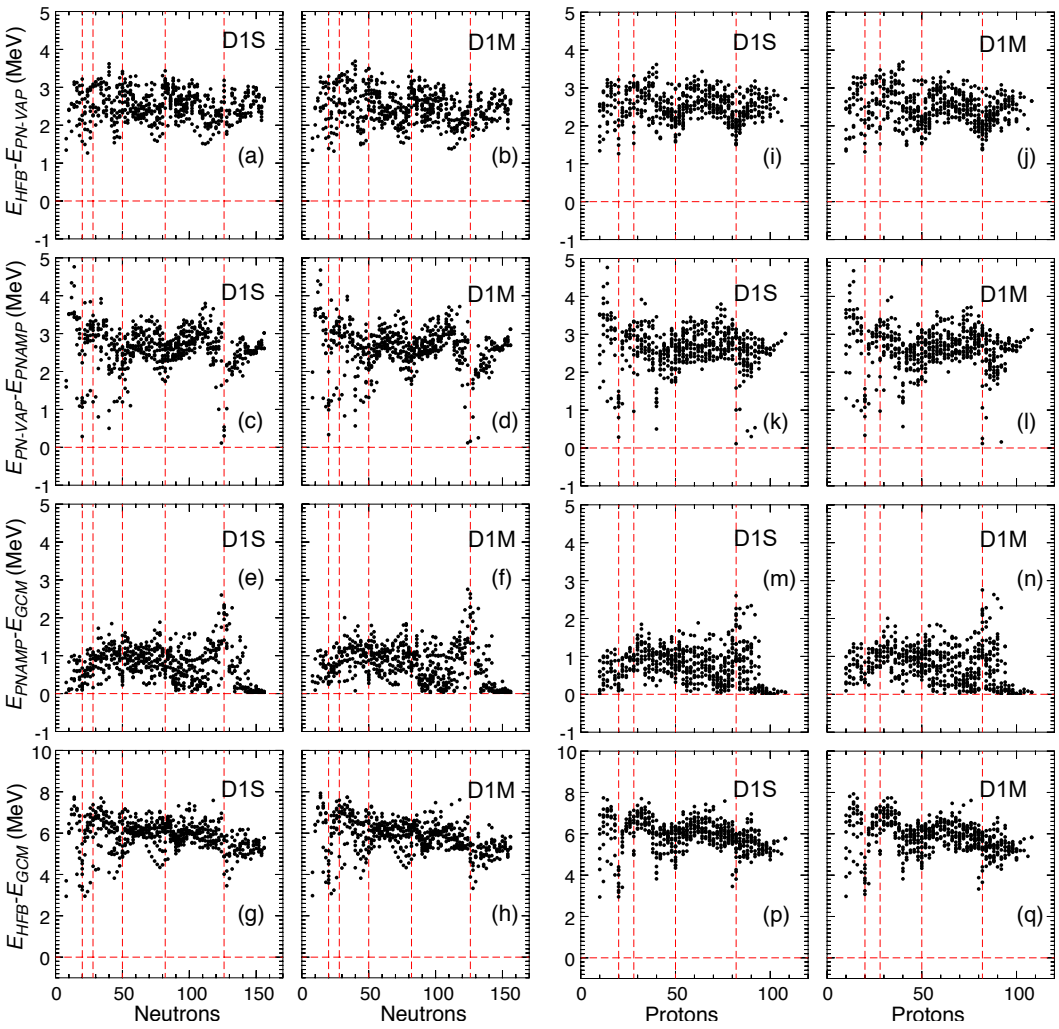

Fig. 6.4: Binding energy gains from successive inlcusions of BMF corrections as a function of neutrons (left side), and protons (right side) both for Gogny D1S and D1M parametrizations (see labels). Vertical dashed lines indicate neutron and proton magic numbers. Adapted from Ref. [270].

which in one or the other way correspond to the neutron and proton magic numbers. As for the GCM calculations, the energy corrections also show parabolic behaviour around shell closures, with the most noticeable peak at $N = 126$ (Fig. 6.4 (e,f)), and around $Z = 82$ both for D1S and D1M (Fig. 6.4 (m,n)). The overall mean energy gain for solely configuration mixing is ~ 0.8 MeV. Finally, the cumulative BMF correlations as a function of neutrons are shown on Fig. 6.4 (g,h), and as proton function on Fig. 6.4 (p,q). A negative slope for BMF correlations is well visible, and the the energy gains amount to $5 - 7$ MeV of energy correction to HFB results. The parabolic patterns with minima at or around neutron and proton shell closures tend to compensate the inverted oscillating patterns seen on Fig. 5.2.

Because the axial quadrupole deformations are pivotal in both PNAMP and GCM methods, we also plot the considered BMF corrections for all calculated nuclei as a function of β_2 in Fig. 6.5. First of all, the spherical isotopes show the largest span of

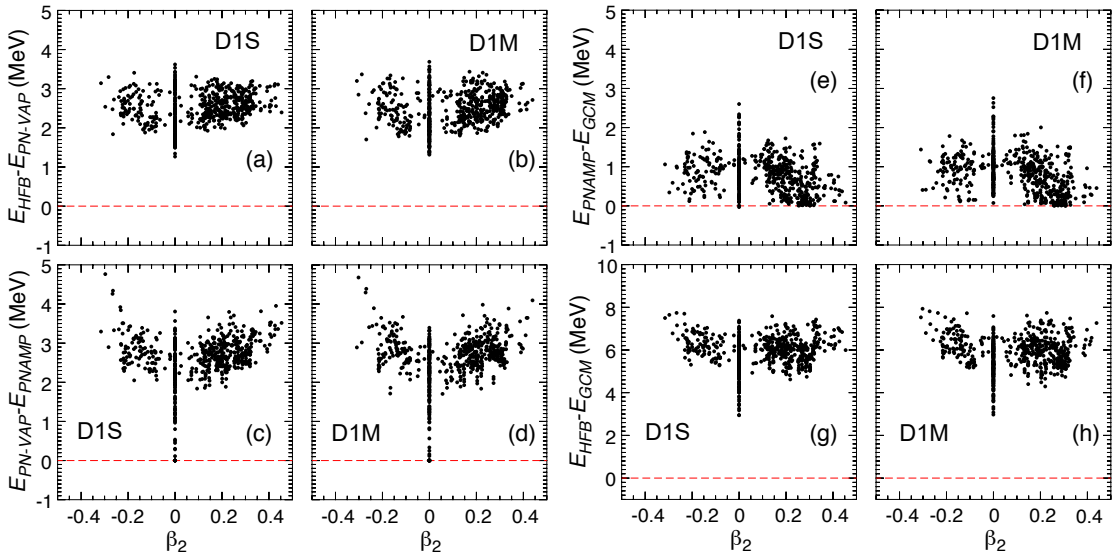

Fig. 6.5: Similar to Fig. 6.4, but the BMF energy gains are plotted against β_2 quadrupole deformation parameter. Adapted from Ref. [270].

correlation energies for all the approaches, ranging from zero up to $\sim$3.7 MeV. Most of the deformed nuclei are found to be of prolate shapes in the range of $\beta_2 \approx +0.1 \sim +0.35$, while most of the oblate nuclei found to have $\beta_2 \approx -0.05 \sim -0.2$. No specific trends are identifiable for the PN-VAP corrections, which produce $\Delta E_{\text{PN-VAP}} \approx 2-3$ MeV of correlations for all non-spherical nuclei, Fig. 6.5 (a,b). However, as is seen on Fig. 6.5 (c,d), while quantitatively of the same strength as the former, the PNAMP approach yields larger energy gains for the well-deformed nuclei than for the nuclei that exhibit smaller quadrupole deformations. The configuration mixing within GCM method, on the other hand, is seen to somewhat compensate the identified pattern of PNAMP corrections by providing an invert behavior, Fig. 6.5 (c,d). Similar trends for PNAMP and GCM corrections were also found for Skyrme SLy4 interaction in Ref. [245]. Finally, the total BMF corrections for D1S and D1M functionals are shown in Fig. 6.5 (g,h).

6.3.2 Comparison with experimental masses

Having analyzed the global energy gains from the different BMF approaches, we now turn to the question of whether the implemented BMF corrections improve theoretical

D1S	E [MeV]	S_{2n} [MeV]	S_{2p} [MeV]	D1M	E [MeV]	S_{2n} [MeV]	S_{2p} [MeV]
HFB	3.53	0.98	1.15	HFB	5.29	0.89	0.99
PN-VAP	2.62	1.10	1.11	PN-VAP	3.14	1.03	0.96
PNAMP	3.75	0.98	1.00	PNAMP	1.79	0.89	0.86
GCM	4.45	0.95	1.00	GCM	2.17	0.85	0.87

Table 6.1: Root-mean-square deviations from the experimental results of AME12 for total binding energies E, as well as two-neutron S_{2n} and two-proton S_{2p} separation energies of the considered methods for D1S (left side), and D1M (right side).

description of the known nuclei. The baseline HFB calculation, as well as each step of our BMF correction are shown in Fig. 6.6 and compared to the experimentally known masses from AME12 [13, 14]. The Table 6.1 quantifies the results, and presents the rms values for g.s. binding energies, as well as two-neutron, and two-proton separation energies.

As was already mentioned in Sec. 5.3, the elder Gogny D1S parametrization has a couple of major drawbacks, which are, as can be seen in Fig. 6.6, inherited by the BMF corrections as well. First, the apparent overbinding of both HFB and BMF methods

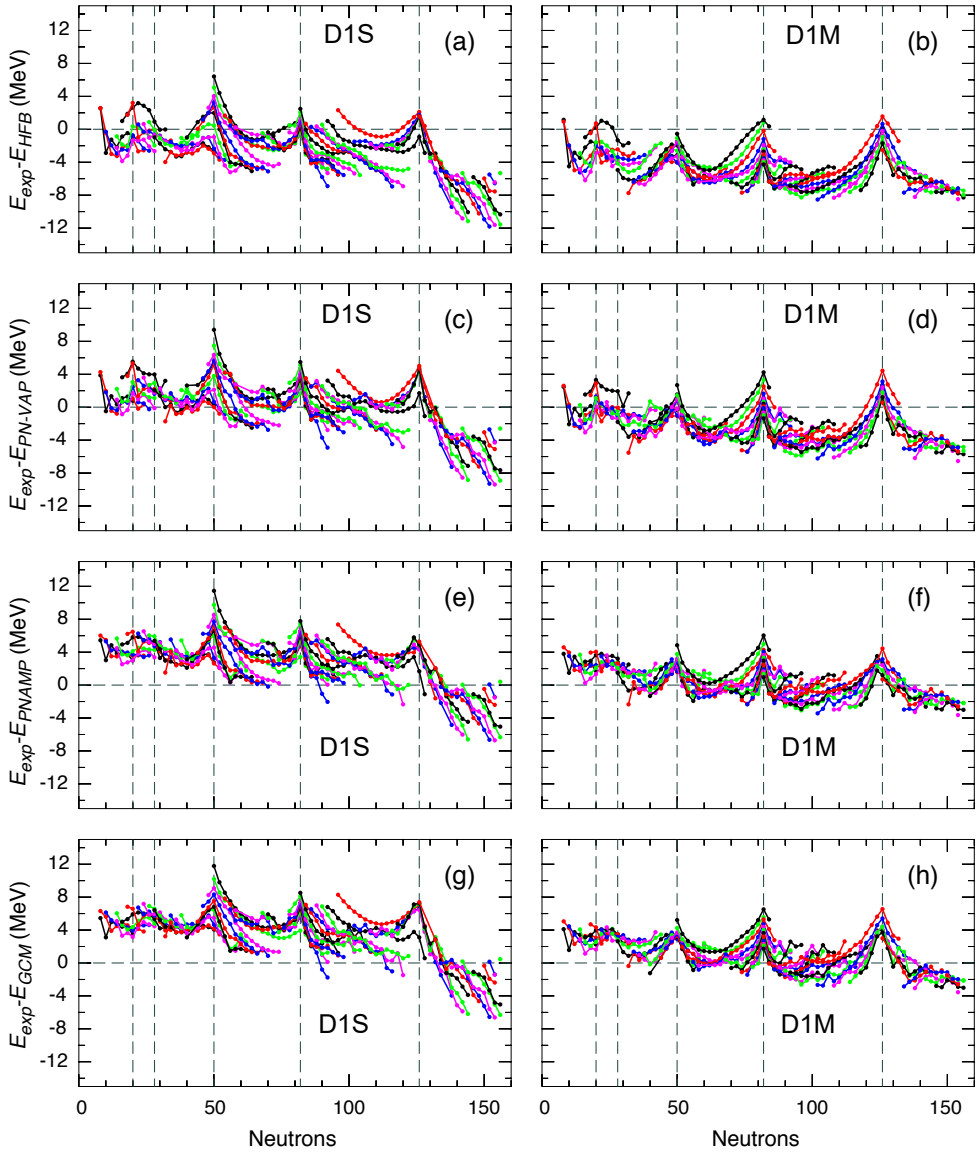

Fig. 6.6: Comparison of the calculated binding energies with (a,b) HFB, (c,d) PN-VAP, (e,f) PNAMP, and (g,h) GCM approaches to experimental masses of AME12 compilations both for (left) D1S, and (right) D1M Gogny functionals as a function of neutrons. Isotopes are interconnected with solid lines. Neutron magic numbers are marked with vertical dashed lines. Adapted from Ref. [270].

at the shell closures are observed, which results in the appearance of the pronounced peaks at $N = 50, 82$, and 126. Although that the BMF corrections tend to soften these peaks somewhat, the reduction is not sufficient to flatten the experimental residuals and bring the rms value below 2.6 MeV for any of the approaches. Another drawback, is the previously discussed systematic underbinding of the neutron-rich isotopes due to the poorly implemented symmetry energy (see Sec. 5.3 for discussion). Finally, the parameters of the D1S interaction were fitted without consideration of additional BMF corrections, therefore a large fraction of the nuclei is found to be overbound already at the mean-fiend level. Going beyond the mean-field will naturally lead to an overall shift of the rms values upwards. This fact is well-seen by studying the D1S part of the Table 6.1 for binding energies, where, apart from PN-VAP, the inclusion of additional BMF correlations only raises the rms up to 4.45 MeV when all BMF correlations are taken in account.

The situation with the newer Gogny D1M parametrization is a bit different. The functional was refitted to a larger set of experimental data with the aim to account for the drawbacks of D1S interaction. Some BMF correlations obtained with 5DCH approach [154, 199] were also included in the fitting protocol, resulting in the rms deviation of 0.798 MeV. Obviously, our BMF calculation with D1M functional cannot achieve such a good agreement with the experimental data due to several major differences in the two approaches. Firstly, the 5DCH includes triaxiality as an additional degree of freedom during the calculations. Secondly, the 5DCH do not incorporate exact quantum number projections, and the included quadrupole corrections can be viewed as a GOA approximation of the our GCM method [59]. Moreover, the 5DCH quadrupole corrections are not strictly variational [270], and some corrections for the closed-shell nuclei had to be manually neglected [154]. Lastly, on top of 5DCH corrections additional arbitrary energy adjustment due to the lack of convergence were made. However, we have previously disproved such adopted corrections in Sec. 5.4. The Fig. 6.6 (b,d,f,h) shows the D1M calculations with and without our BMF corrections. First of all, the systematic underbinding of neutron-rich nuclei is corrected. Although that the inclusion of the BMF effects tends to somewhat flatten the differences with the experimental data, the presence of strong Shell Effects is still evident by the well-pronounced peaks at the neutron-shell closures. As mentioned before, the fitting protocol of D1M interaction left some room for the BMF effects, resulting in the fact that the HFB calculations (Fig. 6.6 (b)) are underbound by 5.29 MeV on average. Including the PN-VAP and PNAMP correlations (Fig. 6.6 (d,f)) reduced the rms value to 3.14 MeV and 1.79 MeV, respectively. However, due to the reasons discussed previously, adding also configuration mixing raises the rms to 2.17 MeV.

Of course, considering only the rms values is misleading. First of all, neither D1S nor D1M were fitted to incorporate the BMF corrections considered in this work. Moreover, the rms mirrors only the global trend in comparing the theoretical results to the experimental ones, and do not represent the improvements in local regions of the nuclear chart. For example, as can be seen by comparing Fig. 6.6 (b) to Fig. 6.6 (h), the GCM methods significantly reduces the spread in the $N \leq 28$ region.

Similarly to the recently discussed figure, the Fig. 6.7 shows the analogous binding energy differences, but as a function of the proton number. The nuclei of the same isotonic chains are connected with lines. The Shell Effects are much less evident here, however, just like the case with isotopic chains, the greatest improvement from the

inclusion of BMF effects is observed in the region of light nuclei around $Z \approx 20$ with both Gogny parametrizations, while no noticeable reduction of the residual spread can be observed for heavier nuclei. Nevertheless, the mentioned problem with the symmetry energy is also observed in the D1S plots by the systematic drift of the binding energies for almost all isotonic chains in Fig. 6.7 (a,c,e,g). However, comparing D1S and D1M calculations in Fig. 6.6 and Fig. 6.7, we conclude that both the symmetry energy issue, as well as systematic overbinding can be resolved by refitting the functional. On the other hand, despite some reduction on the lower mass region of the nuclear chart, the strong Shell Effects are not smeared out by the BMF corrections.

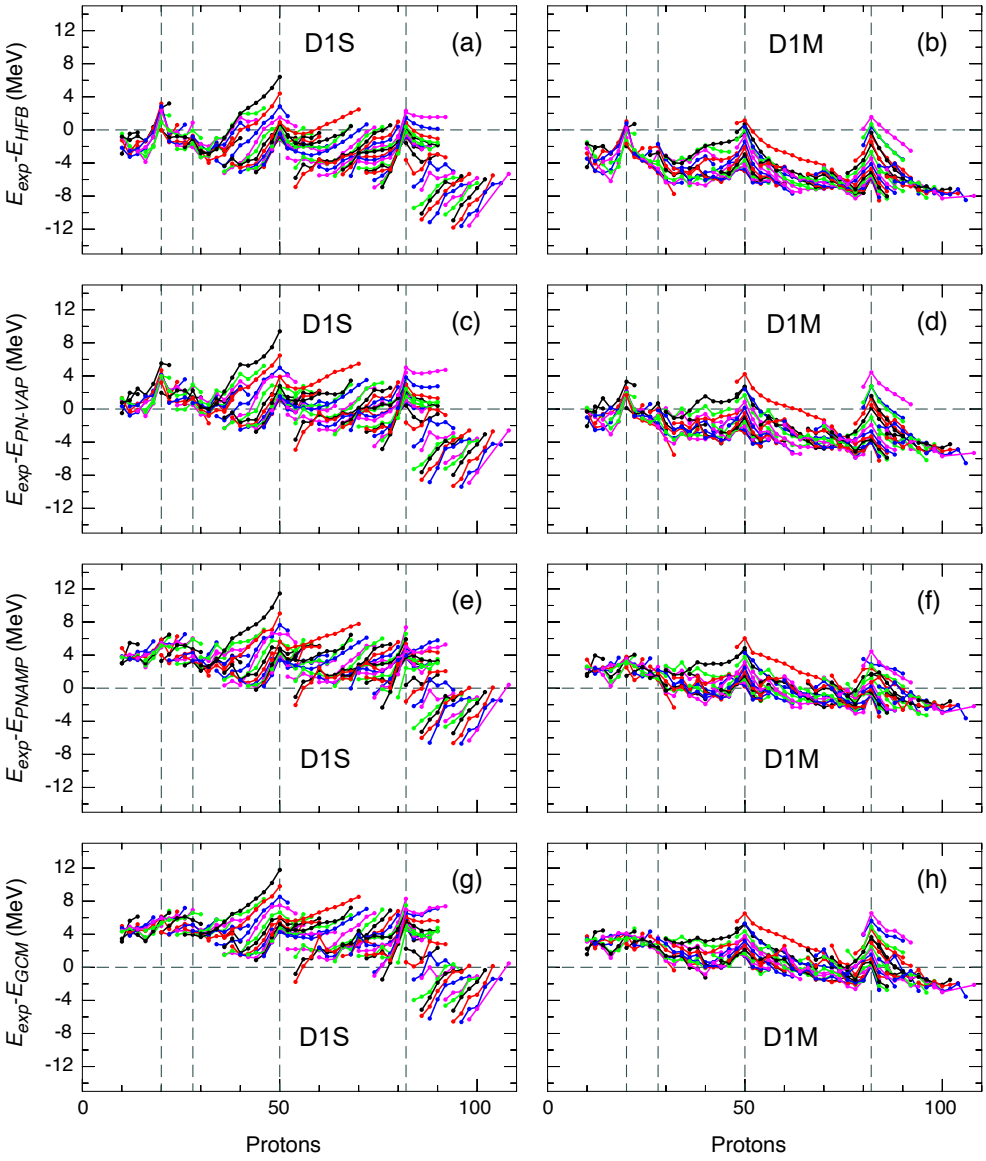

Fig. 6.7: Same as Fig. 6.6, but as a function of protons. Isotones are interconnected with solid lines. Vertical dashed lines mark the proton magic numbers. Adapted from Ref. [270].

6.3.3 Two-particle separation energies and shell gaps

To gain more insight into the impact of the implemented BMF corrections, we also study the derivative values of the total binding energies, such as two-neutron and two-proton separation energies, defined as $S_{2n}(Z,N) \equiv E(Z,N-2) - E(Z,N)$ and $S_{2p}(Z,N) \equiv E(Z-2,N) - E(Z,N)$, respectively. These quantities are more sensitive to the Shell Effects than the binding energies, but the pairing effects are less pronounced than in the one-particle separation energies. Besides this, the separation energies are also of a greater astrophysical interest, since they directly enter into calculations of reaction rates and the Q–values. The S_{2n} and S_{2p} values for both Gogny D1S and D1M are shown

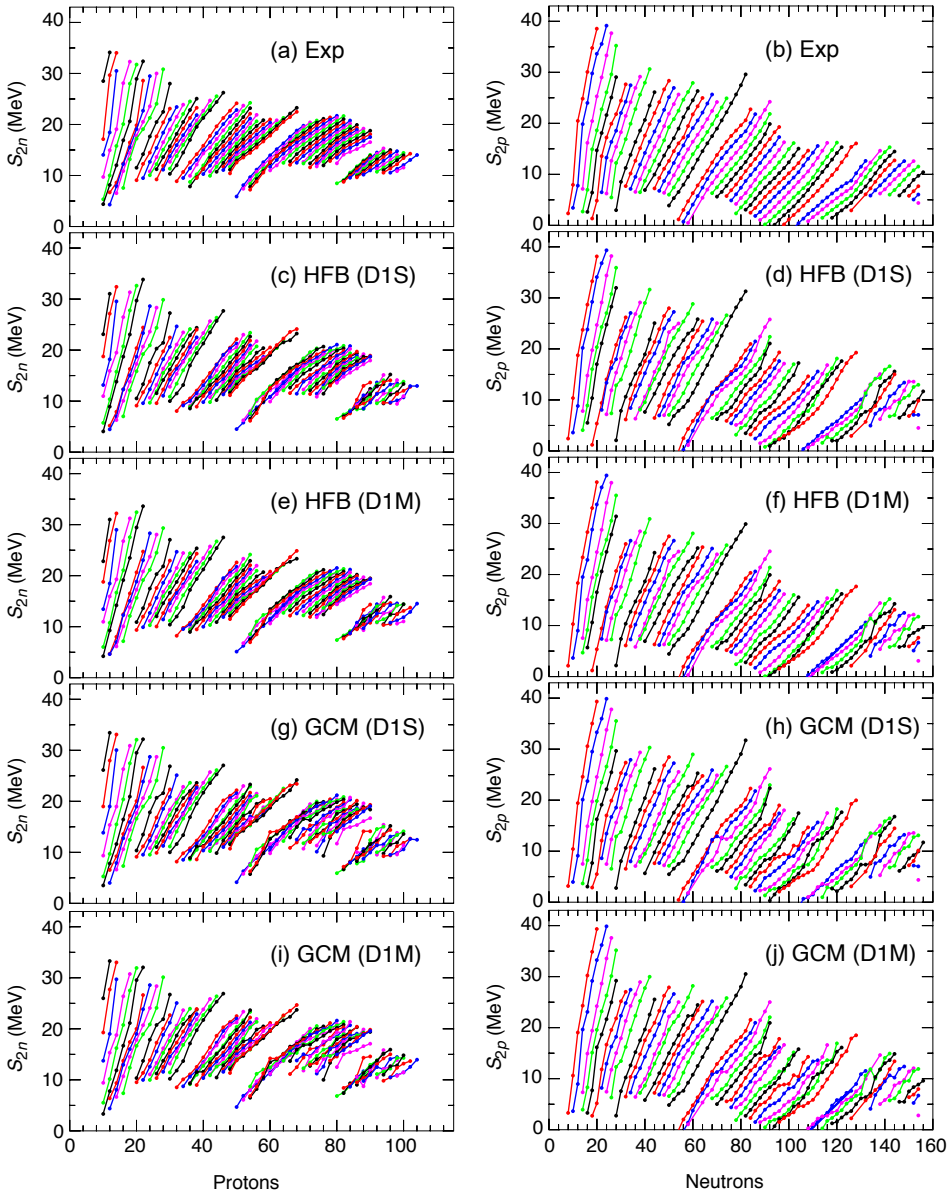

Fig. 6.8: S_{2n} (left side) and S_{2p} (right side) values for experimental data and theoretical calculations. See text and plot labels. Adapted from Ref. [270].

in Fig. 6.8, while the quantitative result can be found in Table 6.1. All the generic features of the empirical separation energies are found present in all of the theoretical approaches. Moreover, compared to the total binding energies, the global rms values are significatly reduced and are found to be of $\sim$1 MeV order (Table 6.1). Nevertheless, a closer inspection of the particular isotopic and isotonic chains reveals some troublesome behaviour of the calculatations. For example, the curves of empirical separation energies, Fig. 6.8 (a,b), are found to be much smoother when compared to results of theoretical calculations in Fig. 6.8 (c-j). More speficifically, already on the mean-field level, Fig. 6.8 (c-f), the plotted separation energy curves are more fractured, and the inclusion of the BMF corrections, shown in Fig. 6.8 (g-j), seems to amplify this feature with more inter-crossing of the curves starting to appear. This shortcoming may be due to the convergence issues of HFB results discussed in Sec. 5.3, or due to the insuficiently large SHO basis used for BMF corrections (see minor numerical noise appearing in Fig. 6.3). Furthermore, the lack of higher multipole degrees of freedom in our calculations may also contribute to this issue. However, it should be noticed, that despite an inclusion of triaxiality into the 5DCH calculation [199], the BMF corrections obtained there are found to be smaller than from the present SCCM method. Besides this, the much smoother separation energies reported in Refs. [245, 273] might be due to the implementation of GOA approximations in the configuration-mixing calculations. Therefore it remains to be seen whether a greater degree of convergence and additional degrees of freedom in the BMF calculations will improve the smoothness of our theoretical results.

As mean-field description of the nuclei in the direct vicinity to the shell closures appears to be quite challenging for the current models [146] (see also Chap. 7.4) and the inclusion of the BMF effects is reported to reduce the exaggerated shell quenching of HFB approach [199, 273], we briefly study the impact on the neutron and proton shell

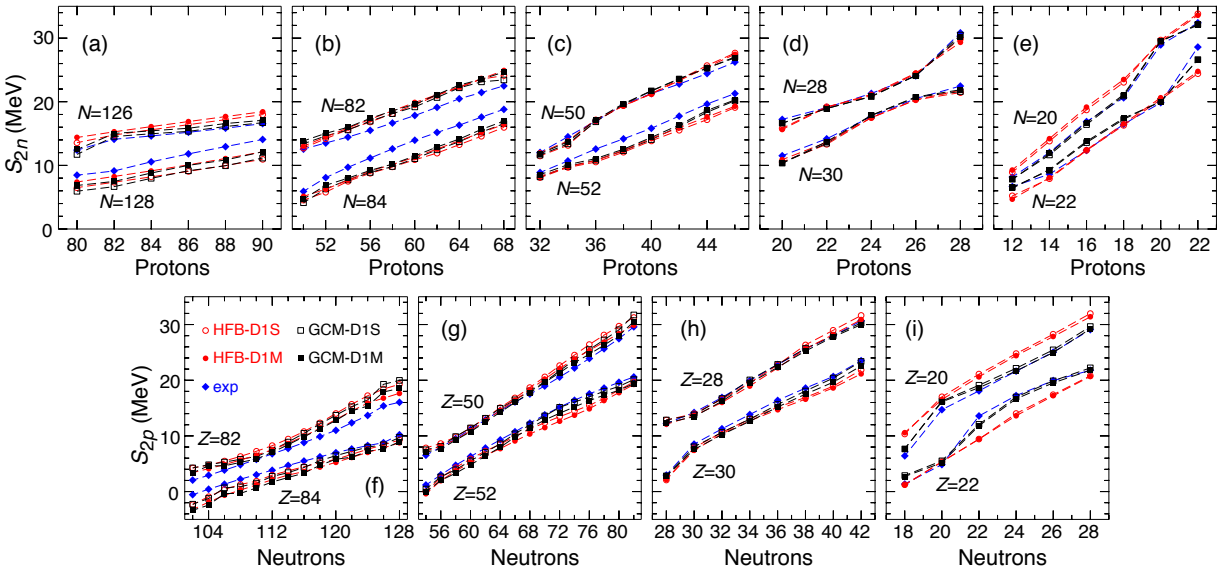

Fig. 6.9: Experimental and calculated (a-e) S_{2n}, and (f-i) S_{2p} values of the (a) $N = 126$, (b) $N = 82$, (c) $N = 50$, (d) $N = 28$, and (e) $N = 20$ neutron shell gaps; as well as (f) $Z = 82$, (g) $Z = 50$, (h) $Z = 28$, and (i) $Z = 20$ proton shell gaps. Adapted from Ref. [270].

gaps from the inclusion of the BMF methods. The Fig. 6.9 shows direct comparison of the shell gaps extracted from experimental data, as well as the obtained from theoretical approaches. As can be noticed, the HFB calculations tend to overpredict the shell gaps in most of he cases for both D1S and D1M parametrizations. The additions of the BMF corrections brings the shell gaps somewhat down in all chains, with the largest reduction found at $N = 20$, as well as $Z = 50$ and 20 magic numbers, shown in Fig. 6.9 (e,g,i). However, particularly for the heavier chains, the inclusion of the BMF effects at this level is not sufficient to the reproduce the experimental results.

6.3.4 2_1^+–excitation energies and comparison

Since the GCM approach allows us to calculate the excitation spectrum of the nuclei on the same footing as other discussed observables, we extend our BMF survey to also analyze the systematics of first-excited states in doubly even nuclei and compare the theoretical energies to the global experimental data compilation of Ref. [287]. In this section we calculate the energy of the $J = 2$ first-excited state within the SCCM framework (Sec. 4.2.4) and extract the 2_1^+ excitation energy according to Eq. (6.4). Similar studies were performed with Skyrme SLy4 interaction with the GOA approxiamtion [280], and

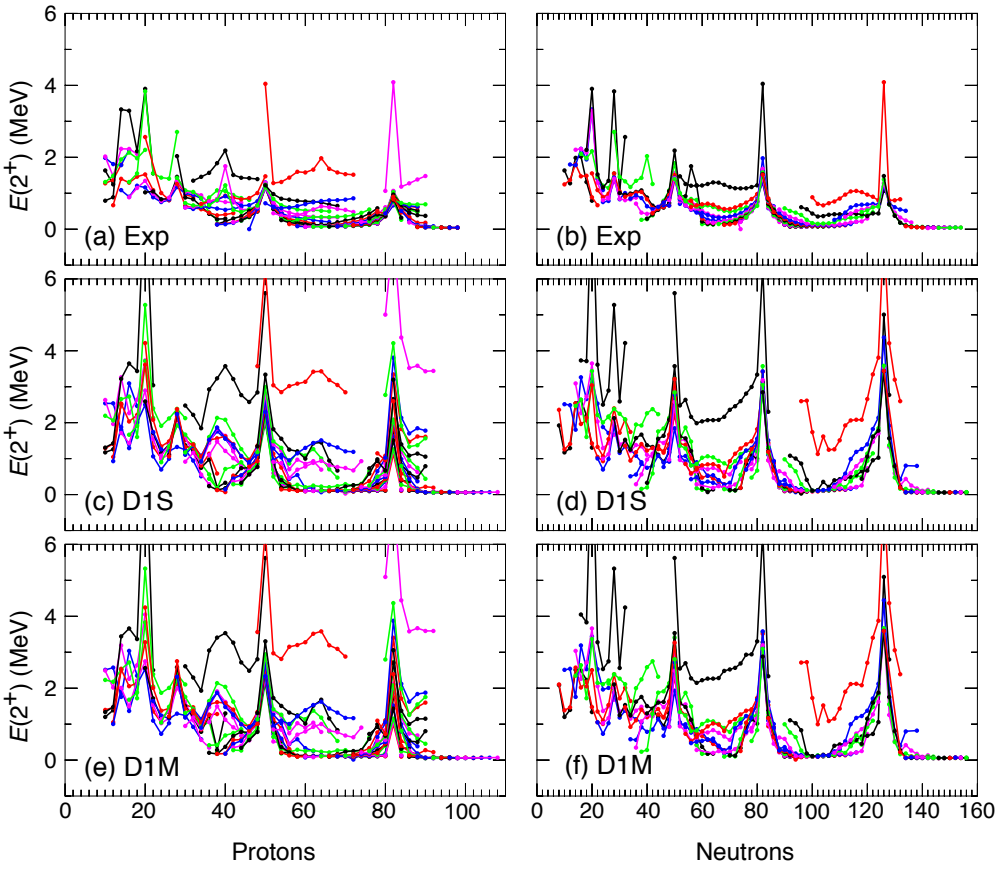

Fig. 6.10: The 2_1^+ excitation energies from (a,b) experimental compilation in Ref. [287], as well as present GCM calculation with (c,d) D1S, and (e,f) D1M Gogny functional. Nuclei of the same isotonic (left side), and isotopic (right side) chains are connected with solid lines. Adapted from Ref. [270].

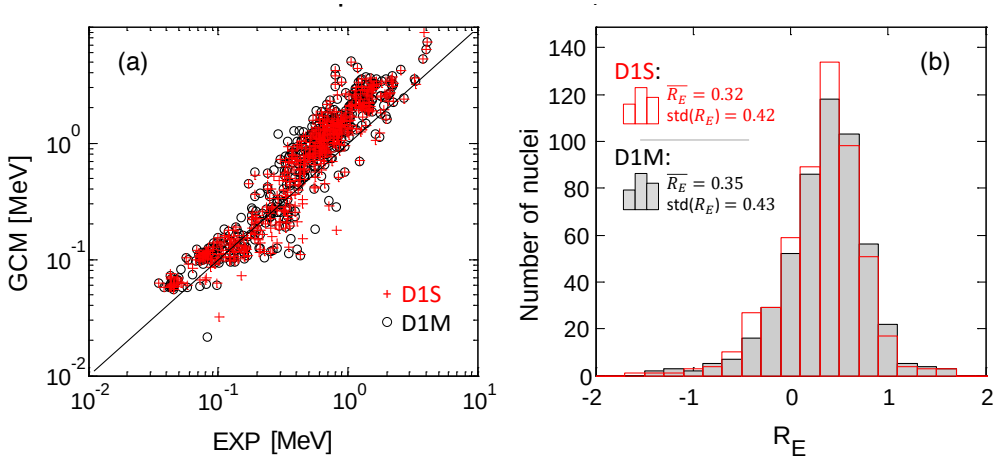

Fig. 6.11: (a) Scatter plot of GCM 2_1^+ excitation energies plotted against experimental ones from Ref. [287] for both D1S (red crosses), and D1M (black circles); (b) Logarithmic errors R_E for D1S (unfilled red), and D1M (shaded black) histograms. Average value and its standard deviations are also quoted. Adapted from Ref. [270].

using Gogny D1S functional withing 5DCH framework [199, 288]. The Fig. 6.10 shows our results of 2_1^+ energies compared to experimental data, while a direct comparison to the other theoretical surveys mentioned earlier is available in Ref. [270]. First of all, as can be seen in Fig. 6.10 (c,d,e,f), both D1S and D1M calculations have almost identical results for 2_1^+ energies, despite differing substantially in their masses predictions. Moreover, both experimental and theoretical graphs possess similar global trends with the sharp excitation energy peaks occurring at doubly-magic nuclei, while gradually decreasing in between the shell closures. Besides this, both magic isotonic and isotopic chains are energetically elevated above the rest of the neighboring chains. However, the theoretical results are found to be less smooth than their experimental counterparts, as well as turn out to be slightly overestimated. The latter fact is particularly well observed on the scatter plot in Fig. 6.11 (a), where a direct comparison of calculations against experimental data is shown by plotting the computed D1S and D1M excitation energies as a function of the corresponding empirical values. In order to gain more quantitative insight into this matter, we also indicate the logarithmic error R_E of the calculations, which is defined as

$$R_E = \ln\left[E(2_1^+)_{\rm th}/E(2_1^+)_{\rm exp}\right]. \tag{6.5}$$

Histograms of logarithmic error R_E for the considered sets of 534 even-even nuclei with D1S and D1M parametrizations are shown in Fig. 6.11 (b). Once again, the almost symmetric distributions with two Gogny interactions are fairly similar and both are shifted towards the higher values. The mean values, $\bar{R}_E$, and the corresponding standard deviations, $\mathrm{std}(R_E) = \langle\left(R_E - \bar{R}_E\right)^2\rangle^{1/2}$, are quoted in the graph and are found to be very similar to the ones obtained in the Skyrme SLy4 survey [280]. The obvious tendency to overestimate the 2_1^+ excitation energies is due to the variation space itself, which favors the ground state configuration and generally distorts the excitation spectra [270]. Another explanation may be that the generated wave functions do not posses the correct mass for the collective motion [219]. An inclusion of additional degrees of freedom particularly relevant to the excited states, such as triaxiality, T-symmetry

breaking, or quasi particles excitations, may significantly reduce the discrepancy with the experiment [270, 280]. In addition, the excitation spectra should also be considered in the fitting protocol of any future EDF to achieve the best possible accuracy of such calculations.

6.4 Summary and outlook

We have carried out a large-scale BMF calculation of doubly even nuclei using both D1S and D1M Gogny EDFs. In particular, we have systematically analyzed the calculated BMF correction energies resulting from successive implementations of particle-number projection, and angular-momentum restoration techniques, as well as the axial quadrupole configuration mixing within the GCM framework without the popular GOA approximation. In order to achieve the best possible convergence of the observables of the one hand, and reduce the computational effort on the other hand, we have performed the mean-field calculations in a relatively large $N_{OS} = 19$ harmonic oscillator basis, and augmented the results with the beyond-mean-field corrections obtained in a reduced $N_{OS} = 11$ basis. Before carrying out the global calculation, we have ensured that splitting the computation procedure into two parts with different SHO basis dimensions according to Eq. (6.1) does not compromise the overall quality of the results. Moreover, as was already thoroughly discussed in Chap. 5, such differential quantities as particle-separation energies, are found to be much less dependent on the basis dimension. Despite yielding noticeably different total binding energies on the HFB level, both D1S and D1M functionals produce very similar values of BMF correlation energies. Concerning the elder D1S parametrization, we have once again confirmed the drawback, already discussed in detail in Sec. 5.3, regarding the implementation of symmetry energy in this functional, which was corrected in the newer D1M interaction. Despite that pronounced Shell Effects were found in both of the Gogny parametrizations on the HFB level, the inclusion of rotational and vibrational corrections beyond the static mean-field by the SCCM approach tend to somewhat wash out the parabolic deviations from the experimental values. However, the reduction of the Shell Effects are not sufficient to significantly correct this observed pattern.

The extracted two-neutron and two-proton separation energies showed a much greater degree of compliance to the empirical values. Nevertheless, there are still some problems with calculated S_{2n} and S_{2p} energies, such as the lack of their smoothness along the separate isotonic and isotopic chains, as well as the crisscrossing of the separation energies between the different nuclear chains. The inclusion of BMF corrections seemed to even amplify these issues slightly, which could be explained by insufficiently large working basis for the BMF calculations. Finally, most of the computed 2^+ first-excited states were found to be systematically overestimated, with very similar results for both D1S and D1M functionals.

Generally, the restricted form of the effective interaction, and the limited selection of experimental observables in the fitting procedure of the Gogny functional [245, 289] is the cause of some discrepancies with the experimental results. Certainly, a new parametrization of the Gogny interaction fitted to a larger set of observables will improve both descriptive and predictive power of the calculation. Nevertheless, not all the discussed issues can be removed by improving the functional. A particular attention must be paid to the convergence issues of the observables in the harmonic oscillator basis.

Besides this, as was the case with 2_1^+ energies, the BMF methods themselves and the resulting variational space may affect one observable more than the others. That is why extensions to the variational space by additional degrees of freedom, such as triaxiality and time-symmetry breaking, are highly desirable. Of course, the required extensive computational cost will also demand development of highly optimized programming codes, as well as availability of powerful computing facilities.

7 Self-consistent blocking for odd-A and odd-odd nuclei

With the advent of ever growing computational resources available for the nuclear physics community, the odd-A and doubly odd nuclei (later referred to as simply *odd nuclei*) are finally starting to receive the deserved attention. After all, the odd nuclei comprise three quarters of the nuclear chart, while their various properties turn to be crucial in continuing the pursued quest of nuclear physics – to develop a more reliable and universal energy density functional (EDF) that describes as many nuclear properties as possible while simultaneously reducing the number of *ad hoc* components. The ubiquitous systematics of weaker binding in the odd nuclear systems compared to the neighboring doubly even ones (or simply *even nuclei*), known as odd-even staggering (OES), has long been identified in nuclear physics [290]. The OES is instrumental in studying such collective effect as pairing correlation [59], which manifest itself in numerous different phenomena of nuclear structure [224], and is the most important feature of any EDF beyond the nuclear mean field [275]. While OES is directly connected with pairing, there may be a few other mechanisms that can contribute to it [291–294]. Besides the mass polarization and its manifestation as OES, the unpaired nucleon also induces spin and deformation polarizations, and such data, as parities and angular momenta of ground and excited states, their excitation energies, charge radii, quadrupole and other multipole nuclear deformations, provide the essential information about the underlying shell structure of odd nuclei. A better understanding of the subtle quantum mechanical effects governing the nuclear structure of these nuclei is also indispensable for stellar nucleosynthesis calculations [295, 296], where questions of stability near the drip lines [297], and in the region of super-heavy nuclei [298–300], as well as proper description of dynamical evolution in the nuclei undergoing fission cycling [301, 302] are of paramount interest for nuclear astrophysics.

7.1 Introduction

A self-consistent description of the spin-polarized ($J > 0$) odd nuclei breaks the time-reversal symmetry of the HFB states. This makes their study more involved in different aspects than when dealing with the even nuclei. In case of the Gogny EDF, the density matrix ρ and the pairing tensor κ (*cf.* Sec. 4.1.2) of the odd nucleus violate T-symmetry [59]. The associated Hartree-Fock and pairing fields obtain both T-even and T-odd components. For even-even nuclei the T-odd terms intricately vanish in the nuclear ground state (g.s.) calculations of $J^\pi = 0^+$ configurations, and therefore can be disregarded in numerical computations. However, for odd nuclei, the T-symmetry is internally broken, and the T-odd fields have to be treated explicitly in the calcula-

tions [146, 303, 304]. This fact lifts the two-fold Kramer's degeneracy of the HFB quasiparticles (q.p.) states [59], thereby at least doubling the computational effort already in this aspect [305]. Moreover, a fully self-consistent variational calculation for odd nuclei usually requires to block multiple low-lying q.p. states separately to later identify the configuration leading to the lowest g.s. energy solution [170], thereby making the calculation scheme even more sophisticated and time-consuming (see Sec. 7.2). Because of the heavy computational burden, most of the recent calculations either ignored the T-odd fields completely [294, 306], or involved approximative blocking techniques while keeping the benefits of time-reversal symmetry. One of the most successful examples of such approaches is the so-called equal filling approximation (EFA), that was implemented for relativistic mean-field [307], Skyrme [304, 308], and Gogny [309, 310] functionals. However, since EFA is filling the pair of time-conjugated states with equal occupation probabilities, such intricate imprints of pairing as the extracted OES can miss the subtle effects of T-odd fields. Despite of the recently renewed attention to the T-odd fields, many aspects of their impact are still being investigated. The performed studies of the T-odd fields within the framework of relativistic mean field [311–313], as well as non-relativistic approaches with Skyrme [304, 314–320] and Gogny [310, 321] functionals, indicate various levels of contribution to the ground state energies and spectra, as the role of T-odd fields is naturally model dependent.

In this chapter we present the technical aspects of exact blocking calculations both for even-Z and odd-Z chains, and compare the obtained results with the widely used perturbative quasiparticle addition (PQPA) method [294, 322]. We analyse in detail a representative sample of isotopic chains from $Z = 23$ up to $Z = 91$ with a particular focus on the $Z = 48 - 52$ region, which is of increased interest for nucleosynthesis calculatations in various astrophysical environments [323–326]. We also discuss global trends and systematics of the calculated pairing gaps across the whole nuclear chart from $Z = 8$ and up to $Z = 134$.

7.2 Details of T–symmetry breaking calculation

The results of this chapter were obtained with the same HFBAXIAL-code [229, 281] that was used previously in Chap. 5 for calculations of even nuclei, as well as its more general version, the ATB- code [310, 327], for self-consistent calculations with exact blocking implementation with T-odd fields explicitely taken into account. Both codes are based on the HFB approach with Gogny effective interaction to expand the many-body wave function (w.f.) in the configuration space of harmonic oscillators. The basis states are cylindrically symmetric (and chosen of equal length in both directions), thus the axial symmetry of the nuclear wave function is preserved during the calculation. The implemented block structure of the Bogolyubov transformation matrices U and V (defined in Eq. 4.2) allows *no* proton-neutron mixing, permitting us to label q.p. states with a definite isospin, t_z. Moreover, the utilized block structure ensures that the projection of the angular momentum along the axial symmetry axis, $K = J_{\|}$, is a good quantum number. The main consequence is that the different K-configurations are automatically orthogonal to each other. However, the K and $-K$ q.p. states must be included in the same block, as they are coupled by the pairing HFB field [310]. Despite that parity is, in principle, not conserved in the calculation, it usually remains to be a good symmetry of the system, therefore allowing us in *most* cases to label the proton

and neutron q.p. states with K^π tag.

The starting configuration is generated with the T-even HFBAXIAL-code. This initial fully paired w.f. can explicitly be written in its BCS form in terms of the canonical s.p. basis $a_p, a_p^\dagger$ as

$$|\Phi_e\rangle = \prod_{p>1} (u_p + v_p a_p^\dagger a_{-p}^\dagger)\,|-\rangle\,. \tag{7.1}$$

The occupation probabilities u_p and v_p satisfy the condition $u_p^2 + v_p^2 = 1$. The canonical s.p. operators are related to the working s.p. basis, as well as to the U and V matrices, by the Bloch-Messiah theorem [59]. From Eq. (7.1) it is obvious that the seed w.f. $|\Phi_e\rangle$ is a linear superposition of Slater determinants with even number of particles (*i.e.* even number parity [328]), where the particle a_p and its time-conjugate partner a_{-p} are fully paired. Applying the variational principle, the g.s. of $|\Phi_e\rangle$ is then sought with constraint to yield the correct odd number of protons (neutrons) as an expectation value, *i.e.* $\langle\Phi_e^0|\hat{Z}(\hat{N})|\Phi_e^0\rangle = Z(N)$, where $|\Phi_e^0\rangle$ is a converged g.s. wave function.

In the next step, we identify 8 lowest-lying q.p. excitations for several quadrupole deformations that correspond to one global and *up to* two local energy minima. As illustrated in Fig. 7.1 (a) by the example of Te_{69}, only two well-established minima were identified, corresponding to $\beta_2 = -0.14$ (oblate) and $\beta_2 = 0.27$ (prolate) quadrupole deformation. The corresponding neutron q.p. states are shown in Fig. 7.1 with $K^\pi(\xi)$ tags, where ξ is an ordinal variable to distinguish between multiple states with the identical K-values. In case of the odd-odd neutron-rich Ac_{145} nucleus, shown in Fig. 7.1 (b), the potential energy curve (PEC) is more elaborate – three minima were identified: one global at $\beta_2 = 0.25$, and two local at $\beta_2 = -0.16$, and 0.65. Although that in this particular example of Ac_{145} the two local minima are energetically well above the global minima $E_0 = -1763.48$ MeV by more than 5 MeV, this prescription allows us to systematically treat cases across the whole nuclear chart where several minima can be nearly degenerate, as in the case of Te_{69}. Some impacts of having several close-lying minima are discussed later. The 8 lowest proton *and* the same number of neutron q.p. states for Ac_{145} are depicted in Fig. 7.1 (b) for each deformation. The global energy minimum corresponding to the even number-parity solution is labeled with $E_{\text{T-even}}$, while the results of the so-called perturbative quasiparticle addition (PQPA) approximative method, described in Ref. [294], are readily extracted at this stage of calculation, and are denoted with E_{PQPA}.

Given that the level to be blocked is not known beforehand, we block one of the previously identified low-lying q.p.-states in the $|\Phi_e^0\rangle$ configuration. The obtained set of blocked w.f. can formally be written as

$$|\Phi_{\mu_i}\rangle = \beta_{\mu_i}^\dagger \left|\Phi_e^0\right\rangle, \tag{7.2}$$

where $\mu_i = \{t_z, K^\pi(\xi)\}$, $i = 1, \ldots, 8$; or, after proper normalization, it can be recast in terms of canonical s.p. basis to

$$|\Phi_{\mu_i}\rangle = a_{\mu_i}^\dagger \prod_{p>1}^{p\neq\mu_i} (u_p + v_p a_p^\dagger a_{-p}^\dagger)\,|-\rangle\,. \tag{7.3}$$

Here clearly such w.f. is composed of superpositions of Slater determinants with odd number of particles (odd number parity), and now properly describes an odd-A nucleus.

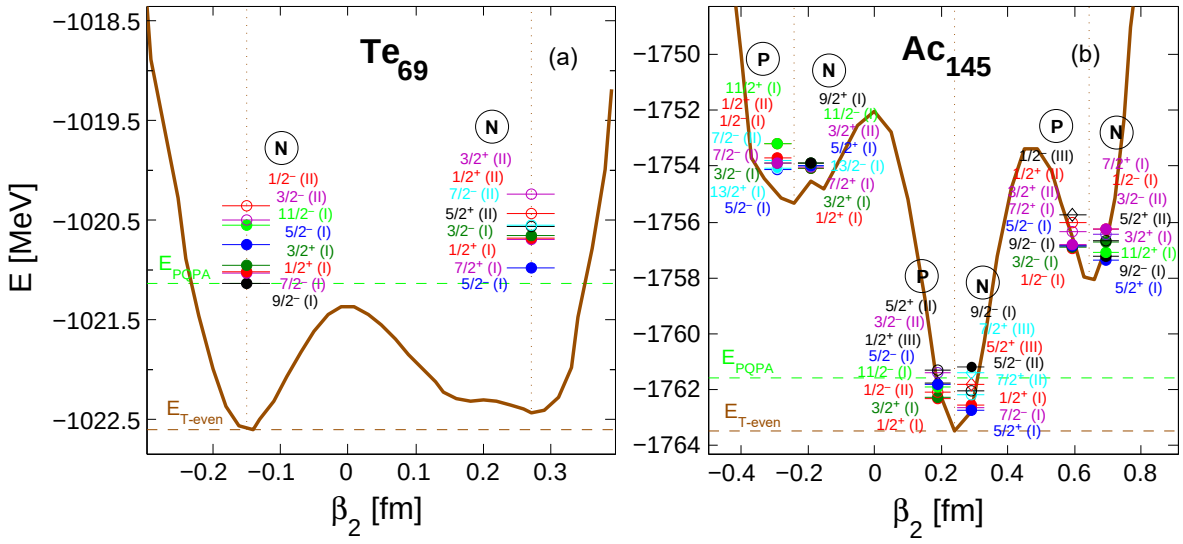

Fig. 7.1: Calculated β_2–PEC (brown solid line) of $\left|\Phi^0_e\right\rangle$ for (a) ^{69}Te, and (b) ^{145}Ac. The identified energy minima are denoted with vertical dotted lines, for which 8 lowest-lying q.p. excitations for (N)eutrons and (P)rotons with corresponding $K^\pi(\xi)$ tags are shown. The absolute $\left|\Phi^0_e\right\rangle$-minimum ($E_{\text{T-even}}$), and PQPA approximation (E_{PQPA}) are shown by dashed lines.

In practice blocking can very conveniently be carried out by swapping the appropriate columns in the U and V matrices of a fully-paired $\left|\Phi^0_e\right\rangle$ state, *i.e.*

$$\left(U_{m\mu_i}, V_{m\mu_i} \right) \leftrightarrow \left(V^*_{m\mu_i}, U^*_{m\mu_i} \right). \tag{7.4}$$

The swapping effectively converts $\beta^\dagger_{\mu_i}$ in Eq. (7.1) into β_{μ_i}, thereby re-defining the q.p. vacuum, changing the number parity, and straightforwardly going over to one-q.p. state [59]. Of course, for the case of a doubly odd nucleus, one has to block both proton *and* neutron q.p. states. In fact, the swapping of different columns can be carried out multiple times as to represent, for instance, multi-quasiparticle excitations [310].

One proceeds by re-minimizing each of the 8 blocked configurations $\{|\Phi_{\mu_i}\rangle\}$ and, following the variational principle, identifies the converged w.f. $\left|\Phi^0_{\mu_0}\right\rangle$ that results in lowest g.s. energy. Here it should be noted, that owing to the non-linear character of the self-consistent HFB equations, blocking only one lowest q.p. state is not guaranteed to converge to the lowest g.s. energy solution. In case of the doubly odd nuclei, according to our prescription, we analyze *at most* $8 \times 8 = 64$ starting configurations. In practice, however, we restrict ourselves only to $\xi \leq 2$ configurations, thereby reducing somewhat the number of required re-minimizations. In cases when $\xi > 1$, we impose an additional constraint and require orthogonality to the already blocked states with K^π-nomenclature, as to ensure a non-degenerate solution.

Several PEC profiles for a representative selection of converged blocked $\left|\Phi^0_{\mu_i}\right\rangle$ configurations for $^{67-73}$Te nuclei are shown in Fig. 7.2. These particular isotopes were chosen as examples for several reasons. One of which is to demonstrate that the converged lowest-energy $\left|\Phi^0_{\mu_0}\right\rangle$–state of ^{69}Te has $K = 7/2$, and was obtained in this particular case by blocking the *second*-to-lowest q.p. state in $\left|\Phi^0_e\right\rangle$ (*cf.* Fig. 7.1). Although that such energy

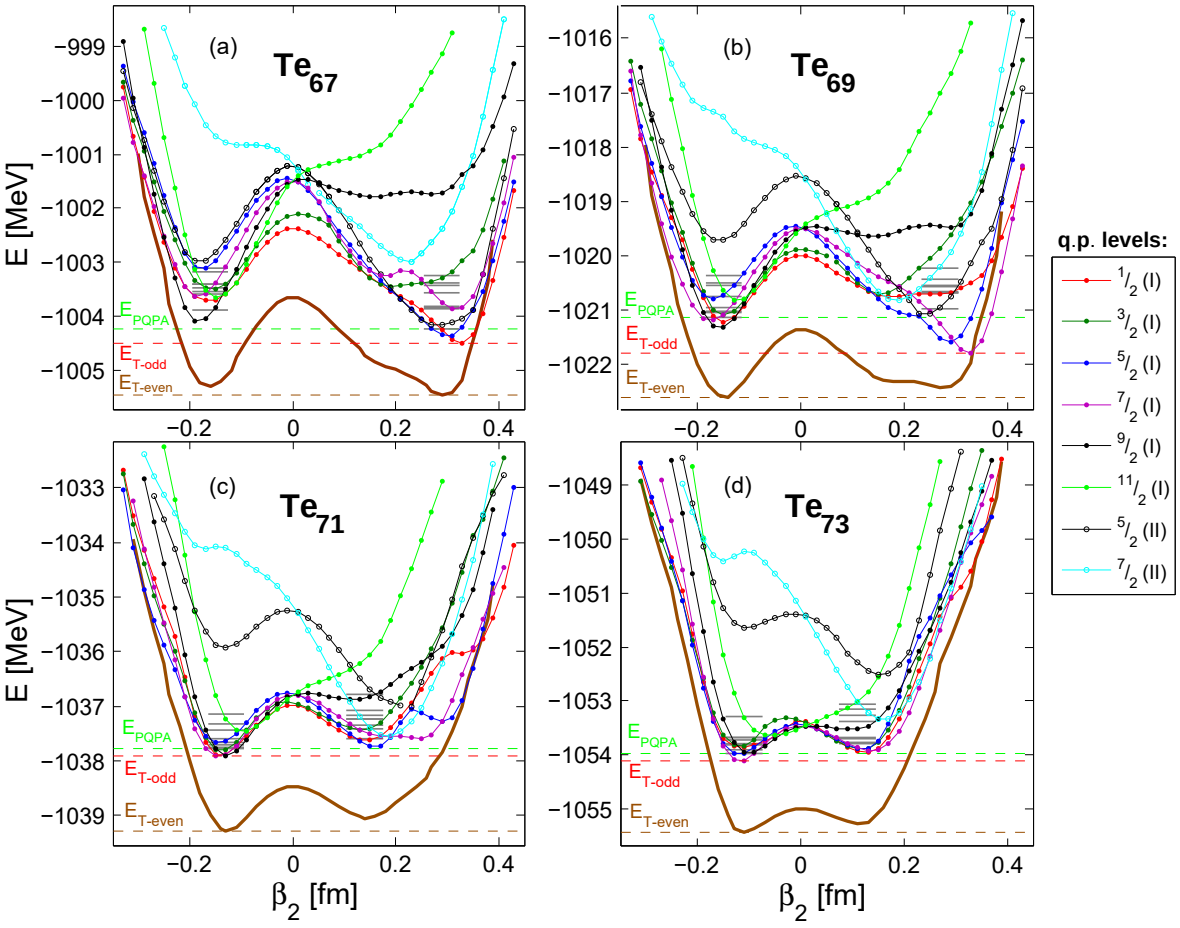

Fig. 7.2: Calculated β_2–PECs for a representative selection of blocked q.p. $|\Phi^0_{\mu_i}\rangle$–states in (a) ^{67}Te, (b) ^{69}Te, (c) ^{71}Te, and (d) ^{73}Te. The q.p. spectra of the states being blocked is denoted with gray horizontal lines. The energy of the lowest converged w.f. $|\Phi^0_{\mu_0}\rangle$ is denoted with $E_{\text{T-odd}}$, the blocked q.p. states are labeled with $K^\pi(\xi)$ tag.

gains, *i.e.* by re-minimizing multiple initial q.p. configurations, are typically of the order of a few hundreds keV, it may have a measurable impact on the profile of the pairing gaps, which we discuss later. Furthermore, as can be seen in Fig. 7.2, various converged q.p. configurations have very contrasting PEC profiles, some of which have only one β_2–minimum. This naturally leads to distinct predictions of nuclear deformations for various blocked q.p. states. Finally, such analysis is crucial for establishing the K^π properties of the calculated g.s. states.

Besides this, looking at the shape profile evolution of the $^{67-73}$Te isotopes, we can clearly see the effects of deformation polarization coming from the unpaired nucleon. Breaking the nucleon pair tend to move the energy minima of the T-odd HFB-states slightly further apart on the β_2–axis than in the fully-paired T-even reference state, on which the predictions of PQPA approach are based. That is best seen on examples of ^{67}Te and ^{69}Te, see Fig. 7.2 (a,b). In the case of the former, Fig. 7.2 (a), both schemes conclude a prolate shape, but interestingly for ^{69}Te, shown in Fig. 7.2 (b), the PQPA suggests an *oblate* global minimum with $\beta_2 = -0.14$, whereas the induced T-odd polarizations press

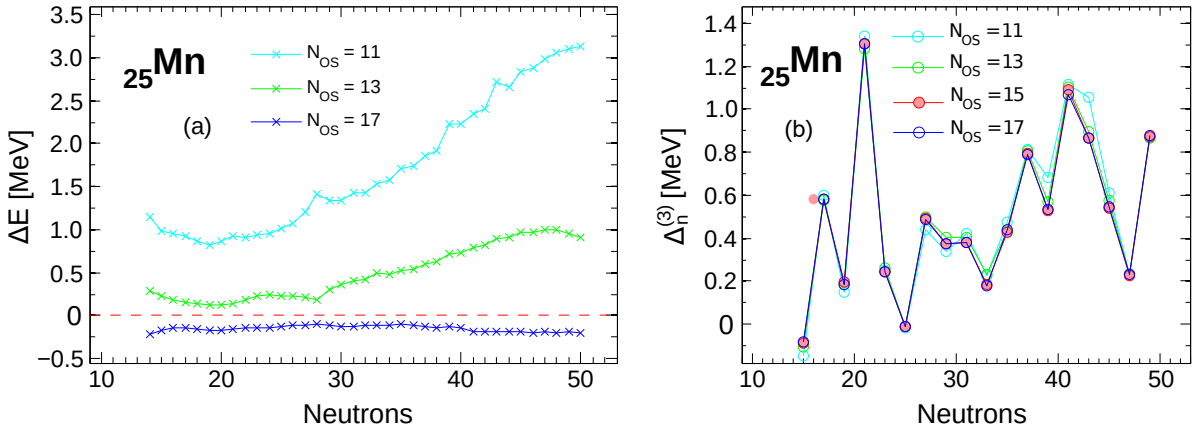

Fig. 7.3: Calculated (a) $\Delta E(N_{OS})$ and (b) $\Delta_n^{(3)}$ in working bases with various dimensions $N_{OS}$for manganese isotopes.

the PEC of the $K = 7/2$ blocked state lower at the *prolate* region of deformation, yielding a well-deformed $\beta_2 = 0.33$ solution. For Te_{71} and Te_{73}, Fig. 7.2 (c,d), both methods again agree in their deformation predictions. However, the noticeable consequence of such a discord for Te_{69} is an elevated difference between the absolute energies, E_{PQPA} and $E_{\text{T-odd}}$, when compared to the neighboring isotopes. This feature mirrors itself as a sudden negative kink in the neutron pairing gap $\Delta_n^{(3)}$ at $N = 69$ on Fig. 7.5 (c).

Following the discussion in regard to quadrupole deformations, an important remark regarding the octupole moments is in its place. Before re-minimizing the set of $\{|\Phi_{\mu_i}\rangle\}$ initial configurations, the reflection symmetry is explicitely broken by imposing a small octupole deformation $\beta_3 = 0.05$ in each of the blocked configurations, so that this self-consistent symmetry of the initial w.f. is not carried over to the subsequent w.f. iterations during the minimization procedure [59]. Many nuclei exhibit the octupole g.s. deformations, which was already shown in Gogny EDF calculations of doubly even nuclei [279, 329, 330], as well as odd-A ones [309]. Just as in case with quadrupole moment, blocking particular q.p. states results also in octupole moment fluctuations akin to the β_2–PECs already shown in Fig. 7.2. The gains in binding energies by breaking the reflection symmetry, and thereby including octupole degree of freedom, can be as high as 2 MeV if compared to the $\beta_3 = 0$ states [309].

7.3 Convergence benchmark of the results

The calculations in this analysis were carried out in a working s.p. basis comprising of $N_{OS} = 15$ major oscillator shells. The oscillator length parameter b, introduced in Sec. 5.2, was chosen adaptively for every isotope, as to ensure the lowest g.s. binding energy. As was already thoroughly discussed in Chap. 5, the calculated total binding energies, especially in the neutron-rich tail of isotopic chains, are expected to be less converged than the energies of stable nuclei, which is well-seen on, for example, Fig. 5.3. Nevertheless, studying the derivatives of the binding energies, *i.e.* such quantities as separation energies and pairing gaps, the absolute energy differences are generally expected to cancel out (*e.g.*, see Fig. 5.10). However, before proceeding to the results,

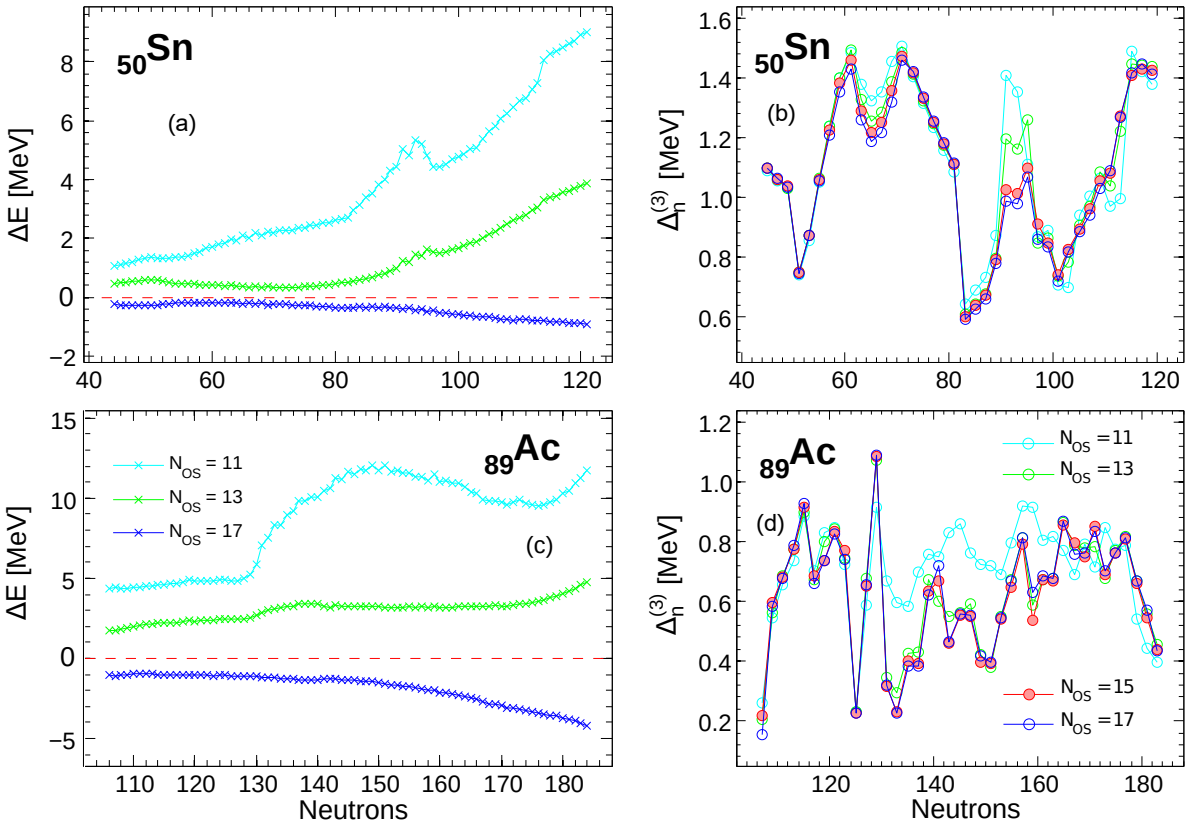

Fig. 7.4: Calculated g.s. binding energy differences $\Delta E(N_{OS})$ in various basis dimensions N_{OS} for (a) tin, and (c) actinium isotopes, as well as corresponding neutron pairing gaps $\Delta_n^{(3)}$ for (b) tin, and (d) actinium chains.

we briefly verify this aspect with respect to the OES effects to ratify our choice of the size of harmonic oscillator basis.

Left panels of Figs. 7.3 and 7.4 show the absolute binding energy differences of manganese, tin, and actinium isotopic chains calculated in $N_{OS} = 11, 13$, and 17 major oscillator basis and are compared to the reference calculations in $N_{OS} = 15$ basis. For this purpose we define the quantity

$$\Delta E(N_{OS}) \equiv E(N_{OS}) - E(15), \tag{7.5}$$

where $E(N_{OS})$ is the total binding energy calculated in a basis of N_{OS} dimension. As can be seen in Fig. 7.3 (a), $\Delta E(11)$ is reaching values slightly above 3 MeV for the case of lighter mass Mn-chain, the heavier isotopes of Sn- and Ac-chains, shown in Fig. 7.4 (a,c), are much more underconverged in $N_{OS} = 11$ basis, where $\Delta E(11)$ is reaching $\sim$8.5 MeV and $\sim$12 MeV, respectively. Of course, such quantities as two-neutron separation energies S_{2n} (defined in Eq. 5.10) and neutron pairing gaps $\Delta_n^{(3)}$ (defined in Eq. 7.6), should be insensitive to the relative shifts in terms of $\Delta E(N_{OS})$ parameter as long as they are constant across the whole isotopic chain, but the sudden changes of $\Delta E(N_{OS})$ for neighboring nuclei in Figs. 7.3 (left) and 7.4 (left) are expected to impact not only the extracted separation energies, but also the neutron pairing gaps shown in Figs. 7.3 (right) and 7.4 (right). The most pronounced $\Delta E(11)$ irregularities occur for Cd-nuclei around

$N \approx 94$, and for Ac-chain starting from $N \gtrsim 130$. It is precisely where the calculations in larger basis dimensions noticeably differ in their S_{2n} and $\Delta_n^{(3)}$ predictions. For example, the pairing gaps of $Sn_{91,93}$ calculated in $N_{OS} = 11$ basis (shown in Fig. 7.4 (b)) are over-predicted by a substantial 0.4 MeV as compared to the $N_{OS} = 15, 17$ values, and even worse for Ac-isotopes (see Fig. 7.4 (d)). As was discussed previously in Chap. 5, the $N_{OS} = 11$ basis is not large enough to adequately encapsulate the many-body w.f. of heavier nuclear systems, but even in the case of Mn-isotopes – the slight deviations for $N = 11$ calculations of $\Delta_n^{(3)}$ in Fig. 7.3 (b) are evident starting from $N \gtrsim 26$. The $\Delta E(13)$ are much smoother in all of the chains, leading to almost converged calculations of S_{2n} and $\Delta_n^{(3)}$. Finally, the $\Delta E(17)$ values are showing nearly a constant negative shift for most of the isotopes of the studied chains, resulting in virtually converged separation energies and pairing gaps on a level of hundred keV. This fact together with the comparatively low computational times in $N_{OS} = 15$ basis renders it to be a fair choice for the performed large-scale analysis.

7.4 Results of T-odd calculations

The OES effects may be analyzed with help of multiple different filters formulas: 3-point, 4-point, 5-point differences, and their variations [155, 291, 292, 331] – all of them have main objectives to quantify OES by removing the smooth contribution of the mean field energy from the remaining correlations. We follow the arguments in Refs. [291, 331] and adopt the 3-point difference formula, which is defined as

$$\begin{aligned} \Delta_n^{(3)}(N) &= \frac{1}{2}\left[\, 2E(Z,N) - E(Z,N+1) - E(Z,N-1) \,\right] \\ &= \frac{1}{2}\left[\, S_n(Z,N+1) - S_n(Z,N) \,\right], \end{aligned} \tag{7.6}$$

where N is an *odd* number of neutrons, and $S_n(Z,N)$ is the neutron separation energy, defined as

$$S_n(Z,N) \equiv E(Z,N-1) - E(Z,N). \tag{7.7}$$

The $\Delta_n^{(3)}(N)$ measure of OES has a close resemblance with the gap parameter from the BCS theory [59]. However, since BCS gap is not an observable, comparing it directly to the experimental OES is not possible. Moreover, because of the self-consistent nature of HFB calculations leads to rearrangements of q.p. levels in the neighboring nuclei, the pairing gaps have to be extracted from the particular HFB calculations directly.

7.4.1 Examination of odd-A isotopes of Cd, Sn, and Te

We start off by presenting our results for the even-Z chains of $_{48}$Cd, $_{50}$Sn, and $_{52}$Te, where only one neutron q.p. state has to be blocked. The pairing gaps of cadmiums are shown in Fig. 7.5 (a), and of tellurium isotopes are in Fig. 7.5 (c). The empirical gaps are extracted from Atomic Mass Evaluation 2012 (AME2012) mass table [13, 14], if not mentioned otherwise. On average, the 31 cadmium and 36 tellurium gaps calculated with PQPA method are larger by ~250 keV in both chains than the results from blocking calculations with T-odd fields. On the closer expection, however, there are regions in

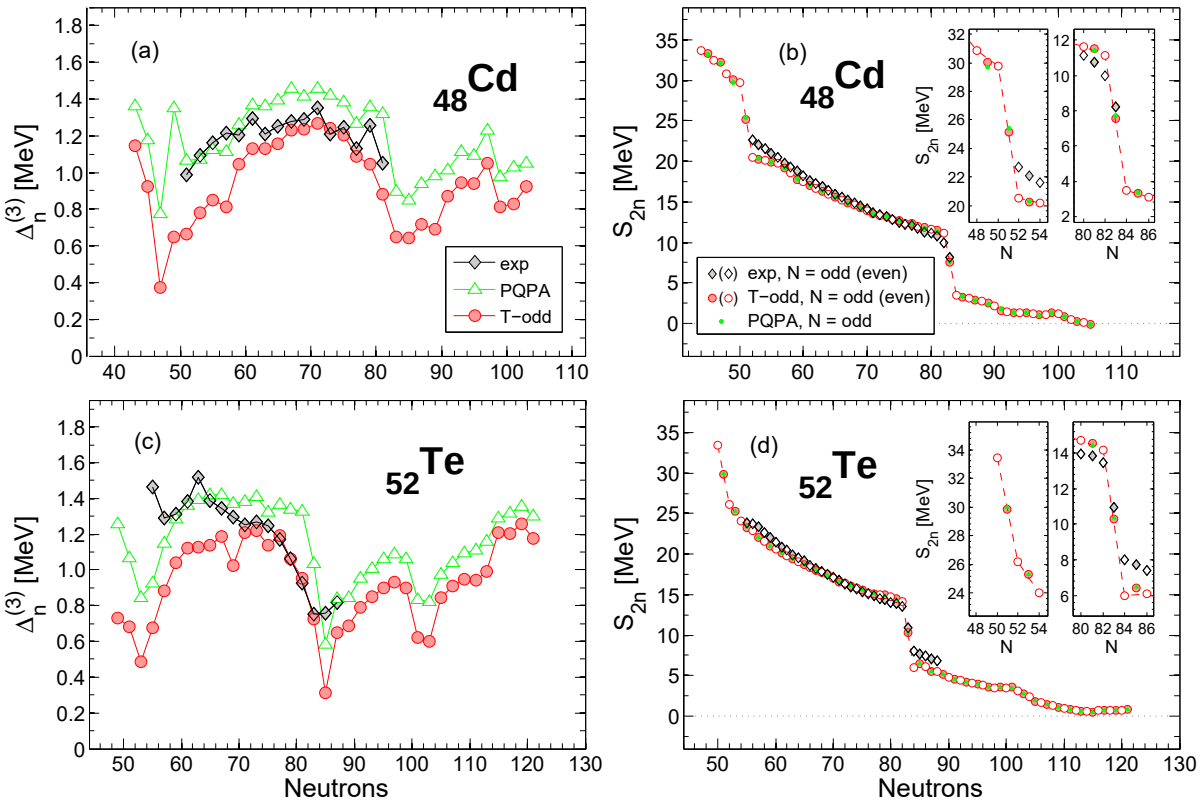

Fig. 7.5: The calculated PQPA (green) and T-odd (red) pairing gaps of (a) cadmium, and (c) tellurium isotopes. Experimental results are shown in black and are taken from AME12 and Ref. [332]. The S_{2n} are also shown for (b) cadmium, and (d) tellurium isotopes. The corresponding shells gaps are plotted in the insets.

both chains, where the theoretical approaches deviate significantly from one another. In the case of cadmium, it is the sudden kink at $N = 49$ in the perturbative calculation that is not visible in the one with T-odd fields. Unfortunately, there are no experimental data for this gap to attest or disprove this differentia. For the tellurium we observe a smaller negative kink at $N = 69$ in the blocking calculation that is not present when adding a nucleon perturbatively. The origin of this dip are the markedly distinctive quadrupole moments of the found Te_{69} ground states, as was already explained previously in Sec. 7.2. The EDF calculations agree in predicting the gap quenchings at $N = 47, 83, 99$ for Cd, and at $N = 53, 85, 101$ for Te on the quantitative level. Although that the predicted rapid decrease of the gap strength in the $N = 75 - 83$ region of Te is confirmed by the AME2012 values, the gap quenching at $N = 85$ is not present. Also the empirical dips at $N = 55$, and $N = 63$ are not reproduced in either calculations of Te nuclei.

In the context of astrophysics, however, the more important quantities are the neutron separation energies, that enter directly into calculations of *e.g.* reaction rates and Q values. We show the two-neutron separation energies S_{2n} for cadmium and tellurium isotopes in Fig. 7.5 (b) and Fig. 7.5 (d), respectively. The calculated S_{2n} values show a particularly good agreement with the experimental ones in between the $N = 50$ and $N = 82$ magic numbers, where they decrease smoothly while the $N = 50 - 82$ shell is being filled. Nonetheless, the regions in the direct vicinity of the closed shells tend to be

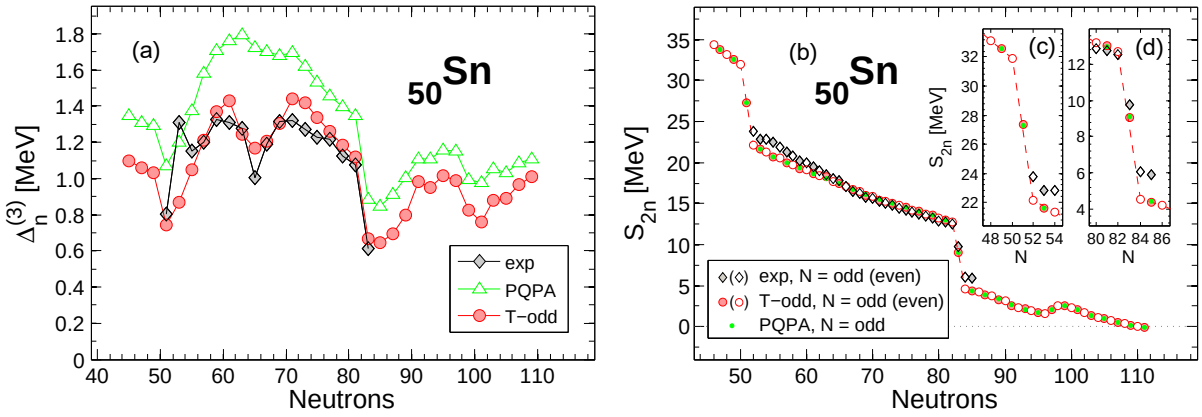

Fig. 7.6: Same as Fig. 7.5. Some experimental values are taken from Ref. [333].

more troublesome to reproduce in the mean-field approaches. As can better be seen in the inset of Fig. 7.5 (b,d), the theoretical calculations tend to significantly overpredict the shell gaps, and quite generally give a poor agreement of the S_{2n} values around the shell closures. Nevertheless, regardless of whether all the mentioned experimental details may or may not be reproduced, the theoretical results show the imprints of the shell structure for the implemented Gogny-D1S EDF.

Now we turn to the case of the semimagic $_{50}$Sn chain. Tin isotopes can be regarded as the favorites in the study of pairing properties of different EDFs [311, 334–337]. Our results are presented in Fig. 7.6, and are similar in their general trends to the cases of Cd and Te discussed before. The gaps from PQPA calculatations are on average larger by $\sim$250 keV than from the blocking calculations, while both approaches show an arched overall behavior throughout the $N = 50 - 82$ major shell: following the gap quenching at $N = 51$, the strength of the gaps gradually increase from the doubly magic $^{100}_{50}$Sn and decrease towards the shell closure with a strong gap quenching at $N = 83$. The T-odd calculations encounter a small dip at around $N = 65$, which is confirmed by the empirical results, but is almost invisible in the PQPA approach. The calculated gaps around this dip are also peculiar in the sense that, as was shown in Fig. 7.4 (b), the differences in binding energies around $N = 65$ exhibit comparatively lesser degree of convergence even in a larger $N_{OS} = 15$ basis than the calculations of other isotopes. Consequentially, one may expect to better reproduce the sharper kink of the experimental values by performing calculation in larger working basis. Another noticeable feature that is not captured by the mean-field calculations is the sudden experimental kink at $N = 53$. Despite that the total decrease of the gap at $N = 83$ is quantitatively well-replicated in the Gogny calculations, as can be seen in Fig. 7.6 (c,d), the two-neutron separation energies at the shell closure are much exaggerated, just as in the previous cases of Cd and Te.

Looking at more neutron-rich tin isotopes in Fig. 7.6 (b), where the S_{2n} drops below 3 MeV we see a eminent bulge of the separation energies rising by $\sim$1 MeV around $N = 99$. Although not so prominent in cases of cadmium and tellurium, but still distinguishable in those chains as well. The Fig. 7.7 (a) shows the mean-square radius of the density

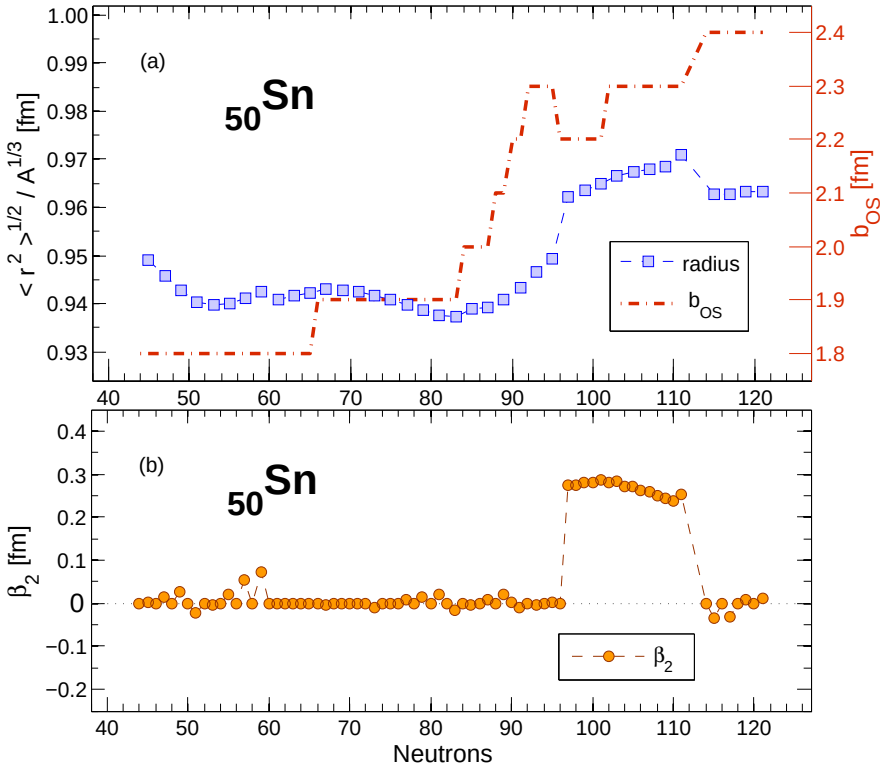

Fig. 7.7: Calculated (a) mean-squared radius of tin nuclei (left Y-axis, blue squares), as well adaptively chosen oscillator length b_{OS} of the working basis (right Y-axis, red dot-dashed line); (b) corresponding quadrupole deformation parameter β_2.

distribution $\langle r^2 \rangle^{1/2}$ on the left axis, where

$$\langle r^2 \rangle = \int \rho(\vec{r})\, \vec{r}^{\,2} dV \;/ \int \rho(\vec{r}) dV. \tag{7.8}$$

The right axis shows the adaptively chosen oscillator length parameter b_{OS}. One can see that the calculated nuclear radii expand rather abruptly for $N = 97$ nucleus, precisely at the point where the aforementioned bulge in S_{2n} is starting to build up. The radius then suddenly drops back to lower values at $N = 115$. Looking at the oscillator lengths, one sees that, despite the sudden increase of the radius in the $N = 97 - 115$ region, the optimal b_{OS} values not only stop rising, but even decrease for a couple of nuclei. The explanation for such behavior can be found by looking at the Fig. 7.7 (b), where the quadrupole deformation parameter β_2 is plotted against the neutron number. One sees that the calculations predict a sudden change from the spherical shape to a well-deformed prolate deformation of $\beta_2 \approx 0.27$ precisely for the mentioned $N = 97 - 115$ region of the isotopic chain. While accelerator facilities have yet not reached that far into the neutron- rich tail of the tin chain, all these features still remain to be validated by the experiments.

7.4.2 Analysis of odd-odd nuclei: from vanadium to protactinium

While more results of even-Z chains with exact blocking approach and Gogny D1S functional can be found in Ref. [310], we proceed our analysis with the more challenging

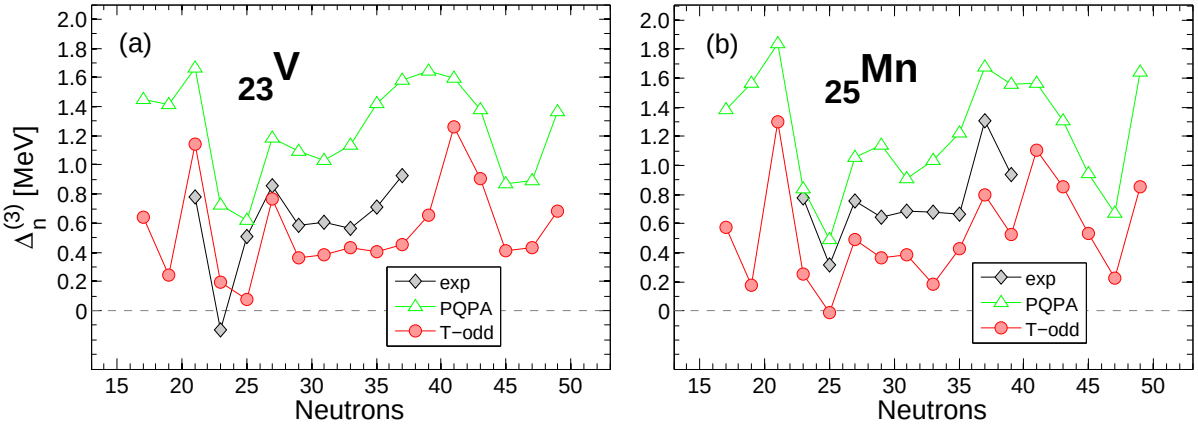

Fig. 7.8: The neutron pairing gaps obtained with PQPA method (green), and blocking approach (red), compared to experimental values (black) for (a) vanadium, and (b) manganese isotopes.

odd-Z chains. The pairing gaps for two lighter odd-Z chains from our survey, $_{23}$V and $_{25}$Mn, are plotted in the Fig. 7.8. Both PQPA and exact blocking calculations show qualitatively similar trends of the pairing gaps, that overall agree with the features of experimental results. However, the PQPA approach is seen to overestimate the $\Delta_n^{(3)}$ parameter in comparison to the 9 empirical gaps by a mean of 0.56 MeV and 0.35 MeV for vanadium and manganese, respectively. On the other hand, the blocking calculations are generally underpredicting the gaps by $\sim 100 - 300$ keV. If one directly compares the PQPA approach with the exact blocking method, the former is yielding gaps that are on average stronger by 0.69 MeV than the latter. Looking at the particular details of the $\Delta_n^{(3)}$ values, both theoretical approaches exhibit a strong decrease in the gaps strength at $N = 23$ when filling the $f_{7/2}$ subshell. While owing to an absence of experimental results at $N = 23$ this cannot be directly confirmed for manganese, this feature is present in the empirical results for vanadium. One should also note an exceptional case of negative empirical pairing gap at $N = 23$, with the only other known case up to now in the $_{31}$Ga–chain at $N = 31$ (see Ref. [224] for discussion). One can also notice that the inclusion of T-odd fields results in a more spiky gap profile than when adding the nucleon perturbatively on top of the fully-paired nucleus. This is not surprising, since the paring gaps are largely impacted by the density variations of the s.p. levels and their character near the Fermi energy [308], and blocking one of the q.p. states may lead to significant rearrangements of such levels. Besides this, the unpaired nucleon will induce deformation polarizations of the core, the effects of which will also lay imprints on the pairing gaps. All these effects, of course, are not included in the PQPA approach. We will come back to these points later.

The next two chains in our analysis are the $_{49}$In and $_{51}$Sb, shown of Fig. 7.9. Looking at the neutron gaps, Fig. 7.9 (a,b), some similarities with the previously reported results for Cd, Sn, and Te are observed. The $\Delta_n^{(3)}$ values of both chains grow after shell quenching at $N = 49$ for In, and $N = 53$ for Sb, reaching a strength of ~ 1 MeV in the middle of the shell, and sharply decrease at around $N \approx 80$ in both calculations. The perturbative addition calculations for both In– and Sb–chains show on average ~ 0.35 MeV larger gaps than the results from blocking method. However, there are some distinctive features to

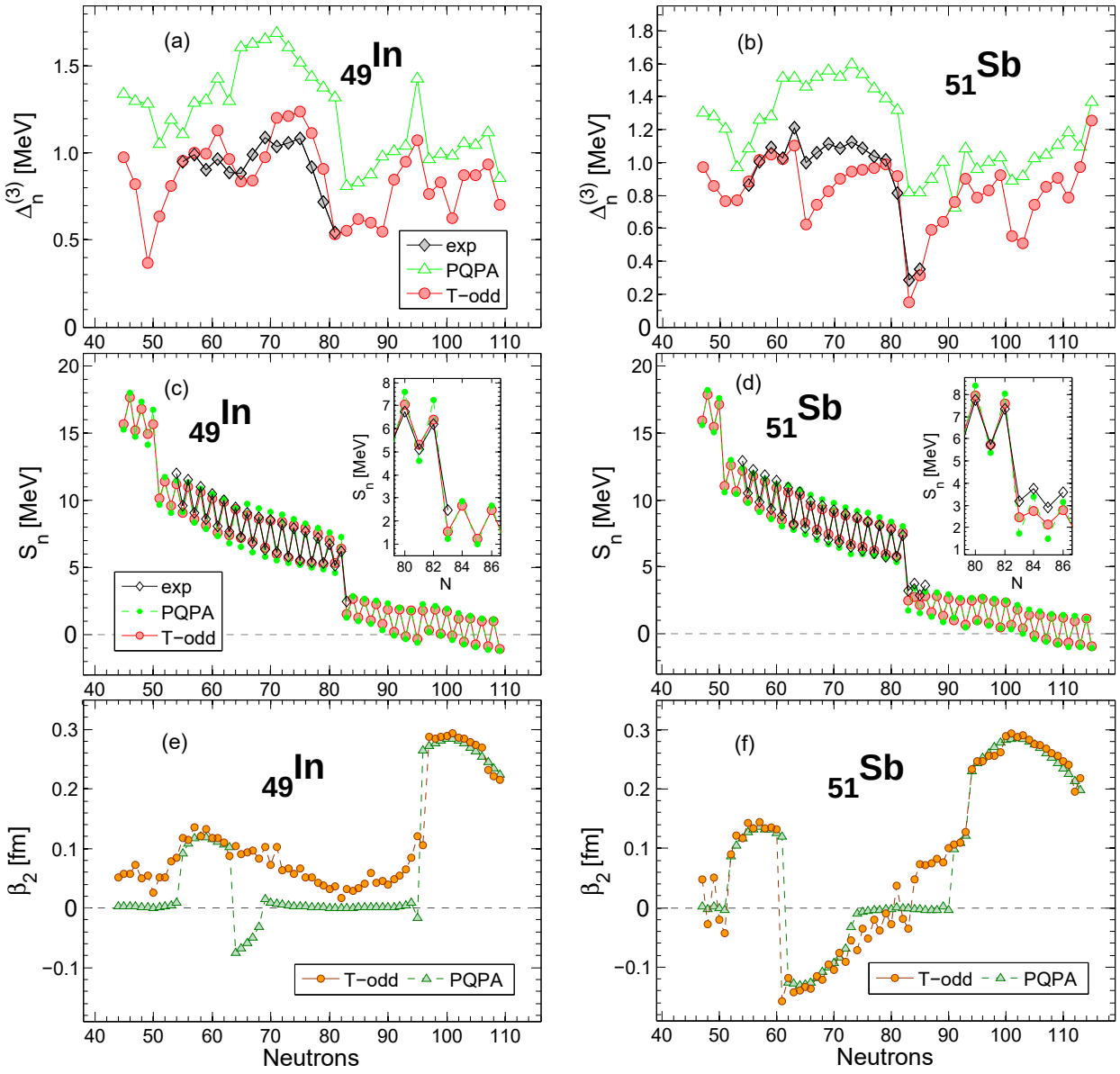

Fig. 7.9: The neutron pairing gaps obtained with PQPA method (green), and blocking approach (red), compared to experimental values (black) for (a) indium, and (b) antimony isotopes; corresponding one-neutron separation energies of (c) In–, and (d) Sb–isotopes; the estimates of quadrupole deformation parameter β_2 for (e) indium, and (f) antimony chains.

be found. On a closer inspection of the indium chain (Fig. 7.9 (a)), one observes a well-pronounced dip at around $N = 65$ in the T-odd calculations, just like for tin isotopes. This dive, although significantly shallower, is also visible experimentally, and yet it is not observed in the PQPA gaps, but rather on the contrary – a sudden rise of the pairing gaps is in place at $N = 65$. This discrepancy can be explained by looking at the Fig. 7.9 (e), where the β_2 deformation parameter for both theoretical approaches is plotted for the whole isotopic chain. One can clearly see the abrupt shape transition at $N = 64$ from prolate to a slightly oblate deformation in the PQPA case. Meanwhile, the T-odd

calculations do not predict such a sudden change, and the quadrupole moment decreases smoothly in this region. The underlying reason for such divergence is the presence of two nearly degenerate energy minima at $\beta_2 \approx \pm 0.1$ and the effects of deformation polarization coming from the unpaired nucleons, just as was the case with the Te_{67-73} isotopes discussed earlier in Sec. 7.2. Furthermore, the perturbative calculation for $N = 44 - 54$ and $N = 69 - 95$ yield mostly spherical results with $\beta_2 \approx 0$, whereas the polazization effects of the T-odd fields tend to slightly distort the nuclear densities across the whole isotopic chain up to $N = 96$, whereupon both approaches agree on a sudden jump to the prolate deformation with $\beta_2 \approx 0.26$. The one-neutron separation energies S_n of indium both for blocking and perturbative methods are plotted on Fig. 7.9 (c). The T-odd calculations tend to overpredict S_n for even-N nuclei and underpredict for odd-N values, which is particularly evident in the $N = 66 - 82$ region. The experimental shell gap at $N = 82$ is shown in the inset of Fig. 7.9 (c), which is likewise better replicated by the T-odd calculation. Overall, the resemblance of the full blocking results with the experiment is noticeably better than for the perturbative approach.

Turning to the antimony nuclei, shown in Fig. 7.9 (f), both PQPA and T-odd calculations evidence a shape transition at $N \approx 60$, and, apart from a small discrepancy in $N = 73 - 90$ region, reach a good agreement on the β_2 parameter for the rest of the chain. Despite this, the T-odd calculation exhibit a particularly strong drop in the gap strength at $N = 65$ (see Fig. 7.9 (b)), which is partly supported by the empirical results, and completely invisible in the PQPA calculations. This disparate behavior could not be explained by dissimilar predictions of β_2 at $N = 65$. We also can see an unusual dip for perturbative approximation at $N = 91$, where the calculated PQPA gap drops even slightly below the corresponding T-odd value. The situation with S_n values, plotted in Fig. 7.9 (d), is very similar to the indium case, where the T-odd calculations provide one-neutron separation energies noticeably closer to the experimental values, also reducing the shell gap by 1.15 MeV, shown in inset of Fig. 7.9 (d).

The last elements that we consider in detail are the heavier ${}_{89}\mathrm{Ac}$ and ${}_{91}\mathrm{Pa}$ chains. The neutron pairing gaps are plotted in Fig. 7.10 (a,b). On a large scale, the patterns from both calculations agree with each other, although perturbative gaps are ~ 230 keV stronger than the ones with T-odd fields. One can also notice, that just like the in case with In- and Sb-chains, the PQPA approximation smooths the gaps somewhat more than the blocking approach. There are 15 experimental gaps for actinium, and 14 for protactinium available to us at this moment – all showing similar patterns across the chains, but having some distinctive fingerprints. The first feature is very sharp dip at $N = 125$, where the $\Delta_n^{(3)}$ drop by ~ 250 keV for actinium, and a whole ~ 400 keV for protactinium. These marks are quantitatively very well reproduced by both calculations. There are apparent experimental gap quenching at $N = 133$ in both chains, and another one at $N = 149$ for protactinium. The overall tendency of the calculated gaps is to support this empirical evidence, but the agreement is on a much lesser level. For example, the gap quenching of calculated results appear to be shifted from the experimentally established $N = 133$ to $N = 131$ in both cases, and additionally from $N = 145$ to $N = 143$ in actinium chain. The theoretical gaps also tend to show more staggering, which is evident by looking at the $N = 133 - 147$ region. Finally, there is a huge spike in the gap strength appearing both for T-odd and PQPA calculations at $N = 129$ in Ac-chain. This peculiarity can be explained by looking at the Fig. 7.10 (c,d), where we clearly see that the calculations struggle significantly more in agreeing

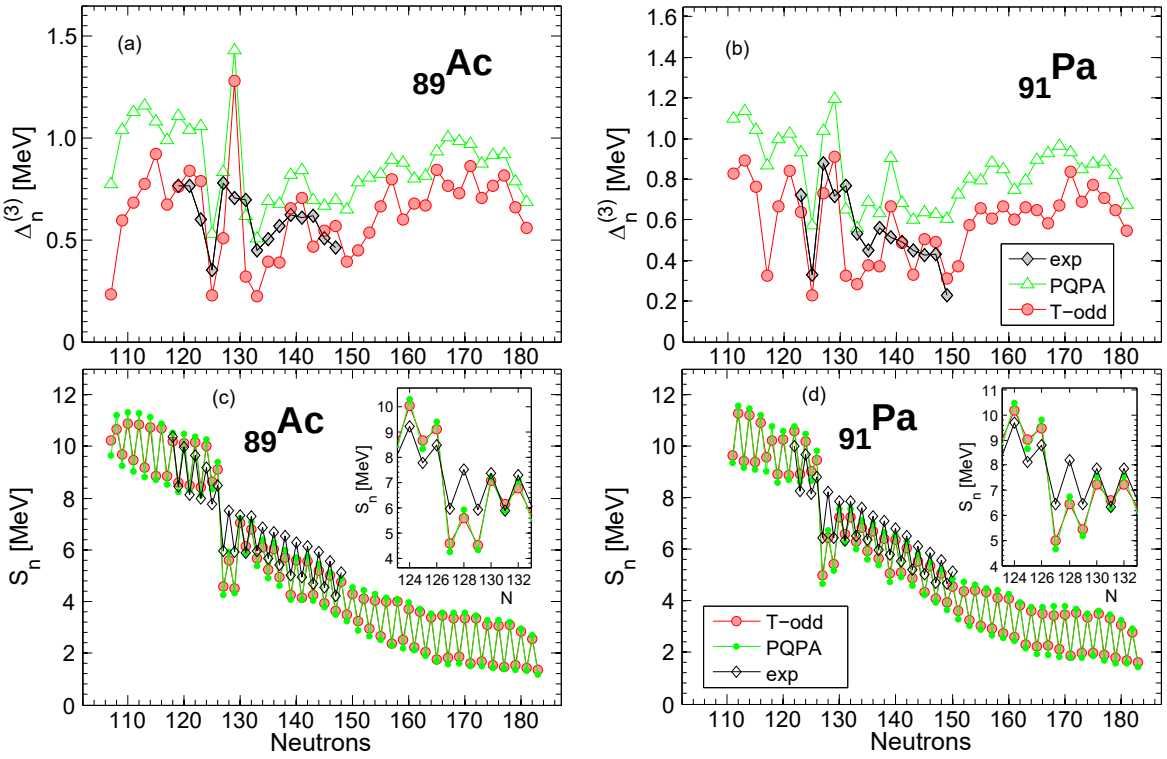

Fig. 7.10: Neutron pairing gaps for (a) actinium, and (b) protactinium isotopes, and the corresponding one-neutron separation energies of (c) Ac–, and (d) Pa–chains.

with experimental values around the $N = 126$ shell closure. For $N = 127$, and 129 the calculated one-neutron separation energies are understated by more than ~ 1.5 MeV, thereby the whole S_{2n} shell gap is largely overpredicted by $\sim$4.8 MeV in both chains, as can be seen in the insets of Fig. 7.10 (c,d).

7.4.3 Global systematics of the results

Having analyzed in detail a couple of representative chains, and on their examples highlighted the most prominent generic issues of both simplistic PQPA and proper self-consistent T-odd treatments of odd nuclei, we move on and discuss the overall trends and systematics in the pairing gaps across the whole nuclear chart. Upper panel (a) of Fig. 7.11 contains the pairing gaps of all isotopic chains computed in this survey from $Z = 8$ and up to $Z = 134$ with PQPA approximation, while the lower panel (b) shows the analogous results for T-odd treatment. The isotopes within a same chain are connected with solid lines. The even-Z chains are shown in red, while the odd-Z chains are plotted in blue. The experimental results are shown as a gray-shaded region in the background for comparison.

Overall, both PQPA and T-odd global calculatations exhibit a common trend of decreasing spread of the gaps for a single fixed N as one goes to heavier elements. In the case of PQPA one can also notice that the gaps tend to decrease in their strength for heavier isotopic chains, which is not visible in the T-odd calculations. The systematic decrease of the gap strength with the mass number is also present in the experimental,

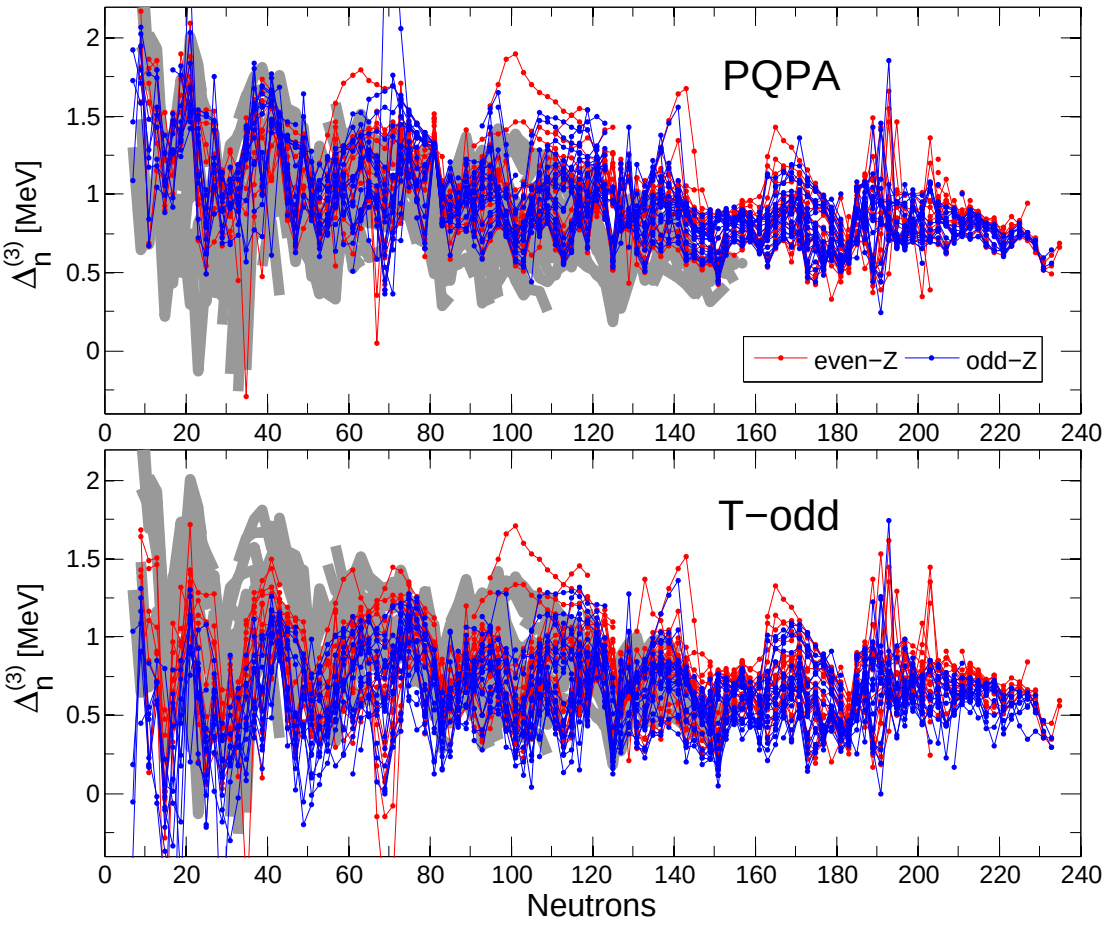

Fig. 7.11: Global surveys from $Z = 8$ up to Z=134 of calculated PQPA (upper panel) and T-odd (lower panel) pairing gaps for even-Z (red) and odd-Z (blue) chains. Isotopes are connected with lines. Gray region represents empirical results for comparison.

where one commonly implements an estimate $\Delta_n^{(3)} \approx 12/\sqrt{A}$ MeV based on global fit to empirical results [224, 292, 338]. Another feature on the global scale is the occurrence of many narrow, both negative and positive, spikes in the PQPA results – particularly noticeable in the region $N \approx 50 - 120$. The T-odd gaps appear to be more smeared out, with only a couple of major well-established dips occurring in vicinity from the magic numbers $N = 28, 50, 82, 126$ and a couple of other values of neutron number. Besides the fact that the PQPA approximation overall yield larger gaps than T-odd calculations, another striking difference is that there is a apparent tendency of odd-Z gaps having weaker strength than in the even-Z chains. This feature is qualitatively visible in the Fig. 7.11 (b), where the odd-Z chains (blue) are shifted downwards with respect to the even-Z chains (red), whereas the PQPA calculatation, shown in Fig. 7.11 (a), clearly does not exhibit this feature. This was quantitatively verified in Table 7.1, where the calculated number of 1985 even-Z and the same quantity of odd-Z pairing gaps have an identical average of 0.95 MeV, whereas the T-odd calculations for the same nuclei have 0.73 MeV and 0.62 MeV for even-Z and odd-Z cases, respectively. This dependence on proton number parity is also established experimentally, where the total number of 556 even-Z gaps are found to have 1.06 MeV, while the 508 established odd-Z gaps yield

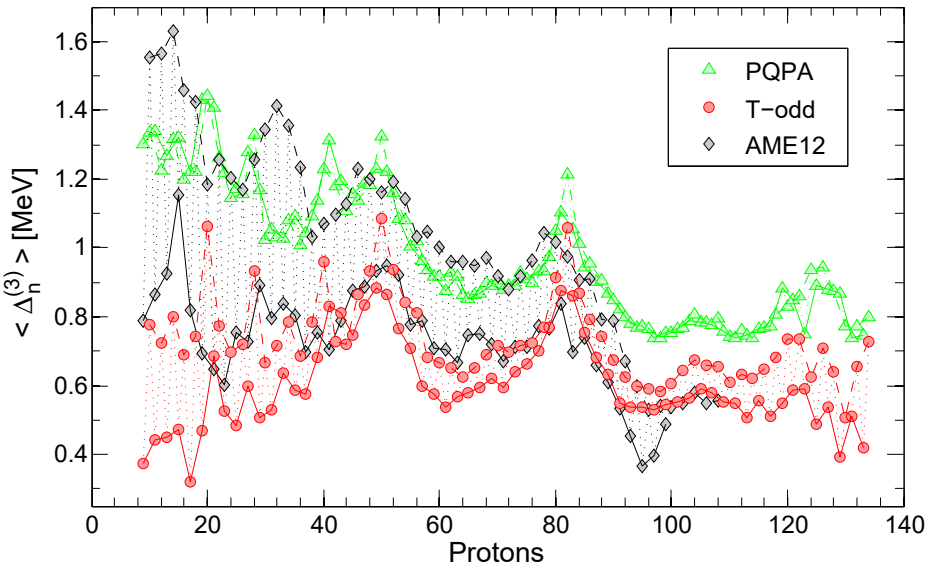

Fig. 7.12: Average pairing gaps $\langle\Delta_n^{(3)}\rangle$ for odd-Z chains (solid lines) and even-Z chains (dashed lines). The neighboring elements are connected with dotted lines.

0.76 MeV on average. Interestingly, the standard deviation in all the cases of calculated gaps is found to be $\sim$0.28 MeV.

The lack of significant dependence of the gaps strength upon the Z–number can be seen even more clearly in Fig. 7.12, where the average pairing gaps for a given Z-number are shown. The experimental results (shown in black) start off with as much as $0.6-0.8$ MeV difference in $\langle\Delta_n^{(3)}\rangle$ between the neighboring lighter elements, and this staggering gradually decreases towards the heavier elements. Quantitatively, such staggering is also observed in the T-odd calculations, albeit somewhat less pronounced. And, as was already anticipated from the previous results, the PQPA approximations completely lack this feature. This is due to the fact, that the PQPA energies both for *even* and *odd* nuclei are extracted from the wave function of *even* number parity, while compensating for overbinding by adding either one (odd-A mass), or two (doubly odd) lowest q.p. excitation energies. Being fully-paired, the many-body states not only lack an explicit break of a proton and/or a neutron pair, but also exhibit a similar and smoothly varying q.p. spectra across the isotopic chain irrespective of the number parity.

$\langle\Delta_n^{(3)}\rangle$ [MeV]	even-Z	odd-Z
T-odd	0.732 ± 0.282	0.622 ± 0.282
PQPA	0.950 ± 0.282	0.947 ± 0.283
Exp.	1.061 ± 0.334	0.760 ± 0.256

Table 7.1: Numerical values of average pairing gaps for even-Z and odd-Z chains.

7.5 Summary and perspective

We have performed a large-scale survey with a proper treatment of T-odd fields of Gogny EDF within the framework of an exact blocking method to calculate ground states of both odd-A and doubly odd nuclei up to the neutron drip lines from $Z = 8$ up to $Z = 134$. We have also extracted binding energies with an approximative PQPA approach, and compared the results from both methods with the experimental values.

On a large scale, the PQPA method generally tends to overestimate the gap strength, while the opposite holds for the T-odd approach. The empirical dependence of the overall gap strength on the proton number parity is found to be qualitatively reproduced in blocking calculatations, while the PQPA calculations completely lack this effect. On the other hand, there is almost no dependence of the gap strength on the Z-number in T-odd calculations, whilst this experimental phenomenology is clearly established in PQPA results (Fig. 7.12). Thereby we can confirm this systematic deficiency of Gogny parametrization that was already established earlier [310].

On the scale of separate isotopic chains, both theoretical approaches are found to provide an overall coarse description of the experimental pairing gaps on the qualitative level, reproducing the gap quenchings and most of the other features of the pairing gaps. While perturbative treatment of odd nuclei smooths out somewhat the pairing

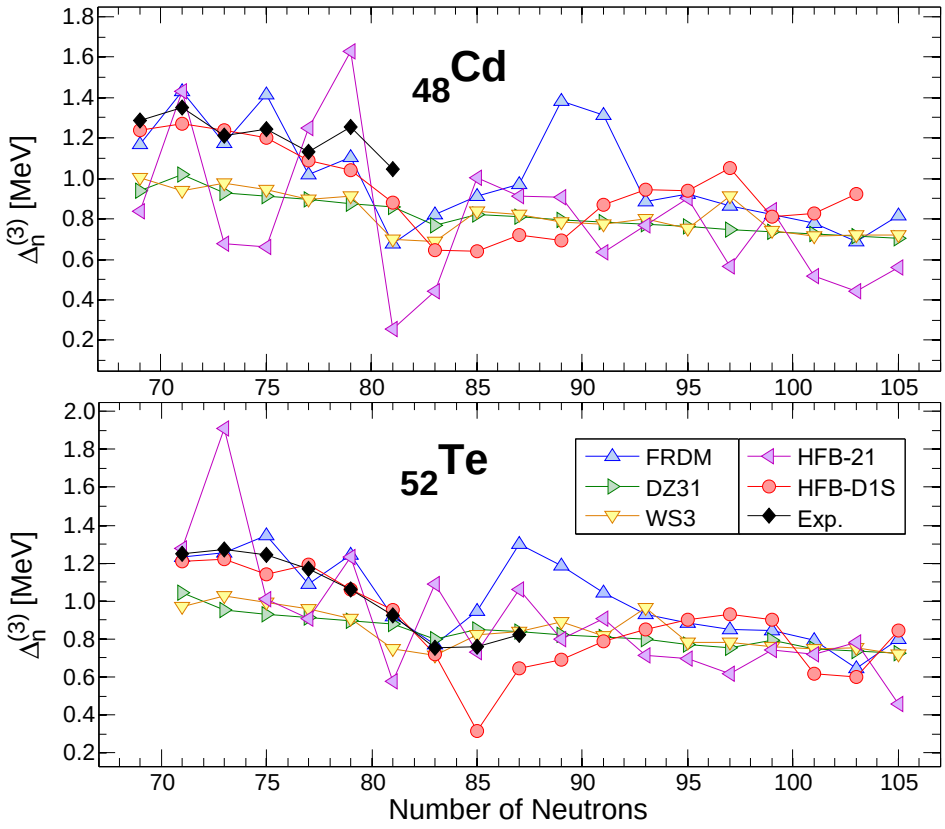

Fig. 7.13: Pairing gaps for cadmium (upper) and tellurium (lower) isotopic chains calculated with different mass models used in astrophysics: FRDM [129], DZ31 [136], WS3 [134], HFB-21 [23]. Compared to our HFB-D1S results and the experimental values.

gaps across the isotopic chains, the blocking calculation was found to capture some of the more subtle traits of the experimental results. Nonetheless, the calculations with explicit T-odd fields are far from resolving all deviations of PQPA approximation from the experimental results. Notably, both treatments perform especially bad in the direct vicinity to the shell closures, which is particularly visible in neutron-separation energies. Despite this, we have highlighted most of the distinctive properties and shortcomings of the calculations, and gave the explanations to some of the underlying shell structure features.

The analysis of equal filling approximation performed in Ref. [310] suggests that the role of T-odd fields in D1S parametrization of Gogny interaction is weak. Despite this, a better parametrization of the Gogny EDF can alter the mean-field energy contribution to the pairing effects and change the overall Z-dependence of the gap strengths [310, 322, 339]. In order to further enhance the predictive power of the functional, and thereby avoid any local parameters adjustement, a new functional form is needed to be established that perhaps incorporates a flexible tensor potential, and richer finite-range spin-orbit interaction [279]. However, since there are also other mechanisms that can contribute to OES, an improvement is also expected by going beyond the mean-field level of wave function description. Projecting onto a good particle number, and restoring the angular momentum can substantially change the described state of affairs.

Despite the fact that the mass models momentarily used in astrophysics have recently achieved a very good level of description of the known nuclei, all having rms deviations from experimental values less than ~ 0.8 MeV, the local discrepancies and significant difference in the calculations of unknown nuclei have a very noticeable impact on calculations of r-process elemental abundances. The Fig. 7.13 highlights this fact on the examples of cadmium and tellurium, showing the theoretical estimates of the pairing gaps for some of the widely used mass models. In any case, the only way to surpass all the limitations of current models is to continue an active development of the density functional theories, while improving both the mean-field description, as well as augmenting it with beyond-mean-field effects.

8 Concluding remarks and remaining challenges

In the beginning of this work we have outlined the recent progress and the main difficulties in constructing a unified model of low-energy nuclear structure from the first principles. While the highly non-perturbative regime of low-energy QCD poses the first major complication along such a formidable challenge, another obstacle stems from the many-body yet finite-size nature of the nuclear system itself. This fact significantly restricts the computationally accessible domain of the fundamental *ab initio* methods, while also preventing its statistical treatment. However, aiming at a high-precision description of such nuclear ground-state properties, as masses, radii, and deformations, one does not necessarily has to revert to the "all-inclusive" *ab initio* approaches. This was indeed demonstrated by the impressively low rms values obtained with the phenomenological mic-mac mass formulas. Nevertheless, since the descriptive accuracy of a model is not necessarily correlated with its predictive power, a greater reliability in theoretical extrapolations to the limits of the nuclear chart is generally expected by implementing a more microscopic description of the nuclear structure. The SCMF approach based on the nuclear EDF theory is currently the only option to provide both microscopic and universal description for such ground-state nuclear properties, as binding energies, radii, quadrupole, and other multipole deformations across the whole nuclear chart.

In order to further improve the precision of the currently available SCMF methods, we have identified three topics of particular importance that are generally relevant to all of the present HFB-based global nuclear models, namely

I. an insufficient convergence of calculations in truncated working bases, and techniques to extrapolate the results to the limit of infinite model space (Chap. 5);

II. lack of important correlations and broken symmetries in the HFB mean-field formalism, which require implementation of beyond-mean-field techniques to account for (Chap. 6);

III. importance of time-odd fields in the HFB calculations of odd-mass nuclei, and incorporation of the self-consistent blocking techniques for their proper treatment (Chap. 7).

While detailed summary, thorough discussion, and future perspectives for each of the mentioned topics can be found at the end of the corresponding chapters, we provide here only the gross summary of the whole thesis along with its most important conclusions and concisely list the direction for the future studies.

The study performed in Chap. 5 has confirmed that the calculated binding energies are largely underconverged in the truncated SHO bases. The analysis of the convergence

patterns has demonstrated significant inconsistencies in one of the widely used phenomenological energy-correction scheme. Hence, in an attempt to reliably extrapolate our results to the limit of an infinite working basis, we have systematically tested one of the recently proposed IR energy-correction scheme. We found that this technique, at least in the context of Gogny-HFB approach, is robust only in the region of well-bound nuclei. Nevertheless, we have demonstrated that a better convergence treatment removes the numerical noise that was found in some of the previous HFB calculations, and also brings down the global rms deviation with experimental masses. Additionally, this has also a noticeable impact on the extracted separation-energies. For example, we have eliminated most of the artificial abrupt jumps in the two-neutron separation energies that plagued some of the recent global Gogny-HFB surveys. This has also brought the calculated separation-energies closer to the smoother phenomenology of the corresponding experimental values. Moreover, while the total binding energies calculated in truncated SHO bases were found to be far from converged, we have demonstrated that the extracted separation energies are converged on $\sim$ 100 keV level even for the neutron-rich isotopes near the drip line. Altogether, with much of the numerical noise removed, the calculated masses and binding energies can now be plugged into the r-process nucleosynthesis calculation with greater confidence.

In Chap. 6 we have extended the HFB mean-field formalism with BMF techniques and performed a systematic analysis of the SCCM method without the usually adopted GOA approximations. We carried out global BMF calculations both with D1S and D1M parametrizations of Gogny interaction and compared binding, separation, and 2^+–excitation energies of the calculated doubly even nuclei to the available experimental data. We found that the BMF effects amount to $5-6$ MeV of correlation energy, and tend to decrease the observed strong shell effects particularly in the region of light nuclei. The two-neutron separation energies are also found to be in a better agreement with experimental data. In particular, the BMF corrections brought the theoretical predictions closer towards the experimental values for $N, Z = 20$ shell gaps. But the necessity of performing the computationally heavy BMF calculations in the significantly reduced dimensions of the working basis have re-introduced some of the previously removed numerical noise. Nevertheless, by performing such large-scale SCCM calculation without the commonly employed GOA approximations we have eliminated another source of numerical uncertainty in the previous BMF implementations, and established the directions in which the the future work should be focused. While the accumulated experience from the convergence analysis performed earlier will allow us to eliminate the artificial noise due to insufficient convergence in the subsequent BMF surveys, the exploration of triaxiality and other degrees of freedom are also mandatory. Moreover, while a better parametrization of Gogny EDF that explicitly accounts for SCCM method is certainly desirable, new functional forms of EDF should also be explored in order to further reduce the uncertainties from the nuclear structure models in r-process calculations.

Finally, in Chap. 7 we introduced all the necessary tools to perform self-consistent blocking calculations of the odd-A and doubly odd nuclei within the HFB framework. We presented our large-scale survey with an explicit treatment of all T-odd components in Gogny EDF for nuclei up to the neutron drip line in the $8 \leq Z \leq 134$ range. We also compared our calculation to the available experimental data, as well as values obtained with the widely used PQPA method of approximative blocking. The calculations with ex-

plicit T-odd fields were generally found to capture more subtle traits of the observed odd-even staggering effects than the PQPA approach. Moreover, an important difference of these two methods is seen when comparing separate isotopic chains with different proton-number parities: the T-odd calculations yield reduced strength for the odd-Z chains with respect to the even-Z chains, precisely following the experimental phenomenology. The PQPA calculations clearly do not exhibit this feature, which underlines the importance of self-consistency in the calculations of odd nuclei. Overall, the pairing strength of D1S functional is found adequate to qualitatively describe the principle features of the experimentally known gaps, but their mass-dependence is not very well reproduced in T-odd calculations. Ultimately, in order to improve the theoretical results, the odd nuclei should be properly considered in fitting protocols of a better parametrization, while also exploring the impact of BMF correlations. All things considered, we have showed that a proper treatment of the T-odd fields has a direct impact on the predicted pairing effects, which, through the extracted separation-energies, could leave a noticeable imprint on the calculated r-process abundances.

Summing everything up, in this work we have addressed and systematically studied the three mentioned topics that are particularly important for constructing a reliable mass model based on EDF approach. By introducing new or improved methods we were able to obtain better results and gain a firmer control on these issues. We thereby have taken another three steps along the path towards a better microscopic mass model for the purposes of r-process nucleosynthesis calculations. We conclude this work by outlining our view on the most important remaining challenges of the present nuclear EDF theory:

- Quite generally, all of the modern EDF approaches based on Skyrme and Gogny interactions, or relativistic Lagrangians are, in principle, capable of providing a good level of description for the nuclear ground-state properties. While the symmetry-breaking mechanism of the HFB formalism holds the key in accounting for such indispensable static nuclear correlations, as deformation and pairing, the restoration of the broken symmetries is essential to include the important missing collective correlations, and thereby also allows to extend the theoretical description to such spectroscopic nuclear properties, as excited states and transitions. The question of providing a consistent framework to incorporate various beyond-mean-field correlations – both from symmetry-restorations and from collective fluctuations around the mean-field minima – is one of the current challenges of the EDF approach. See, for example, Ref. [219] for a recent overview of the state-of-the-art BMF methods.

- Another important question is related to the predictive power of the EDF theory. The semi-phenomenological form of the effective interaction is adapted for the HFB and BMF calculations by extensive fits to the experimentally known nuclear data. This inevitably leads to predictions of unknown nuclear properties that are rather dependent on the particular choice of the parametrization. Hence, this fact introduces systematic errors that propagate up to the limits of the nuclear chart and makes the tools for their controlled improvements rather obscure. Development of the new functional forms for EDF calculations that are more rigorously constrained by the microscopic considerations would undoubtedly provide a greater confidence in theoretical extrapolations towards the nuclear drip lines. Inspired by the recent

success of χEFT and RG techniques, the search for a firmer link between the energy density functional and the underlying fundamental interactions is already underway, but it poses a serious challenge for the nuclear physics community in the years to come. See, for example, Refs. [80, 340, 341] and references therein, for some of the most recent achievements in this direction.

- Finally, irrespective of the physical origin and the mathematical structure of the new functional forms, the EDF approach will unavoidably contain a number of phenomenological components that need to be tuned to the experimental data. Such components are not only required to make the nuclear many-body problem computationally feasible, but are also necessary to effectively account for the potentially missing correlations. The uncertainties of theoretical predictions will inevitably depend *not* only on the actual form of the EDF and the nuclear data used to establish its the free parameters, but will *also* depend on the actual details of the optimization in the fitting procedure itself. Moreover, the necessary truncations of the working basis and other details of numerical implementations play also a very important role, and can easily inhibit the calculations from converging to the exact solution of the method. The development of a rigorous methodology to identify all such important uncertainties, quantify the implementation errors and propagate them to the model predictions is another substantial challenge in the future development of the EDF theory. See, for example, Ref. [342] for a recent review on the latest progress in this topic.

List of Figures

Bibliography

[1] E. M. Burbidge, G. R. Burbidge, W. A. Fowler, and F. Hoyle, "Synthesis of the Elements in Stars", Rev. Mod. Phys. **29**, 547–650 (1957).

[2] A. G. W. Cameron, "Nuclear Reactions in Stars and Nucleogenesis", PASP **69**, 201 (1957).

[3] F. Käppeler, R. Gallino, S. Bisterzo, and W. Aoki, "The s-process: Nuclear physics, Stellar models, and Observations", Rev. Mod. Phys. **83**, 157–194 (2011).

[4] Y.-Z. Qian, "The origin of the heavy elements: Recent progress in the understanding of the r-process", Prog. Part. Nucl. Phys. **50**, 153–199 (2003).

[5] Y.-Z. Qian and G. J. Wasserburg, "Where, oh where has the r-process gone?", Phys. Rep. **442**, 237–268 (2007).

[6] M. Arnould, S. Goriely, and K. Takahashi, "The r-process of Stellar Nucleosynthesis: astrophysics and nuclear physics achievements and mysteries", Phys. Rep. **450**, 97–213 (2007).

[7] F.-K. Thielemann, M. Eichler, I. Panov, M. Pignatari, and B. Wehmeyer, *Handbook of Supernovae*, edited by A. W. Alsabti and P. Murdin (Springer, 2017).

[8] National Research Council, *Connecting quarks with the cosmos: eleven science questions for the new century* (The National Academies Press, 2003).

[9] National Research Council, *Nuclear physics: exploring the heart of matter* (The National Academies Press, 2013).

[10] K. Langanke and G. Martínez-Pinedo, "Nuclear weak-interaction processes in stars", Rev. Mod. Phys. **75**, 819–862 (2003).

[11] C. Sneden and J. J. Cowan, "Genesis of the Heaviest Elements in the Milky Way Galaxy", Science **299**, 70–75 (2003).

[12] B. H. Sun, Y. A. Litvinov, I. Tanihata, and Y. H. Zhang, "Toward precision mass measurements of neutron-rich nuclei relevant to r-process nucleosynthesis", Frontiers of Physics **10**, 1–25 (2015).

[13] G. Audi, M. Wang, A. H. Wapstra, F. Kondev, M. MacCormick, X. Xu, and B. Pfeiffer, "The AME2012 atomic mass evaluation (I). Evaluation of input data, adjustment procedures", Chinese physics C **36**, 1287 (2012).

[14] M. Wang, G. Audi, A. H. Wapstra, F. Kondev, M. MacCormick, X. Xu, and B. Pfeiffer, "The AME2012 atomic mass evaluation (II). Tables, graphs and references", Chinese physics C **36**, 1603 (2012).

[15] G. Audi and A. H. Wapstra, "The 1995 update to the atomic mass evaluation", Nucl. Phys. A **595**, 409–480 (1995).

[16] A. Sobiczewski and Y. A. Litvinov, "Predictive power of nuclear-mass models", Phys. Rev. C **90**, 017302 (2014).

[17] A. Arcones and G. Martínez-Pinedo, "Dynamical r-process studies within the neutrino-driven wind scenario and its sensitivity to the nuclear physics input", Phys. Rev. C **83**, 045809 (2011).

[18] M. R. Mumpower, R. Surman, G. C. McLaughlin, and A. Aprahamian, "The impact of individual nuclear properties on r-process nucleosynthesis", Prog. Part. Nucl. Phys. **86**, 86–126 (2016).

[19] J. J. Mendoza-Temis, M.-R. Wu, K. Langanke, G. Martínez-Pinedo, A. Bauswein, and H.-T. Janka, "Nuclear robustness of the r process in neutron-star mergers", Phys. Rev. C **92**, 055805 (2015).

[20] N. Chamel, S. Goriely, and J. M. Pearson, "Further explorations of Skyrme-Hartree-Fock-Bogoliubov mass formulas. IX: Constraint of pairing force to $^1S_0$ neutron-matter gap", Nucl. Phys. A **812**, 72–98 (2008).

[21] S. Goriely, N. Chamel, and J. M. Pearson, "Further explorations of Skyrme-Hartree-Fock-Bogoliubov mass formulas. XIII. The 2012 atomic mass evaluation and the symmetry coefficient", Phys. Rev. C **88**, 024308 (2013).

[22] G. Audi, A. H. Wapstra, and C. Thibault, "The AME2003 atomic mass evaluation (II). Tables, graphs and references", Nucl. Phys. A **729**, 337–676 (2003).

[23] S. Goriely, N. Chamel, and J. M. Pearson, "Further explorations of Skyrme-Hartree-Fock-Bogoliubov mass formulas. XII. Stiffness and stability of neutron-star matter", Phys. Rev. C **82**, 035804 (2010).

[24] D. J. Gross and F. Wilczek, "Ultraviolet Behavior of Non-Abelian Gauge Theories", Phys. Rev. Lett. **30**, 1343–1346 (1973).

[25] H. D. Politzer, "Reliable Perturbative Results for Strong Interactions?", Phys. Rev. Lett. **30**, 1346–1349 (1973).

[26] N. Ishii, S. Aoki, and T. Hatsuda, "Nuclear Force from Lattice QCD", Phys. Rev. Lett. **99**, 022001 (2007).

[27] S. R. Beane, W. Detmold, K. Orginos, and M. J. Savage, "Nuclear physics from lattice QCD", Prog. Part. Nucl. Phys. **66**, 1–40 (2011).

[28] S. Aoki, "From Quarks to Nuclei: Challenges of Lattice QCD", Nucl. Phys. B Proc. Suppl. **195**, 281–287 (2009).

[29] Z. Fodor and C. Hoelbling, "Light hadron masses from lattice QCD", Rev. Mod. Phys. **84**, 449–495 (2012).

[30] I. Campos, P. Fritzsch, C. Pena, D. Preti, A. Ramos, and A. Vladikas, "Controlling quark mass determinations non-perturbatively in three-flavour QCD", in EPJ Web of Conf. Vol. 137 (Mar. 2017).

[31] J. Greensite, *An Introduction to the Confinement Problem*, Lecture Notes in Physics (Springer, 2011).

[32] H. Yukawa, "On the Interaction of Elementary Particles I", Proc. Phys. Math. Soc. Jap. **17**, 48–57 (1935).

[33] R. Machleidt and I. Slaus, "The nucleon-nucleon interaction", J. Phys. G **27**, R69–R108 (2001).

[34] V. G. J. Stoks, R. A. M. Klomp, C. P. F. Terheggen, and J. J. de Swart, "Construction of high-quality NN potential models", Phys. Rev. C **49**, 2950–2962 (1994).

[35] R. Machleidt, "High-precision, charge-dependent Bonn nucleon-nucleon potential", Phys. Rev. C **63**, 024001 (2001).

[36] R. B. Wiringa, V. G. J. Stoks, and R. Schiavilla, "Accurate nucleon-nucleon potential with charge-independence breaking", Phys. Rev. C **51**, 38–51 (1995).

[37] S. C. Pieper, K. Varga, and R. B. Wiringa, "Quantum Monte Carlo calculations of A = 9,10 nuclei", Phys. Rev. C **66**, 044310 (2002).

[38] S. C. Pieper, V. R. Pandharipande, R. B. Wiringa, and J. Carlson, "Realistic models of pion-exchange three-nucleon interactions", Phys. Rev. C **64**, 014001 (2001).

[39] B. S. Pudliner, V. R. Pandharipande, J. Carlson, and R. B. Wiringa, "Quantum Monte Carlo Calculations of A >6 Nuclei", Phys. Rev. Lett. **74**, 4396–4399 (1995).

[40] S. A. Coon, M. D. Scadron, P. C. McNamee, B. R. Barrett, D. W. E. Blatt, and B. H. J. McKellar, "The two-pion-exchange three-nucleon potential and nuclear matter", Nucl. Phys. A **317**, 242–278 (1979).

[41] S. Weinberg, "Phenomenological Lagrangians", Physica A **96**, 327–340 (1979).

[42] R. Machleidt and D. R. Entem, "Chiral effective field theory and nuclear forces", Phys. Rep. **503**, 1–75 (2011).

[43] E. Epelbaum, H.-W. Hammer, and U.-G. Meißner, "Modern theory of nuclear forces", Rev. Mod. Phys. **81**, 1773–1825 (2009).

[44] J. Golak, R. Skibiński, K. Topolnicki, H. Witała, E. Epelbaum, H. Krebs, H. Kamada, U.-G. Meißner, V. Bernard, P. Maris, J. Vary, S. Binder, A. Calci, K. Hebeler, J. Langhammer, R. Roth, A. Nogga, S. Liebig, and D. Minossi, "Low-energy neutron-deuteron reactions with N^3LO chiral forces", Eur. Phys. J. A **50**, 177 (2014).

[45] H. Witała, W. Glöckle, J. Golak, A. Nogga, H. Kamada, R. Skibiński, and J. Kuroś-Żołnierczuk, "Nd elastic scattering as a tool to probe properties of 3N-forces", Phys. Rev. C **63**, 024007 (2001).

[46] A. Nogga, D. Hüber, H. Kamada, and W. Glöckle, "Triton binding energies for modern NN forces and the π-π exchange three-nucleon force", Phys. Lett. B **409**, 19–25 (1997).

[47] R. Lazauskas and J. Carbonell, "Testing nonlocal nucleon-nucleon interactions in four-nucleon systems", Phys. Rev. C **70**, 044002 (2004).

[48] R. Lazauskas, "Elastic proton scattering on tritium below the n-^{3}He threshold", Phys. Rev. C **79**, 054007 (2009).

[49] A. Deltuva and A. C. Fonseca, "Four-nucleon scattering: Ab initio calculations in momentum space", Phys. Rev. C **75**, 014005 (2007).

[50] A. Deltuva and A. C. Fonseca, "Four-Body Calculation of Proton-^{3}He Scattering", Phys. Rev. Lett. **98**, 162502 (2007).

[51] M. Hjorth-Jensen, M. Lombardo, and U. van Kolck, *An Advanced Course in Computational Nuclear Physics: Bridging the Scales from Quarks to Neutron Stars*, Lecture Notes in Physics (Springer, 2017).

[52] J. Carlson, S. Gandolfi, F. Pederiva, S. C. Pieper, R. Schiavilla, K. E. Schmidt, and R. B. Wiringa, "Quantum Monte Carlo methods for nuclear physics", Rev. Mod. Phys. **87**, 1067–1118 (2015).

[53] A. Gezerlis, I. Tews, E. Epelbaum, M. Freunek, S. Gandolfi, K. Hebeler, A. Nogga, and A. Schwenk, "Local chiral effective field theory interactions and quantum Monte Carlo applications", Phys. Rev. C **90**, 054323 (2014).

[54] S. C. Pieper and R. B. Wiringa, "Quantum Monte Carlo Calculations of Light Nuclei", Annu. Rev. Nucl. Part. Sci. **51**, 53–90 (2001).

[55] J. E. Lynn, I. Tews, J. Carlson, S. Gandolfi, A. Gezerlis, K. E. Schmidt, and A. Schwenk, "Chiral Three-Nucleon Interactions in Light Nuclei, Neutron-α Scattering, and Neutron Matter", Phys. Rev. Lett. **116**, 062501 (2016).

[56] K. E. Schmidt and S. Fantoni, "A quantum Monte Carlo method for nucleon systems", Phys. Lett. B **446**, 99–103 (1999).

[57] E. Epelbaum, H. Krebs, T. A. Lähde, D. Lee, and U.-G. Meißner, "Structure and Rotations of the Hoyle State", Phys. Rev. Lett. **109**, 252501 (2012).

[58] T. A. Lähde, E. Epelbaum, H. Krebs, D. Lee, U.-G. Meißner, and G. Rupak, "Lattice effective field theory for medium-mass nuclei", Phys. Lett. B **732**, 110–115 (2014).

[59] P. Ring and P. Schuck, *The nuclear many-body problem* (Springer, 1980).

[60] W. Leidemann and G. Orlandini, "Modern ab initio approaches and applications in few-nucleon physics with A > 4", Prog. Part. Nucl. Phys. **68**, 158–214 (2013).

[61] A. Kievsky, M. Viviani, L. E. Marcucci, and S. Rosati, "Recent developments in few-nucleon systems", Nucl. Phys. A **737**, 61–69 (2004).

[62] S. Deflorian, N. Barnea, W. Leidemann, and G. Orlandini, "Nonsymmetrized Hyperspherical Harmonics with Realistic NN Potentials", Few-Body Systems **54**, 1879–1887 (2013).

[63] M. Gattobigio, A. Kievsky, and M. Viviani, "Nonsymmetrized hyperspherical harmonic basis for an A-body system", Phys. Rev. C **83**, 024001 (2011).

[64] P. Navrátil, S. Quaglioni, I. Stetcu, and B. R. Barrett, "Recent developments in no-core shell-model calculations", J. Phys. G **36**, 083101 (2009).

[65] B. R. Barrett, P. Navrátil, and J. P. Vary, "Ab initio no core shell model", Prog. Part. Nucl. Phys. **69**, 131–181 (2013).

[66] A. M. Shirokov, J. P. Vary, A. I. Mazur, and T. A. Weber, "Realistic nuclear Hamiltonian: Ab exitu approach", Phys. Lett. B **644**, 33–37 (2007).

[67] D. R. Entem and R. Machleidt, "Accurate charge-dependent nucleon-nucleon potential at fourth order of chiral perturbation theory", Phys. Rev. C **68**, 041001 (2003).

[68] S. Ôkubo, "Diagonalization of Hamiltonian and Tamm-Dancoff Equation", Prog. Theo. Phys. **12**, 603–622 (1954).

[69] K. Suzuki and S. Y. Lee, "Convergent Theory for Effective Interaction in Nuclei", Prog. Theo. Phys. **64**, 2091–2106 (1980).

[70] R. Roth and P. Navrátil, "Ab Initio Study of ^{40}Ca with an Importance-Truncated No-Core Shell Model", Phys. Rev. Lett. **99**, 092501 (2007).

[71] R. Roth, "Importance truncation for large-scale configuration interaction approaches", Phys. Rev. C **79**, 064324 (2009).

[72] R. Roth, A. Calci, J. Langhammer, and S. Binder, "Evolved chiral NN+3N Hamiltonians for ab initio nuclear structure calculations", Phys. Rev. C **90**, 024325 (2014).

[73] R. Roth, S. Binder, K. Vobig, A. Calci, J. Langhammer, and P. Navrátil, "Medium-Mass Nuclei with Normal-Ordered Chiral NN+3N Interactions", Phys. Rev. Lett. **109**, 052501 (2012).

[74] K. D. Launey, A. C. Dreyfuss, T. Dytrych, J. P. Draayer, D. Langr, P. Maris, J. P. Vary, and C. Bahri, "Symmetry-adapted ab initio no-core shell model calculations for ^{12}C", in J. Phys. Conf. Series, Vol. 436 (Apr. 2013).

[75] L. Lang, "No-core monte carlo shell model calculations with unitary correlation operator method and similarity renormalization group", Chinese Physics C **39**, 054103 (2015).

[76] C. J. Horowitz and B. D. Serot, "Relativistic Hartree theory of finite nuclei: The role of the quantum vacuum", Phys. Lett. B **140**, 181–186 (1984).

[77] R. Brockmann and R. Machleidt, "Nuclear saturation in a relativistic Brueckner-Hartree-Fock approach", Phys. Lett. B **149**, 283–287 (1984).

[78] J. W. Clark and E. Feenberg, "Simplified Treatment for Strong Short-Range Repulsions in N-Particle Systems. I. General Theory", Phys. Rev. **113**, 388–399 (1959).

[79] J. W. Clark and P. Westhaus, "Method of Correlated Basis Functions", Phys. Rev. **141**, 833–857 (1966).

[80] T. Duguet, M. Bender, J.-P. Ebran, T. Lesinski, and V. Somà, "Ab initio-driven nuclear energy density functional method. A proposal for safe/correlated/improvable parametrizations of the off-diagonal EDF kernels", Eur. Phys. J. A **51**, 162 (2015).

[81] R. J. Furnstahl and K. Hebeler, "New applications of renormalization group methods in nuclear physics", Rep. Prog. Phys. **76**, 126301 (2013).

[82] S. K. Bogner, T. T. S. Kuo, and A. Schwenk, "Model-independent low momentum nucleon interaction from phase shift equivalence", Phys. Rep. **386**, 1–27 (2003).

[83] F. Wegner, "Flow-equations for Hamiltonians", Annalen der Physik **506**, 77–91 (1994).

[84] R. Roth, T. Neff, and H. Feldmeier, "Nuclear structure in the framework of the Unitary Correlation Operator Method", Prog. Part. Nucl. Phys. **65**, 50–93 (2010).

[85] R. J. Furnstahl, "The Renormalization Group in Nuclear Physics", Nuc. Phys. B Proc. Suppl. **228**, 139–175 (2012).

[86] S. K. Bogner, R. J. Furnstahl, and R. J. Perry, "Similarity renormalization group for nucleon-nucleon interactions", Phys. Rev. C **75**, 061001 (2007).

[87] F. Coester, "Bound states of a many-particle system", Nucl. Phys. A **7**, 421–424 (1958).

[88] R. F. Bishop, M. F. Flynn, M. C. Boscá, E. Buenda, and R. Guardiola, "Translationally invariant coupled cluster theory for simple finite systems", Phys. Rev. C **42**, 1341–1360 (1990).

[89] J. H. Heisenberg and B. Mihaila, "Ground state correlations and mean field in ^{16}O", Phys. Rev. C **59**, 1440–1448 (1999).

[90] R. J. Bartlett and M. Musiał, "Coupled-cluster theory in quantum chemistry", Rev. Mod. Phys. **79**, 291–352 (2007).

[91] D. J. Dean and M. Hjorth-Jensen, "Coupled-cluster approach to nuclear physics", Phys. Rev. C **69**, 054320 (2004).

[92] G. R. Jansen, M. Hjorth-Jensen, G. Hagen, and T. Papenbrock, "Toward open-shell nuclei with coupled-cluster theory", Phys. Rev. C **83**, 054306 (2011).

[93] G. D. Purvis and R. J. Bartlett, "A full coupled-cluster singles and doubles model: The inclusion of disconnected triples", J. Chem. Phys. **76**, 1910–1918 (1982).

[94] G. Hagen, T. Papenbrock, M. Hjorth-Jensen, and D. J. Dean, "Coupled-cluster computations of atomic nuclei", Rep. Prog. Phys. **77**, 096302 (2014).

[95] G. Hagen, T. Papenbrock, D. J. Dean, and M. Hjorth-Jensen, "Ab initio coupled-cluster approach to nuclear structure with modern nucleon-nucleon interactions", Phys. Rev. C **82**, 034330 (2010).

[96] G. Hagen, D. J. Dean, M. Hjorth-Jensen, T. Papenbrock, and A. Schwenk, "Benchmark calculations for H-3, He-4, O-16, and Ca-40 with ab initio coupled-cluster theory", Phys. Rev. C **76**, 044305 (2007).

[97] S. Binder, P. Piecuch, A. Calci, J. Langhammer, P. Navrátil, and R. Roth, "Extension of coupled-cluster theory with a noniterative treatment of connected triply excited clusters to three-body Hamiltonians", Phys. Rev. C **88**, 054319 (2013).

[98] S. Binder, J. Langhammer, A. Calci, P. Navrátil, and R. Roth, "Ab initio calculations of medium-mass nuclei with explicit chiral 3N interactions", Phys. Rev. C **87**, 021303 (2013).

[99] R. Roth, J. R. Gour, and P. Piecuch, "Ab initio coupled-cluster and configuration interaction calculations for O-16 using the V_{UCOM} interaction", Phys. Rev. C **79**, 054325 (2009).

[100] R. Roth, J. R. Gour, and P. Piecuch, "Center-of-mass problem in truncated configuration interaction and coupled-cluster calculations", Phys. Lett. B **679**, 334–339 (2009).

[101] S. Binder, J. Langhammer, A. Calci, and R. Roth, "Ab initio path to heavy nuclei", Phys. Lett. B **736**, 119–123 (2014).

[102] E. D. Jurgenson, P. Navrátil, and R. J. Furnstahl, "Evolution of Nuclear Many-Body Forces with the Similarity Renormalization Group", Phys. Rev. Lett. **103**, 082501 (2009).

[103] K. Tsukiyama, S. K. Bogner, and A. Schwenk, "In-Medium Similarity Renormalization Group For Nuclei", Phys. Rev. Lett. **106**, 222502 (2011).

[104] H. Hergert, S. K. Bogner, T. D. Morris, A. Schwenk, and K. Tsukiyama, "The In-Medium Similarity Renormalization Group: A novel ab initio method for nuclei", Phys. Rep. **621**, 165–222 (2016).

[105] H. Hergert, S. K. Bogner, S. Binder, A. Calci, J. Langhammer, R. Roth, and A. Schwenk, "In-medium similarity renormalization group with chiral two- plus three-nucleon interactions", Phys. Rev. C **87**, 034307 (2013).

[106] S. R. Stroberg, H. Hergert, J. D. Holt, S. K. Bogner, and A. Schwenk, "Ground and excited states of doubly open-shell nuclei from ab initio valence-space Hamiltonians", Phys. Rev. C **93**, 051301 (2016).

[107] K. Tsukiyama, S. K. Bogner, and A. Schwenk, "In-medium similarity renormalization group for open-shell nuclei", Phys. Rev. C **85**, 061304 (2012).

[108] H. Hergert, S. K. Bogner, T. D. Morris, S. Binder, A. Calci, J. Langhammer, and R. Roth, "Ab initio multireference in-medium similarity renormalization group calculations of even calcium and nickel isotopes", Phys. Rev. C **90**, 041302 (2014).

[109] E. Gebrerufael, K. Vobig, H. Hergert, and R. Roth, "Ab Initio Description of Open-Shell Nuclei: Merging No-Core Shell Model and In-Medium Similarity Renormalization Group", Phys. Rev. Lett. **118**, 152503 (2017).

[110] H. Hergert, "In-medium similarity renormalization group for closed and open-shell nuclei", Phys. Scr **92**, 023002 (2017).

[111] R. Stroberg, A. Calci, J. Holt, P. Navratil, S. Bogner, H. Hergert, R. Roth, and A. Schwenk, "Ab initio treatment of fully open-shell medium-mass nuclei with the IM-SRG", in APS Div. Nuc. Phys. (Sept. 2016).

[112] Z. M. Niu, Z. L. Zhu, Y. F. Niu, B. H. Sun, T. H. Heng, and J. Y. Guo, "Radial basis function approach in nuclear mass predictions", Phys. Rev. C **88**, 024325 (2013).

[113] C. F. V. Weizsäcker, "Zur Theorie der Kernmassen", Zeitschrift fur Physik **96**, 431–458 (1935).

[114] R. H. Stuewer, "Gamow, Alpha Decay, and the Liquid-Drop Model of the Nucleus", in George Gamow Symposium, Vol. 129, edited by E. Harper and D. Anderson, Astronomical Society of the Pacific Conference Series (1997).

[115] G. Gamow, "Mass Defect Curve and Nuclear Constitution", Proc. Royal Soc. A **126**, 632–644 (1930).

[116] N. Bohr and J. A. Wheeler, "The Mechanism of Nuclear Fission", Phys. Rev. **56**, 426–450 (1939).

[117] H. A. Bethe and R. F. Bacher, "Nuclear Physics A. Stationary States of Nuclei", Rev. Mod. Phys. **8**, 82–229 (1936).

[118] J. M. Pearson and S. Goriely, "Nuclear mass formulas for astrophysics", Nucl. Phys. A **777**, 623–644 (2006).

[119] D. Lunney, J. M. Pearson, and C. Thibault, "Recent trends in the determination of nuclear masses", Rev. Mod. Phys. **75**, 1021–1082 (2003).

[120] W. D. Myers and W. J. Swiatecki, "Nuclear masses and deformations", Nucl. Phys. A **81**, 1 (1966).

[121] S. Ludwig, H. von Groote, E. Hilf, A. G. W. Cameron, and J. Truran, "Droplet mass formula fit", Nucl. Phys. A **203**, 627–640 (1973).

[122] V. M. Strutinsky, ""Shells" in deformed nuclei", Nucl. Phys. A **122**, 1–33 (1968).

[123] M. Brack and P. Quentin, "Self-consistent average density matrices and the strutinsky energy theorem", Phys. Lett. B **56**, 421–423 (1975).

[124] G. G. Bunatian, V. M. Kolomietz, and V. M. Strutinsky, "A foundation to the shell correction method", Nucl. Phys. A **188**, 225–258 (1972).

[125] P. Möller, J. R. Nix, W. D. Myers, and W. J. Swiatecki, "Nuclear Ground-State Masses and Deformations", At. Data Nucl. Data Tables **59**, 185 (1995).

[126] P. Möller and J. R. Nix, "Atomic Masses and Nuclear Ground-State Deformations Calculated with a New Macroscopic-Microscopic Model", At. Data Nucl. Data Tables **26**, 165 (1981).

[127] J. Treiner and H. Krivine, "Semi-classical nuclear properties from effective interactions", Annals of Physics **170**, 406–453 (1986).

[128] J. Bardeen, L. N. Cooper, and J. R. Schrieffer, "Theory of Superconductivity", Phys. Rev. **108**, 1175–1204 (1957).

[129] P. Möller, W. D. Myers, H. Sagawa, and S. Yoshida, "New Finite-Range Droplet Mass Model and Equation-of-State Parameters", Phys. Rev. Lett. **108**, 052501 (2012).

[130] A. K. Dutta, J.-P. Arcoragi, J. M. Pearson, R. Behrman, and F. Tondeur, "Thomas-fermi approach to nuclear mass formula (I). Spherical nuclei", Nucl. Phys. A **458**, 77–94 (1986).

[131] N. Wang, M. Liu, and X. Wu, "Modification of nuclear mass formula by considering isospin effects", Phys. Rev. C **81**, 044322 (2010).

[132] H. J. Krappe and K. Pomorski, eds., *Theory of Nuclear Fission*, Lecture Notes in Physics, Springer (2012).

[133] S. Goriely, "Nuclear inputs for astrophysics applications", in AIP Conf. Series, Vol. 529 (July 2000).

[134] M. Liu, N. Wang, Y. Deng, and X. Wu, "Further improvements on a global nuclear mass model", Phys. Rev. C **84**, 014333 (2011).

[135] A. P. Zuker, "On the microscopic derivation of a mass formula", Nucl. Phys. A **576**, 65–108 (1994).

[136] J. Duflo and A. P. Zuker, "Microscopic mass formulas", Phys. Rev. C **52**, R23–R27 (1995).

[137] J. Mendoza-Temis, J. G. Hirsch, and A. P. Zuker, "The anatomy of the simplest Duflo-Zuker mass formula", Nucl. Phys. A **843**, 14–36 (2010).

[138] E. Caurier, G. Martínez-Pinedo, F. Nowacki, A. Poves, and A. P. Zuker, "The shell model as a unified view of nuclear structure", Rev. Mod. Phys. **77**, 427–488 (2005).

[139] M. Hjorth-Jensen, T. T. S. Kuo, and E. Osnes, "Realistic effective interactions for nuclear systems", Phys. Rep. **261**, 125–270 (1995).

[140] B. H. Wildenthal, "Empirical strengths of spin operators in nuclei", Prog. Part. Nucl. Phys. **11**, 5–51 (1984).

[141] B. A. Brown and W. A. Richter, "New "USD" Hamiltonians for the sd shell", Phys. Rev. C **74**, 034315 (2006).

[142] M. Honma, T. Otsuka, B. A. Brown, and T. Mizusaki, "New effective interaction for pf -shell nuclei and its implications for the stability of the $N = Z = 28$ closed core", Phys. Rev. C **69**, 034335 (2004).

[143] A. Poves, J. Sánchez-Solano, E. Caurier, and F. Nowacki, "Shell model study of the isobaric chains A=50, A=51 and A=52", Nucl. Phys. A **694**, 157–198 (2001).

[144] K. Langanke and G. Martínez-Pinedo, "Applications of the shell model in nuclear astrophysics", Nucl. Phys. A **704**, 154–164 (2002).

[145] K. Langanke and G. Martínez-Pinedo, "Shell model studies for nuclear astrophysics", in J. Phys. Conf. Series, Vol. 580 (Feb. 2015).

[146] M. Bender, P.-H. Heenen, and P.-G. Reinhard, "Self-consistent mean-field models for nuclear structure", Rev. Mod. Phys. **75**, 121–180 (2003).

[147] S. E. Koonin, D. J. Dean, and K. Langanke, "Results From Shell-Model Monte Carlo Studies", Annu. Rev. Nucl. Part. Sci. **47**, 463–504 (1997).

[148] S. E. Koonin, D. J. Dean, and K. Langanke, "Shell model Monte Carlo methods", Phys. Rep. **278**, 1–77 (1997).

[149] S. Goriely, N. Chamel, and J. M. Pearson, "Latest results of Skyrme-Hartree-Fock-Bogoliubov mass formulas", in J. Phys. Conf. Series (Jan. 2016).

[150] R. J. Furnstahl, "The UNEDF Project", Nuclear Physics News **21**, 18–24 (2011).

[151] M. Kortelainen, T. Lesinski, J. Moré, W. Nazarewicz, J. Sarich, N. Schunck, M. V. Stoitsov, and S. Wild, "Nuclear energy density optimization", Phys. Rev. C **82**, 024313 (2010).

[152] M. Kortelainen, J. McDonnell, W. Nazarewicz, P.-G. Reinhard, J. Sarich, N. Schunck, M. V. Stoitsov, and S. M. Wild, "Nuclear energy density optimization: Large deformations", Phys. Rev. C **85**, 024304 (2012).

[153] M. Kortelainen, J. McDonnell, W. Nazarewicz, E. Olsen, P.-G. Reinhard, J. Sarich, N. Schunck, S. M. Wild, D. Davesne, J. Erler, and A. Pastore, "Nuclear energy density optimization: Shell structure", Phys. Rev. C **89**, 054314 (2014).

[154] S. Goriely, S. Hilaire, M. Girod, and S. Péru, "First Gogny-Hartree-Fock-Bogoliubov Nuclear Mass Model", Phys. Rev. Lett. **102**, 242501 (2009).

[155] A. Bohr and B. Mottelson, *Nuclear Structure, Vol. I* (World Scientific, 1998).

[156] D. Davesne, P. Becker, A. Pastore, and J. Navarro, "Infinite matter properties and zero-range limit of non-relativistic finite-range interactions", Annals of Physics **375**, 288–312 (2016).

[157] T. Skyrme, "CVII. The nuclear surface", Phil. Mag. **1**, 1043–1054 (1956).

[158] J. Bell and T. Skyrme, "CVIII. The nuclear spin-orbit coupling", Phil. Mag. **1**, 1055–1068 (1956).

[159] T. Skyrme, "The effective nuclear potential", Nucl. Phys. **9**, 615–634 (1959).

[160] J. R. Stone and P.-G. Reinhard, "The Skyrme interaction in finite nuclei and nuclear matter", Prog. Part. Nucl. Phys. **58**, 587–657 (2007).

[161] W. Greiner, J. Maruhn, and D. Bromley, *Nuclear Models* (Springer, 1997).

[162] D. Vautherin and D. M. Brink, "Hartree-Fock calculations with Skyrme's interaction. 1. Spherical nuclei", Phys. Rev. **C5**, 626–647 (1972).

[163] H. S. Köhler, "Skyrme force and the mass formula", Nucl. Phys. A **258**, 301–316 (1976).

[164] H. Krivine, J. Treiner, and O. Bohigas, "Derivation of a fluid-dynamical lagrangian and electric giant resonances", Nucl. Phys. A **336**, 155–184 (1980).

[165] J. Erler, N. Birge, M. Kortelainen, W. Nazarewicz, E. Olsen, A. M. Perhac, and M. Stoitsov, "The limits of the nuclear landscape", Nature **486**, 509–512 (2012).

[166] E. Chabanat, P. Bonche, P. Haensel, J. Meyer, and R. Schaeffer, "A Skyrme parametrization from subnuclear to neutron star densities. Part II: Nuclei far from stabilities", Nucl. Phys. A **635**, 231–256 (1998).

[167] B. A. Brown and A. Schwenk, "Constraints on Skyrme equations of state from properties of doubly magic nuclei and ab initio calculations of low-density neutron matter", Phys. Rev. C **89**, 011307 (2014).

[168] J. Dobaczewski, H. Flocard, and J. Treiner, "Hartree-Fock-Bogolyubov description of nuclei near the neutron-drip line", Nucl. Phys. A **422**, 103–139 (1984).

[169] A. Bulgac and Y. Yu, "Renormalization of the Hartree-Fock-Bogoliubov Equations in the Case of a Zero Range Pairing Interaction", Phys. Rev. Lett. **88**, 042504 (2002).

[170] H. J. Mang, "The self-consistent single-particle model in nuclear physics", Phys. Rep. **18**, 325–368 (1975).

[171] M. Baldo, G. F. Burgio, H.-J. Schulze, and G. Taranto, "Nucleon effective masses within the Brueckner-Hartree-Fock theory: Impact on stellar neutrino emission", Phys. Rev. C **89**, 048801 (2014).

[172] K. Moghrabi, M. Grasso, G. Colò, and N. van Giai, "Beyond Mean-Field Theories with Zero-Range Effective Interactions: A Way to Handle the Ultraviolet Divergence", Phys. Rev. Lett. **105**, 262501 (2010).

[173] K. Moghrabi, M. Grasso, X. Roca-Maza, G. Colò, and N. Van Giai, "A beyond-mean-field example with zero-range effective interactions in infinite nuclear matter", in EPJ Web of Conf. Vol. 38 (Dec. 2012).

[174] K. Moghrabi and M. Grasso, "Dimensional regularization applied to nuclear matter with a zero-range interaction", Phys. Rev. C **86**, 044319 (2012).

[175] M. Grasso and M. Urban, "Hartree-Fock-Bogoliubov theory versus local-density approximation for superfluid trapped fermionic atoms", Phys. Rev. A **68**, 033610 (2003).

[176] B. G. Carlsson, J. Dobaczewski, and M. Kortelainen, "Local nuclear energy density functional at next-to-next-to-next-to-leading order", Phys. Rev. C **78**, 044326 (2008).

[177] N. Chamel and S. Goriely, "Spin and spin-isospin instabilities in asymmetric nuclear matter at zero and finite temperatures using Skyrme functionals", Phys. Rev. C **82**, 045804 (2010).

[178] X. Y. Xiong, J. C. Pei, and W. J. Chen, "Extension and parametrization of high-order density dependence in Skyrme forces", Phys. Rev. C **93**, 024311 (2016).

[179] J. Margueron, S. Goriely, M. Grasso, G. Colò, and H. Sagawa, "Extended Skyrme interaction. II: Ground state of nuclei and of nuclear matter", J. Phys. G **36**, 125103 (2009).

[180] D. Davesne, J. Navarro, P. Becker, R. Jodon, J. Meyer, and A. Pastore, "Extended Skyrme pseudopotential deduced from infinite nuclear matter properties", Phys. Rev. C **91**, 064303 (2015).

[181] D. Davesne, A. Pastore, and J. Navarro, "Skyrme effective pseudopotential up to the next-to-next-to-leading order", J. Phys. G **40**, 095104 (2013).

[182] D. Davesne, A. Pastore, and J. Navarro, "Extended Skyrme equation of state in asymmetric nuclear matter", A&A **585**, A83 (2016).

[183] Z. Zhang and L.-W. Chen, "Extended Skyrme interactions for nuclear matter, finite nuclei and neutron stars", Phys. Rev. **C94**, 064326 (2016).

[184] B. Behera, X. Viñas, M. Bhuyan, T. R. Routray, B. K. Sharma, and S. K. Patra, "Simple effective interaction: infinite nuclear matter and finite nuclei", J. Phys. G **40**, 095105 (2013).

[185] B. Behera, T. R. Routray, and R. K. Satpathy, "Momentum and density dependence of the mean field in nuclear matter", J. Phys. G **24**, 2073–2086 (1998).

[186] B. Behera, T. R. Routray, B. Sahoo, and R. K. Satpathy, "Momentum dependence of the mean field and equation of state of nuclear matter", Nucl. Phys. A **699**, 770–794 (2002).

[187] D. M. Brink and E. Boeker, "Effective interactions for Hartree-Fock calculations", Nucl. Phys. A **91**, 1–26 (1967).

[188] J. de Boer and H. J. Mang, eds., *D. GOGNY IN PROC. OF THE INT. CONF. ON NUCLEAR PHYSICS* (North-Holland, 1973).

[189] G. Ripka and M. Porneuf, eds., *D. GOGNY IN PROC. OF THE INT. CONF. ON NUCLEAR SELF-CONSISTENT FIELDS* (North-Holland, 1975).

[190] J. Dechargé and D. Gogny, "Hartree-Fock-Bogolyubov calculations with the D1 effective interaction on spherical nuclei", Phys. Rev. C **21**, 1568–1593 (1980).

[191] F. Chappert, M. Girod, and S. Hilaire, "Towards a new Gogny force parameterization: Impact of the neutron matter equation of state", Phys. Lett. B **668**, 420–424 (2008).

[192] D. Vretenar, A. V. Afanasjev, G. A. Lalazissis, and P. Ring, "Relativistic Hartree Bogoliubov theory: static and dynamic aspects of exotic nuclear structure", Phys. Rep. **409**, 101–259 (2005).

[193] J. F. Berger, M. Girod, and D. Gogny, "Time-dependent quantum collective dynamics applied to nuclear fission", Comp. Phys. Comm. **63**, 365–374 (1991).

[194] J. F. Berger, M. Girod, and D. Gogny, "Microscopic analysis of collective dynamics in low energy fission", Nucl. Phys. A **428**, 23–36 (1984).

[195] R. Sellahewa and A. Rios, "Isovector properties of the Gogny interaction", Phys. Rev. C **90**, 054327 (2014).

[196] Z. Fülöp, G. Gyürky, and E. Somorjai, *The 2nd International Conference on Nuclear Physics in Astrophysics* (SIF and Springer, 2007).

[197] S. Goriely, S. Hilaire, M. Girod, and S. Péru, "The Gogny-HFB nuclear-mass model", Eur. Phys. J. A **52**, 202 (2016).

[198] M. Farine, D. Von-Eiff, P. Schuck, J. F. Berger, J. Dechargé, and M. Girod, "Towards a new effective interaction of the Gogny type", J. Phys. G **25**, 863–866 (1999).

[199] J.-P. Delaroche, M. Girod, J. Libert, H. Goutte, S. Hilaire, S. Péru, N. Pillet, and G. F. Bertsch, "Structure of even-even nuclei using a mapped collective Hamiltonian and the D1S Gogny interaction", Phys. Rev. C **81**, 014303 (2010).

[200] J. Meng, *Relativistic Density Functional for Nuclear Structure* (World Scientific, 2016).

[201] C. J. Horowitz and B. D. Serot, "Self-consistent hartree description of finite nuclei in a relativistic quantum field theory", Nucl. Phys. A **368**, 503–528 (1981).

[202] R. Brockmann and R. Machleidt, "Relativistic nuclear structure. I. Nuclear matter", Phys. Rev. C **42**, 1965–1980 (1990).

[203] R. Brockmann and H. Toki, "Relativistic density-dependent Hartree approach for finite nuclei", Phys. Rev. Lett. **68**, 3408–3411 (1992).

[204] T.-S. Chen, H.-F. Lü, J. Meng, S.-Q. Zhang, and S.-G. Zhou, "Pseudospin Symmetry in Relativistic Framework with Harmonic Oscillator Potential and Woods-Saxon Potential", Chinese Physics Letters **20**, 358–361 (2003).

[205] H. Z. Liang, "Pseudospin symmetry in nuclear structure and its supersymmetric representation", Physica Scripta **91**, 083005 (2016).

[206] J. N. Ginocchio, "Pseudospin as a Relativistic Symmetry in Nuclei", in Computational and Group-Theoretical Methods in Nuclear Physics, edited by J. Escher, O. Castaños, J. G. Hirsch, S. Pittel, and G. Stoitcheva (Feb. 2004).

[207] H.-P. Duerr, "Relativistic Effects in Nuclear Forces", Phys. Rev. **103**, 469–480 (1956).

[208] J. D. Walecka, "A theory of highly condensed matter.", Annals of Physics **83**, 491–529 (1974).

[209] P. Ring, "Relativistic mean field theory in finite nuclei", Prog. Part. Nucl. Phys. **37**, 193–263 (1996).

[210] T. Nikšić, D. Vretenar, P. Finelli, and P. Ring, "Relativistic Hartree-Bogoliubov model with density-dependent meson-nucleon couplings", Phys. Rev. C **66**, 024306 (2002).

[211] W. H. Long, N. Van Giai, and J. Meng, "Relativistic Hartree-Fock theory. Part I: density-dependent effective Lagrangians", arXiv:nucl-th/0608009 (2006).

[212] J.-P. Ebran, E. Khan, D. Peña Arteaga, and D. Vretenar, "Relativistic Hartree-Fock-Bogoliubov model for deformed nuclei", Phys. Rev. C **83**, 064323 (2011).

[213] S. Typel and H. H. Wolter, "Relativistic mean field calculations with density-dependent meson-nucleon coupling", Nucl. Phys. A **656**, 331–364 (1999).

[214] J. Boguta and A. R. Bodmer, "Relativistic calculation of nuclear matter and the nuclear surface", Nucl. Phys. A **292**, 413–428 (1977).

[215] S. Gmuca, "Finite-nuclei calculations based on relativistic mean-field effective interactions", Nucl. Phys. A **547**, 447–458 (1992).

[216] Y. Sugahara and H. Toki, "Relativistic mean-field theory for unstable nuclei with non-linear σ and ω terms", Nucl. Phys. A **579**, 557–572 (1994).

[217] P.-G. Reinhard, "The nonlinearity of the scalar field in a relativistic mean-field theory of the nucleus", Zeitschrift fur Physik A **329**, 257–266 (1988).

[218] J. Blaizot and G. Ripka, *Quantum Theory of Finite Systems* (MIT Press, 1986).

[219] J. L. Egido, "State-of-the-art of beyond mean field theories with nuclear density functionals", Phys. Scr **91**, 073003 (2016).

[220] O. Haxel, J. H. Jensen, and H. E. Suess, "On the "Magic Numbers" in Nuclear Structure", Phys. Rev. **75**, 1766–1766 (1949).

[221] M. G. Mayer, "On Closed Shells in Nuclei. II", Phys. Rev. **75**, 1969–1970 (1949).

[222] J. K. MacDonald, "Successive Approximations by the Rayleigh-Ritz Variation Method", Phys. Rev. **43**, 830–833 (1933).

[223] N. N. Bogoliubov, "On a Variational Principle in the Many-Body Problem", Soviet Physics Doklady **3**, 292 (1958).

[224] R. Broglia and V. Zelevinsky, *Fifty Years of Nuclear BCS: Pairing in Finite Systems* (World Scientific, 2013).

[225] J. G. Valatin, "Generalized Hartree-Fock Method", Phys. Rev. **122**, 1012–1020 (1961).

[226] C. Bloch and A. Messiah, "The canonical form of an antisymmetric tensor and its application to the theory of superconductivity", Nucl. Phys. A **39**, 95–106 (1962).

[227] D. Thouless, *The Quantum Mechanics of Many-Body Systems* (Academic Press, 1972).

[228] N. Schunck and L. M. Robledo, "Microscopic theory of nuclear fission: a review", Rep. Prog. Phys. **79**, 116301 (2016).

[229] L. M. Robledo and G. F. Bertsch, "Application of the gradient method to Hartree-Fock-Bogoliubov theory", Phys. Rev. C **84**, 014312 (2011).

[230] D. J. Thouless, "Stability conditions and nuclear rotations in the Hartree-Fock theory", Nucl. Phys. A **21**, 225–232 (1960).

[231] J. Le Bloas, N. Pillet, M. Dupuis, J. M. Daugas, L. M. Robledo, C. Robin, and V. G. Zelevinsky, "First characterization of sd-shell nuclei with a multiconfiguration approach", Phys. Rev. C **89**, 011306 (2014).

[232] C. Robin, N. Pillet, D. Peña Arteaga, and J.-F. Berger, "Description of nuclear systems with a self-consistent configuration-mixing approach: Theory, algorithm, and application to the ^{12}C test nucleus", Phys. Rev. C **93**, 024302 (2016).

[233] D. J. Thouless, "Vibrational states of nuclei in the Random Phase Approximation", Nucl. Phys. A **22**, 78–95 (1961).

[234] S. Goriely, S. Hilaire, S. Péru, M. Martini, I. Deloncle, and F. Lechaftois, "Gogny-Hartree-Fock-Bogolyubov plus quasiparticle random-phase approximation predictions of the M 1 strength function and its impact on radiative neutron capture cross section", Phys. Rev. C **94**, 044306 (2016).

[235] K. Yoshida and N. van Giai, "Low-lying dipole resonance in neutron-rich Ne isotopes", Phys. Rev. C **78**, 014305 (2008).

[236] S. Péru and M. Martini, "Mean field based calculations with the Gogny force: Some theoretical tools to explore the nuclear structure", Eur. Phys. J. A **50**, 88 (2014).

[237] P.-G. Reinhard and K. Goeke, "The Generator Coordinate Method and quantised collective motion in nuclear systems", Rep. Prog. Phys. **50**, 1–64 (1987).

[238] J. J. Griffin and J. A. Wheeler, "Collective Motions in Nuclei by the Method of Generator Coordinates", Phys. Rev. **108**, 311–327 (1957).

[239] D. L. Hill and J. A. Wheeler, "Nuclear Constitution and the Interpretation of Fission Phenomena", Phys. Rev. **89**, 1102–1145 (1953).

[240] R. E. Peierls and J. Yoccoz, *The Collective Model of Nuclear Motion*, edited by R. H. Dalitz and R. Peierls (World Scientific, 1997).

[241] D. Varshalovich, A. Moskalev, and V. Khersonskii, *Quantum theory of angular momentum* (World Scientific, 1988).

[242] A. Messiah, *Quantum mechanics*, Quantum Mechanics v. 2 (North-Holland, 1981).

[243] J. O. Corbett, "A note on angular momentum projection operators", Nucl. Phys. A **169**, 426–428 (1971).

[244] M. Bender and P.-H. Heenen, "Configuration mixing of angular-momentum and particle-number projected triaxial Hartree-Fock-Bogoliubov states using the Skyrme energy density functional", Phys. Rev. C **78**, 024309 (2008).

[245] M. Bender, G. F. Bertsch, and P.-H. Heenen, "Global study of quadrupole correlation effects", Phys. Rev. C **73**, 034322 (2006).

[246] A. Valor, P.-H. Heenen, and P. Bonche, "Configuration mixing of mean-field wave functions projected on angular momentum and particle number", Nucl. Phys. A **671**, 145–164 (2000).

[247] A. Arzhanov, *Gogny-Hartree-Fock-Bogolyubov Nuclear Mass Models with Application to r-Process Stellar Nucleosynthesis*, KTH Royal Institute of Technology and Technische Universität Darmstadt (2013).

[248] A. Arzhanov, T. Rodriguez, and G. Martínez-Pinedo, "Large-scale Gogny-HFB calculation for r-process nucleosynthesis: towards a fully-converged microscopic mass table", in Nuclei in the Cosmos XIII (2014).

[249] A. Arzhanov, T. R. Rodríguez, and G. Martínez-Pinedo, "Systematic study of infrared energy corrections in truncated oscillator spaces with Gogny energy density functionals", Phys. Rev. C **94**, 054319 (2016).

[250] W. Ryssens, P.-H. Heenen, and M. Bender, "Numerical accuracy of mean-field calculations in coordinate space", Phys. Rev. C **92**, 064318 (2015).

[251] S. Hilaire and M. Girod, "Large-scale mean-field calculations from proton to neutron drip lines using the D1S Gogny force", Eur. Phys. J. A **33**, 237–241 (2007).

[252] R. J. Furnstahl, G. Hagen, and T. Papenbrock, "Corrections to nuclear energies and radii in finite oscillator spaces", Phys. Rev. C **86**, 031301 (2012).

[253] S. N. More, A. Ekström, R. J. Furnstahl, G. Hagen, and T. Papenbrock, "Universal properties of infrared oscillator basis extrapolations", Phys. Rev. C **87**, 044326 (2013).

[254] R. J. Furnstahl, S. N. More, and T. Papenbrock, "Systematic expansion for infrared oscillator basis extrapolations", Phys. Rev. C **89**, 044301 (2014).

[255] R. J. Furnstahl, G. Hagen, T. Papenbrock, and K. A. Wendt, "Infrared extrapolations for atomic nuclei", J. Phys. G **42**, 034032 (2015).

[256] M. V. Stoitsov, W. Nazarewicz, and S. Pittel, "New discrete basis for nuclear structure studies", Phys. Rev. C **58**, 2092–2098 (1998).

[257] M. Baldo, L. Robledo, P. Schuck, and X. Viñas, "Energy density functional on a microscopic basis", J. Phys. G **37**, 064015 (2010).

[258] AMEDEE database,
available online:
http://www-phynu.cea.fr/HFB-5DCH-table.htm
and as supplementary material in epaps repository:
http://link.aps.org/supplemental/10.1103/PhysRevC.81.014303.

[259] P. Maris, J. P. Vary, and A. M. Shirokov, "Ab initio no-core full configuration calculations of light nuclei", Phys. Rev. C **79**, 014308 (2009).

[260] C. Forssén, J. P. Vary, E. Caurier, and P. Navrátil, "Converging sequences in the ab initio no-core shell model", Phys. Rev. C **77**, 024301 (2008).

[261] S. K. Bogner, R. J. Furnstahl, P. Maris, R. J. Perry, A. Schwenk, and J. P. Vary, "Convergence in the no-core shell model with low-momentum two-nucleon interactions", Nucl. Phys. A **801**, 21–42 (2008).

[262] M. Lüscher, "Volume dependence of the energy spectrum in massive quantum field theories: I. Stable particle states", Commun. Math. Phys. **104**, 177–206 (1986).

[263] M. Lüscher, "Volume dependence of the energy spectrum in massive quantum field theories: II. Scattering states", Commun. Math. Phys. **105**, 153–188 (1986).

[264] E. D. Jurgenson, P. Maris, R. J. Furnstahl, P. Navrátil, W. E. Ormand, and J. P. Vary, "Structure of p-shell nuclei using three-nucleon interactions evolved with the similarity renormalization group", Phys. Rev. C **87**, 054312 (2013).

[265] V. Somà, C. Barbieri, and T. Duguet, "Ab initio Gorkov-Green's function calculations of open-shell nuclei", Phys. Rev. C **87**, 011303 (2013).

[266] D. Sääf and C. Forssén, "Microscopic description of translationally invariant core+N+N overlap functions", Phys. Rev. C **89**, 011303 (2014).

[267] S. A. Coon, M. I. Avetian, M. K. G. Kruse, U. van Kolck, P. Maris, and J. P. Vary, "Convergence properties of ab initio calculations of light nuclei in a harmonic oscillator basis", Phys. Rev. C **86**, 054002 (2012).

[268] A. Rios and R. Sellahewa, *The Gogny interaction in infinite matter: from nuclei to neutron stars*, First Gogny Conference, France (December 2015).

[269] P. O. Fröman, S. Yngve, and N. Fröman, "The energy levels and the corresponding normalized wave functions for a model of a compressed atom", J. Math. Phys. **28**, 1813–1826 (1987).

[270] T. R. Rodríguez, A. Arzhanov, and G. Martínez-Pinedo, "Toward global beyond-mean-field calculations of nuclear masses and low-energy spectra", Phys. Rev. C **91**, 044315 (2015).

[271] S. Goriely, M. Samyn, and J. M. Pearson, "Further explorations of Skyrme-Hartree-Fock-Bogoliubov mass formulas. VII. Simultaneous fits to masses and fission barriers", Phys. Rev. C **75**, 064312 (2007).

[272] K. Q. Lu, Z. X. Li, Z. P. Li, J. M. Yao, and J. Meng, "Global study of beyond-mean-field correlation energies in covariant energy density functional theory using a collective Hamiltonian method", Phys. Rev. C **91**, 027304 (2015).

[273] M. Bender, G. F. Bertsch, and P.-H. Heenen, "Collectivity-induced quenching of signatures for shell closures", Phys. Rev. C **78**, 054312 (2008).

[274] S. G. Rohoziński, "Gaussian overlap approximation for the quadrupole collective states", J. Phys. G **39**, 095104 (2012).

[275] B. Bally, B. Avez, M. Bender, and P.-H. Heenen, "Beyond Mean-Field Calculations for Odd-Mass Nuclei", Phys. Rev. Lett. **113**, 162501 (2014).

[276] M. Borrajo and J. L. Egido, "Ground-state properties of even and odd Magnesium isotopes in a symmetry-conserving approach", Phys. Lett. B **764**, 328–334 (2017).

[277] P. Möller, R. Bengtsson, B. G. Carlsson, P. Olivius, and T. Ichikawa, "Global Calculations of Ground-State Axial Shape Asymmetry of Nuclei", Phys. Rev. Lett. **97**, 162502 (2006).

[278] K. Hara, A. Hayashi, and P. Ring, "Exact angular momentum projection of cranked Hartree-Fock-Bogoliubov wave functions", Nucl. Phys. A **385**, 14–28 (1982).

[279] L. M. Robledo, "Ground state octupole correlation energy with effective forces", J. Phys. G **42**, 055109 (2015).

[280] B. Sabbey, M. Bender, G. F. Bertsch, and P.-H. Heenen, "Global study of the spectroscopic properties of the first 2^+ state in even-even nuclei", Phys. Rev. C **75**, 044305 (2007).

[281] L. M. Robledo, HFBAXIAL *code*, Universidad Autónoma de Madrid, 2002.

[282] M. Anguiano, J. L. Egido, and L. M. Robledo, "Particle number projection with effective forces", Nucl. Phys. A **696**, 467–493 (2001).

[283] T. R. Rodríguez and J. L. Egido, "New Beyond-Mean-Field Theories: Examination of the Potential Shell Closures at N=32 or 34", Phys. Rev. Lett. **99**, 062501 (2007).

[284] GSI Helmholtz Centre for Heavy Ion Research, `https://wiki.gsi.de/cgi-bin/view/Linux/GridEngine`.

[285] Goethe University Frankfurt, `http://csc.uni-frankfurt.de/index.php?id=51&L=0`.

[286] T. R. Rodríguez and J. L. Egido, "Triaxial angular momentum projection and configuration mixing calculations with the Gogny force", Phys. Rev. C **81**, 064323 (2010).

[287] S. Raman, C. W. Nestor, and P. Tikkanen, "Transition Probability from the Ground to the First-Excited 2^+ State of even-even Nuclides", At. Data Nucl. Data Tables **78**, 1–128 (2001).

[288] G. F. Bertsch, M. Girod, S. Hilaire, J.-P. Delaroche, H. Goutte, and S. Péru, "Systematics of the First 2^+ Excitation with the Gogny Interaction", Phys. Rev. Lett. **99**, 032502 (2007).

[289] M. Bender, P. Bonche, and P.-H. Heenen, "Shape coexistence in neutron-deficient Kr isotopes: Constraints on the single-particle spectrum of self-consistent mean-field models from collective excitations", Phys. Rev. C **74**, 024312 (2006).

[290] W. Heisenberg, "Über den Bau der Atomkerne. I", Zeitschrift fur Physik **77**, 1–11 (1932).

[291] W. Satuła, J. Dobaczewski, and W. Nazarewicz, "Odd-Even Staggering of Nuclear Masses: Pairing or Shape Effect?", Phys. Rev. Lett. **81**, 3599–3602 (1998).

[292] M. Bender, K. Rutz, P.-G. Reinhard, and J. A. Maruhn, "Pairing gaps from nuclear mean-field models", Eur. Phys. J. A **8**, 59–75 (2000).

[293] J. Dobaczewski, P. Magierski, W. Nazarewicz, W. Satuła, and Z. Szymański, "Odd-even staggering of binding energies as a consequence of pairing and mean-field effects", Phys. Rev. C **63**, 024308 (2001).

[294] T. Duguet, P. Bonche, P.-H. Heenen, and J. Meyer, "Pairing correlations. I. Description of odd nuclei in mean-field theories", Phys. Rev. C **65**, 014310 (2002).

[295] K. Langanke, G. Martínez-Pinedo, I. Petermann, and F. K. Thielemann, "Nuclear quests for supernova dynamics and nucleosynthesis", Prog. Part. Nucl. Phys. **66**, 319–328 (2011).

[296] K. Langanke and M. Wiescher, "Nuclear reactions and stellar processes", Rep. Prog. Phys. **64**, 1657–1701 (2001).

[297] Y. E. Penionzhkevich and S. M. Luk'yanov, "Nuclei near closed shells N = 20 and N = 28", Phys. Part. Nucl. **37**, 240–267 (2006).

[298] M. Bender, W. Nazarewicz, and P.-G. Reinhard, "Shell stabilization of super- and hyperheavy nuclei without magic gaps", Phys. Lett. B **515**, 42–48 (2001).

[299] P. Moller and J. R. Nix, "Stability of heavy and superheavy elements", J. Phys. G **20**, 1681–1747 (1994).

[300] Z. Ren, D.-H. Chen, F. Tai, H. Y. Zhang, and W. Q. Shen, "Ground state properties of odd-Z superheavy nuclei", Phys. Rev. C **67**, 064302 (2003).

[301] G. Martínez-Pinedo, D. Mocelj, N. T. Zinner, A. Kelić, K. Langanke, I. Panov, B. Pfeiffer, T. Rauscher, K.-H. Schmidt, and F.-K. Thielemann, "The role of fission in the r-process", Prog. Part. Nucl. Phys. **59**, 199–205 (2007).

[302] I. V. Panov, I. Y. Korneev, G. Martinez-Pinedo, and F.-K. Thielemann, "Influence of spontaneous fission rates on the yields of superheavy elements in the r-process", Astron. Lett. **39**, 150–160 (2013).

[303] G. A. Lalazissis, P. Ring, and D. Vretenar, eds., *Extended Density Functionals in Nuclear Structure Physics*, Lecture Notes in Physics (Springer, 2004).

[304] N. Schunck, J. Dobaczewski, J. McDonnell, J. Moré, W. Nazarewicz, J. Sarich, and M. V. Stoitsov, "One-quasiparticle states in the nuclear energy density functional theory", Phys. Rev. C **81**, 024316 (2010).

[305] A. V. Afanasjev, "Superheavy nuclei: a relativistic mean field outlook", Physica Scripta T **125**, 62–67 (2006).

[306] R. Balian, H. Flocard, and M. Vénéroni, "Variational extensions of BCS theory", Phys. Rep. **317**, 251–358 (1999).

[307] E. Baldini-Neto, B. V. Carlson, and D. Hirata, "Self-consistent Dirac quasiparticle blocking approximation applied to the α-decay scheme of the superheavy element $^{287}115$", J. Phys. G **32**, 655–666 (2006).

[308] G. F. Bertsch, C. A. Bertulani, W. Nazarewicz, N. Schunck, and M. V. Stoitsov, "Odd-even mass differences from self-consistent mean field theory", Phys. Rev. C **79**, 034306 (2009).

[309] S. Perez-Martin and L. M. Robledo, "Microscopic justification of the equal filling approximation", Phys. Rev. C **78**, 014304 (2008).

[310] L. M. Robledo, R. Bernard, and G. F. Bertsch, "Pairing gaps in the Hartree-Fock-Bogoliubov theory with the Gogny D1S interaction", Phys. Rev. C **86**, 064313 (2012).

[311] K. Rutz, M. Bender, P.-G. Reinhard, J. A. Maruhn, and W. Greiner, "Odd nuclei and single-particle spectra in the relativistic mean-field model", Nucl. Phys. A **634**, 67–88 (1998).

[312] K. Rutz, M. Bender, P.-G. Reinhard, and J. Maruhn, "Pairing gap and polarisation effects", Phys. Lett. B **468**, 1–6 (1999).

[313] A. V. Afanasjev and H. Abusara, "Time-odd mean fields in covariant density functional theory: Nonrotating systems", Phys. Rev. C **81**, 014309 (2010).

[314] M. Zalewski, J. Dobaczewski, W. Satuła, and T. R. Werner, "Spin-orbit and tensor mean-field effects on spin-orbit splitting including self-consistent core polarizations", Phys. Rev. C **77**, 024316 (2008).

[315] E. Perlińska, S. G. Rohoziński, J. Dobaczewski, and W. Nazarewicz, "Local density approximation for proton-neutron pairing correlations: Formalism", Phys. Rev. C **69**, 014316 (2004).

[316] U. Post, E. Wüst, and U. Mosel, "Time-odd terms in the nuclear hamiltonian at high angular momenta", Nucl. Phys. A **437**, 274–284 (1985).

[317] B.-Q. Chen, P.-H. Heenen, P. Bonche, M. S. Weiss, and H. Flocard, "Observation of identical bands in superdeformed nuclei with the cranked Hartree-Fock method", Phys. Rev. C **46**, R1582–R1586 (1992).

[318] J. Dobaczewski and J. Dudek, "Time-odd components in the mean field of rotating superdeformed nuclei", Phys. Rev. C **52**, 1827–1839 (1995).

[319] A. V. Afanasjev and P. Ring, "Time-odd mean fields in the rotating frame: Microscopic nature of nuclear magnetism", Phys. Rev. C **62**, 031302 (2000).

[320] K. J. Pototzky, J. Erler, P.-G. Reinhard, and V. O. Nesterenko, "Properties of odd nuclei and the impact of time-odd mean fields: A systematic Skyrme-Hartree-Fock analysis", Eur. Phys. J. A **46**, 299–313 (2010).

[321] A. Villafranca and J. L. Egido, "Self-consistent description of the excited superdeformed bands in ^{191}Hg", Phys. Lett. B **408**, 35–41 (1997).

[322] T. Duguet, P. Bonche, P.-H. Heenen, and J. Meyer, "Pairing correlations. II. Microscopic analysis of odd-even mass staggering in nuclei", Phys. Rev. C **65**, 014311 (2002).

[323] H. Schatz, A. Aprahamian, V. Barnard, L. Bildsten, A. Cumming, M. Ouellette, T. Rauscher, F.-K. Thielemann, and M. Wiescher, "End Point of the rp Process on Accreting Neutron Stars", Phys. Rev. Lett. **86**, 3471–3474 (2001).

[324] K.-L. Kratz, J.-P. Bitouzet, F.-K. Thielemann, P. Moeller, and B. Pfeiffer, "Isotopic r-process abundances and nuclear structure far from stability - Implications for the r-process mechanism", ApJ **403**, 216–238 (1993).

[325] B. Chen, J. Dobaczewski, K.-L. Kratz, K. Langanke, B. Pfeiffer, F.-K. Thielemann, and P. Vogel, "Influence of shell-quenching far from stability on the astrophysical r-process", Phys. Lett. B **355**, 37–44 (1995).

[326] B. Pfeiffer, K.-L. Kratz, and F.-K. Thielemann, "Analysis of the solar-system r-process abundance pattern with the new ETFSI-Q mass formula", Zeitschrift fur Physik A **357**, 235–238 (1997).

[327] L. M. Robledo and G. F. Bertsch, ATB *code*, Universidad Autónoma de Madrid, 2015.

[328] B. Banerjee, H. J. Mang, and P. Ring, "Variational calculation of energy spectra of rotational nuclei at high spins", Nucl. Phys. A **215**, 366–382 (1973).

[329] J. L. Egido and L. M. Robledo, "Microscopic study of the octupole degree of freedom in the radium and thorium isotopes with Gogny forces", Nucl. Phys. A **494**, 85–101 (1989).

[330] K. Nomura, R. Rodríguez-Guzmán, and L. M. Robledo, "Spectroscopy of quadrupole and octupole states in rare-earth nuclei from a Gogny force", Phys. Rev. C **92**, 014312 (2015).

[331] S. A. Changizi, C. Qi, and R. Wyss, "Empirical pairing gaps, shell effects, and di-neutron spatial correlation in neutron-rich nuclei", Nucl. Phys. A **940**, 210–226 (2015).

[332] D. Atanasov, P. Ascher, K. Blaum, R. B. Cakirli, T. E. Cocolios, S. George, S. Goriely, F. Herfurth, H.-T. Janka, O. Just, M. Kowalska, S. Kreim, D. Kisler, Y. A. Litvinov, D. Lunney, V. Manea, D. Neidherr, M. Rosenbusch, L. Schweikhard, A. Welker, F. Wienholtz, R. N. Wolf, and K. Zuber, "Precision Mass Measurements of $^{129-131}$Cd and Their Impact on Stellar Nucleosynthesis via the Rapid Neutron Capture Process", Phys. Rev. Lett. **115**, 232501 (2015).

[333] J. Hakala, J. Dobaczewski, D. Gorelov, T. Eronen, A. Jokinen, A. Kankainen, V. S. Kolhinen, M. Kortelainen, I. D. Moore, H. Penttilä, S. Rinta-Antila, J. Rissanen, A. Saastamoinen, V. Sonnenschein, and J. Äystö, "Precision Mass Measurements beyond ^{132}Sn: Anomalous Behavior of Odd-Even Staggering of Binding Energies", Phys. Rev. Lett. **109**, 032501 (2012).

[334] J. Dobaczewski, W. Nazarewicz, and M. V. Stoitsov, "Contact Pairing Interaction for the Hartree-Fock-Bogoliubov Calculations", in The Nuclear Many-Body Problem, edited by W. Nazarewicz and D. Vretenar (2002).

[335] Y. Yu and A. Bulgac, "Energy Density Functional Approach to Superfluid Nuclei", Phys. Rev. Lett. **90**, 222501 (2003).

[336] M. Anguiano, J. L. Egido, and L. M. Robledo, "Mean-field based approaches to pairing correlations in atomic nuclei", Phys. Lett. B **545**, 62–72 (2002).

[337] W.-C. Chen, J. Piekarewicz, and A. Volya, "Relativistic mean field plus exact pairing approach to open shell nuclei", Phys. Rev. C **89**, 014321 (2014).

[338] S. Hilaire, J.-F. Berger, M. Girod, W. Satuła, and P. Schuck, "Mass number dependence of nuclear pairing", Phys. Lett. B **531**, 61–66 (2002).

[339] W. A. Friedman and G. F. Bertsch, "Whence the odd-even staggering in nuclear binding?", Eur. Phys. J. A **41**, 109–113 (2009).

[340] M. Stoitsov, M. Kortelainen, S. K. Bogner, T. Duguet, R. J. Furnstahl, B. Gebremariam, and N. Schunck, "Microscopically based energy density functionals for nuclei using the density matrix expansion: Implementation and pre-optimization", Phys. Rev. C **82**, 054307 (2010).

[341] S. K. Bogner, R. J. Furnstahl, and L. Platter, "Density matrix expansion for low-momentum interactions", Eur. Phys. J. A **39**, 219–241 (2009).

[342] N. Schunck, J. D. McDonnell, D. Higdon, J. Sarich, and S. M. Wild, "Uncertainty quantification and propagation in nuclear density functional theory", Eur. Phys. J. A **51**, 169 (2015).

Acknowledgements

First of all, I would like to express my deepest appreciation to my supervisor Gabriel Martínez-Pinedo for giving me the opportunity to pursue my PhD studies in his group at TU Darmstadt and GSI. I am thankful for everything I have learned with his help: starting from his fascinating lectures on theoretical astrophysics back in 2010, continuing with my first self-contained scientific project during the GSI Summer School in 2011, and my subsequent master's project in his group at TUD in 2013, and then leading to my doctoral research with his continuous counsel and comprehensive support during all of its states. Without his careful guidance nothing of this would have been possible.

My sincere gratitude goes also to Tomás Rodríguez for sharing with me his vast expertise and knowledge in different subjects of nuclear physics, for his excitement in teaching, and his excellent mentoring that convincingly conveyed a spirit of adventure during all stages of my research.

I am also very thankful to Robert Roth for sharing his *ab initio* views on my *mean-field* topics of research, and giving me a lot of hints and elucidating advises during our numerous PhD committee meetings.

I would like to express my appreciation to Luis Robledo for spending (and self-consistently *blocking*) his time with me during our invaluable Skype discussions at the last stages of my PhD.

Many special thanks go to my current and former group members from the nuclear astrophysics group at TU Darmstadt and GSI for all those unforgettable years before and during my doctoral studies. Especially I would like to thank Andreas for always being supportive and ready to help in any difficulty, Heiko for sharing with me his passion for cycling and for his invaluable advises in every topic imaginable, Samuel for all our physical and non-physical discussions in the office and on our numerous trips together, André for being such a pleasant travel companion during not only my major PhD journey, but also during other minor ones as well.

I would like to thank my parents, Nataliya and Vasily, for always believing in me, for their continuous love and their support in my decisions. Without them none of my achievements would ever be possible.

Furthermore, I would like to thank my parents-in-law not only for their cheerful encouragements, but also for the delicious food aid from their side that kept me agile day by day.

Finally, a very special *thank you* is addressed to my wife, Yana, who showed an incredible amount of patience and not a whit less loving care during all this time starting from the first day of my PhD until this very last sentence.

Curriculum Vitae

Personal Data

Place and Date of Birth:	Moscow, Soviet Union, 30 March 1987
Residence:	Darmstadt, Germany
Citizenship:	Russian, Swedish
E-Mail:	*aarz@kth.se*

Education

2013 - 2017 PhD Candidate in Theoretical Nuclear Astrophysics
at **Technische Universität Darmstadt.**

2011 - 2013 Master of Science in Physics
at **Technische Universität Darmstadt.**

2010 - 2013 Master of Science in Engineering Physics
at **KTH Royal Institute of Technology.**

2006 - 2010 Bachelor of Science in Engineering Physics
at **KTH Royal Institute of Technology.**

2003 - 2006 Swedish academic certificate (Matriculation Standard)
at **Östra Real Gymnasium, Stockholm.**

1999 - 2004 Russian academic certificate (Matriculation Standard)
at **Secondary school at the Russian Embassy in Sweden, Stockholm.**

Erklärung zur Dissertation

Hiermit versichere ich, die vorliegende Dissertation ohne Hilfe Dritter nur mit den angegebenen Quellen und Hilfsmitteln angefertigt zu haben. Alle Stellen, die aus Quellen entnommen wurden, sind als solche kenntlich gemacht. Diese Arbeit hat in gleicher oder ähnlicher Form noch keiner Prüfungsbehörde vorgelegen. Eine Promotion wurde bisher noch nicht versucht.

Darmstadt, den 18. Juli 2017

_____

(Alexander Arzhanov)